



HAL
open science

Development of methods and electronic circuits for ultrasound imaging based on innovative probes

Paolo Mattesini

► **To cite this version:**

Paolo Mattesini. Development of methods and electronic circuits for ultrasound imaging based on innovative probes. Acoustics [physics.class-ph]. Université de Lyon; Università degli Studi di Firenze, 2020. English. NNT: 2020LYSE1036 . tel-03290929

HAL Id: tel-03290929

<https://theses.hal.science/tel-03290929>

Submitted on 19 Jul 2021

HAL is a multi-disciplinary open access archive for the deposit and dissemination of scientific research documents, whether they are published or not. The documents may come from teaching and research institutions in France or abroad, or from public or private research centers.

L'archive ouverte pluridisciplinaire **HAL**, est destinée au dépôt et à la diffusion de documents scientifiques de niveau recherche, publiés ou non, émanant des établissements d'enseignement et de recherche français ou étrangers, des laboratoires publics ou privés.



N°d'ordre NNT : 2020LYSE1036

THESE de DOCTORAT DE L'UNIVERSITE DE LYON

opérée au sein de

l'Université Claude Bernard Lyon 1

Ecole Doctorale MEGA (ED 162)

Mécanique, énergétique, génie civil, acoustique

Spécialité de doctorat : ACOUSTIQUE

Soutenue publiquement le 27/02/2020, par :

Paolo MATTESINI

LE DÉVELOPPEMENT DE MÉTHODES ET DE CIRCUITS ÉLECTRONIQUES D'IMAGERIE ULTRASONORE BASÉS SUR DES SONDES INNOVANTES

Devant le jury composé de :

CACHARD Christian	Professeur des Universités, Lyon 1	Examinateur
FORT Ada	Professoressa Associata, Siena	Examinatrice
LIEBGOTT Hervé	Professeur des Universités, Lyon 1	Co-directeur de thèse
MARQUE Catherine	Professeure des Universités, Compiègne	Examinatrice
RICCI Stefano	Professore Associato, Firenze	Examinateur
TORTOLI Piero	Professore Ordinario, Firenze	Directeur de thèse

Rapporteurs :

BALOCCO Simone	Associate Professor, University of Barcelona
MISCHI Massimo	Full Professor, Eindhoven University of Technology



UNIVERSITÀ
DEGLI STUDI
FIRENZE



UNIVERSITÉ
DE LYON

UNIVERSITÉ
FRANCO
ITALIENNE

UNIVERSITÀ
ITALO
FRANCESE

PHD IN

INFORMATION ENGINEERING

CYCLE XXXII

COORDINATOR PROF. SCHOEN FABIO

**DEVELOPMENT OF METHODS AND
ELECTRONIC CIRCUITS FOR
ULTRASOUND IMAGING BASED ON
INNOVATIVE PROBES**

Academic Discipline (SSD) ING-INF/01

Candidate

Dr. Mattesini Paolo

Supervisors

Prof. Tortoli Piero

Dr. Boni Enrico

Coordinator

Prof. Schoen Fabio

Prof. Liebgott Hervé

Prof. Basset Olivier

YEARS 2016/2019

Università degli Studi di Firenze, Dipartimento di Ingegneria dell'Informazione (DINFO).

Thesis submitted in partial fulfillment of the requirement for the degree of
Doctor of Philosophy in Information Engineering. Copyright © 2019 by
Paolo Mattesini

Abstract

Ultrasound (US) imaging systems, although intensively investigated by many research groups worldwide, have not achieved full maturity yet. US probes, in particular, have wide margins of improvement, not only in terms of materials and elements configuration but also of excitation modalities.

This PhD work has been committed to the development of electronic circuits and methods for US imaging based on innovative ultrasound probes.

First, I've developed the electronic circuits necessary to make an open ultrasound research system (ULA-OP 256) compatible with CMUT probes. CMUT technology is increasingly used because it offers wide band, high sensitivity and great flexibility in the design of elements geometry but, differently from the piezoelectric technology, needs high polarization and peak-to-peak voltages (hundreds of Volt). Since ULA-OP 256 was originally designed to work only with piezoelectric probes, I contributed to the development of circuits capable of adapting this open scanner to work also with CMUT array probes. Furthermore, within a collaboration with ST Microelectronics, I've developed an electronic board that allows to test a new 9-level power amplifier for the transmission of signals to both piezoelectric and CMUT probes.

The second part of my work has been dedicated to the investigation of possible use of "sparse" array probes for 3D high-frame rate and Doppler imaging. Sparse probes are 2D arrays in which a limited number of elements, comparable to the number of channels present in most US scanners, is distributed according to specific geometries, designed to optimize the transmit/receive acoustic beam. CMUT is the ideal technology for implementing sparse array probes, since it guarantees maximum flexibility in distributing the elements into arbitrary positions.

My work with sparse arrays has first included the investigation of possible limitations related to their use when they are committed to transmit Diverging Waves (DWs). These are unfocused waves that may notably increase the frame rate in volumetric (3D) imaging. In this activity, I've done simulations and experiments at CREATIS (Lyon) to

compare the achievable performance in terms of contrast and resolution when different DWs and sparse elements configurations are used.

Finally, a consistent part of my PhD has been focused on the evaluation of the use of sparse arrays in spectral Doppler applications. The intention of this study was to evaluate at which extent the sparsification of probe elements may affect the spectral Doppler performance. To achieve this goal, the use of a full-gridded 1024-element 2D array was compared with the use of a sparse arrays obtained by properly selecting 256 elements out of the same full array. The experiments were developed on both a rotating agar disc (where high SNR are achievable) and on a flow phantom (to test a more realistic condition) at CREATIS. The results of this work quantitatively confirm the suitability of sparse arrays for spectral Doppler velocity measurements, provided the poor signal-to-noise ratio due to the use of few active elements is properly compensated.

Sommario

I sistemi di imaging ad ultrasuoni (US), sebbene siano stati oggetto di intense indagini da parte di molti gruppi di ricerca in tutto il mondo, non hanno ancora raggiunto la piena maturità. Le sonde ad ultrasuoni, in particolare, hanno ampi margini di miglioramento, non solo in termini di materiali e configurazione degli elementi, ma anche di modalità di eccitazione.

Il mio lavoro di dottorato è stato impegnato nello sviluppo di circuiti elettronici e metodi per l'imaging ad ultrasuoni basati su sonde innovative.

In primo luogo, ho sviluppato i circuiti elettronici necessari per rendere compatibile un sistema di ricerca a ultrasuoni per scopi di ricerca (ULA-OP 256) con le sonde CMUT. La tecnologia CMUT è sempre più utilizzata perché offre ampia banda, elevata sensibilità e grande flessibilità nella progettazione della geometria degli elementi ma, a differenza della tecnologia piezoelettrica, necessita di alte tensioni di polarizzazione (dell'ordine delle centinaia di Volt). Poiché ULA-OP 256 è stato originariamente progettato per funzionare solo con sonde piezoelettriche, ho contribuito allo sviluppo di circuiti in grado di adattare questo scanner aperto per lavorare anche con sonde CMUT. Inoltre, in collaborazione con ST Microelectronics, ho sviluppato una scheda elettronica che permette di testare un nuovo amplificatore di potenza a nove livelli per la trasmissione di segnali sia alle sonde piezoelettriche che alle sonde CMUT.

La seconda parte del mio lavoro è stata dedicata allo studio del possibile utilizzo di sonde ad array "sparse" per ecografie 3D Doppler e ad alto frame rate. Le sonde sparse sono array 2D in cui un numero limitato di elementi, paragonabile al numero di canali presenti nella maggior parte degli scanner ad ultrasuoni, è distribuito secondo specifiche geometrie, progettate per ottimizzare il fascio acustico in trasmissione e ricezione. CMUT è la tecnologia ideale per l'implementazione di sonde sparse array, in quanto garantisce la massima flessibilità nella distribuzione degli elementi in posizioni arbitrarie.

Il mio lavoro con gli Sparse Array ha incluso prima di tutto lo studio di possibili limitazioni legate al loro utilizzo quando sono usati per

trasmettere onde divergenti (DWs). Si tratta di onde non focalizzate che permettono di aumentare notevolmente il frame rate nell'imaging volumetrico (3D). In questa attività, ho fatto simulazioni ed esperimenti nel laboratorio CREATIS (Lione) per confrontare le prestazioni ottenibili in termini di contrasto e risoluzione quando si utilizzano diverse configurazioni di DW e di elementi sparsi.

Infine, una parte consistente del mio dottorato di ricerca è stata focalizzata sulla valutazione dell'uso di array sparse in applicazioni Doppler spettrali. L'intenzione di questo studio era di valutare in che misura la dispersione degli elementi sulla superficie della sonda può influenzare le prestazioni del Doppler spettrale. Per raggiungere questo obiettivo, l'uso di un array 2D a 1024 elementi a griglia completa è stato confrontato con l'uso di array sparse ottenuti selezionando opportunamente 256 elementi sulla stessa matrice completa. Gli esperimenti sono stati sviluppati sia su un disco di agar rotante (dove sono raggiungibili alti SNR) che su un phantom di flusso (per testare una condizione più realistica) al CREATIS. I risultati di questo lavoro confermano quantitativamente l'idoneità degli array sparse per misure di velocità Doppler spettrali, a condizione che la perdita di rapporto segnale/rumore dovuto all'utilizzo di meno elementi attivi sia adeguatamente compensata.

Résumé

Les systèmes d'imagerie par ultrasons (US), bien étudiés par de nombreux groupes de recherche dans le monde entier, n'ont pas encore atteint leur pleine maturité. Les sondes US, en particulier, ont de larges marges d'amélioration, non seulement en termes de configuration des matériaux et des éléments, mais aussi en termes de modalités d'excitation.

Mon travail de doctorat a été consacré au développement de circuits électroniques et de méthodes pour l'imagerie US basés sur des sondes ultrasonores innovantes.

Tout d'abord, j'ai développé les circuits électroniques nécessaires pour rendre un échographe de recherche ouvert, le ULA-OP 256, compatible avec les sondes CMUT. La technologie CMUT est de plus en plus utilisée parce qu'elle permet l'utilisation d'une large bande de fréquences, une haute sensibilité et une grande flexibilité dans la géométrie des éléments. Néanmoins, contrairement à la technologie piézoélectrique, elle nécessite une polarisation et des tensions crête à crête élevées (centaines de Volt). L'échographe ULA-OP 256 ayant été conçu à l'origine pour fonctionner uniquement avec des sondes piézoélectriques, j'ai contribué au développement de circuits capables de fonctionner également avec des sondes en réseau CMUT. De plus, dans le cadre d'une collaboration avec ST Microelectronics, j'ai développé une carte électronique qui permet de tester un nouvel amplificateur de puissance à 9 niveaux pour la transmission de signaux aux sondes piézoélectriques et CMUT.

La deuxième partie de mon travail a été consacrée à l'étude de l'utilisation possible de sondes à réseaux clairsemés (dites *sparse* en anglais) pour l'imagerie 3D à haute cadence et l'imagerie Doppler. Les sondes clairsemées sont des matrices 2D dans lesquelles un nombre limité d'éléments, comparable au nombre de canaux présents dans la plupart des échographes, est distribué selon des géométries spécifiques, conçues pour optimiser le faisceau acoustique émis/reçu. CMUT est une technologie adaptée pour la mise en œuvre de sondes à réseaux clairsemés, car elle garantit une flexibilité maximale dans la distribution des éléments dans des positions arbitraires.

Mon travail avec les réseaux clairsemés a d'abord inclus l'étude de leurs limitations lorsqu'ils sont destinés à transmettre des ondes divergentes. Il s'agit d'ondes non focalisées qui peuvent augmenter considérablement la fréquence d'images en imagerie 3D. Ainsi, j'ai fait des simulations et des expériences au laboratoire CREATIS (Lyon) pour comparer les performances en termes de contraste et de résolution lorsque différentes configurations d'onde divergentes et de réseaux clairsemés sont utilisés.

Enfin, une partie conséquente de mon travail a été consacrée à l'évaluation de l'utilisation de réseaux clairsemés dans les applications de Doppler spectral. L'objectif de cette étude était d'évaluer dans quelle mesure la particulière distribution des éléments de la sonde peut affecter la performance du Doppler spectral. Pour atteindre cet objectif, j'ai comparé l'utilisation d'un réseau 2D de 1024 éléments d'une grille complète avec l'utilisation de réseaux clairsemés obtenus en sélectionnant 256 éléments de façon optimale. Les expériences ont été développées à la fois sur un disque de gélatine rotation (où un rapport signal à bruit élevé est réalisable) et sur un fantôme d'écoulement (pour tester une condition plus réaliste) à CREATIS. Les résultats de ces travaux confirment quantitativement l'adéquation des réseaux clairsemés aux mesures de vitesse de Doppler spectral, à condition que le faible rapport signal à bruit dû à l'utilisation de peu d'éléments actifs soit correctement compensé.

October 2019

Acknowledgments

I would like to sincerely thank my supervisors.

Prof. Piero Tortoli for his invaluable help and support starting from the master's degree thesis and especially during the PhD. He always pushed me and encouraged me to do my best even in the hard moments that happen during the research work: it is fundamental to always have a constant positive support to overcome the difficulties and do not lose the positivity.

Dr. Enrico Boni for his precious support during all my PhD activities: when you need a critical and competent point of view, you just have to ask him, and he will resolve your problems before that you realize of having problems.

Prof. Olivier Basset for welcoming me in the beautiful city of Lyon and for always supporting and instilled in me his typical calm needed to face all the challenges of a PhD journey.

Prof. Hervé Liebgott for very kindly hosting me in Lyon, for his incredible friendly attitude that have always warmed my heart (I will never forget our first “meeting”) and provided me everything that I needed to face my challenges, about research work but not only.

Special thanks are also due to Dr. Alessandro Ramalli (despite his favorite football team) for saving me every time that I was in trouble with MATLAB and always pushing me to give everything, especially when I was afraid that I was not good enough to complete a task. I hope that I will return you the favor in the tough challenges you are going to face.

In the end I want to thank all the people forming the two laboratories that I have attended:

MSDLab in Florence for being my second home and offering me a positive special environment where grow as researcher and, especially, as person. I found here friends before than colleagues: I would have never got through this experience without your help and laughs.

CREATIS in Lyon for hosted me as part of them and without mocking me (or at least, not too much) to be an Italian in France. I found very special people there and I have spent unforgettable moments with them: merci beaucoup pour tous mes amis!

Last, but not least I want to thank my family and my beloved ones for always believing in me and supporting me during these years: all the efforts finally turned me in to a Doctor, but maybe did not get me more serious.

“It is impossible to live without failing at something, unless you live so cautiously that you might as well not have lived at all - in which case, you fail by default.”

J.K. Rowling

Contents

Contents	3
Chapter 1. Introduction	7
1.1. Objective	8
1.2. Contributions	10
Chapter 2. Ultrasound Basics	12
2.1. Ultrasound waves	13
2.1.1. Ultrasound propagation	14
2.1.2. Pulsed Wave Systems	17
2.2. Ultrasound Imaging	19
2.3. ULA-OP 256 system	26
2.4. Verasonics Vantage 256 TM	31
Chapter 3. Hardware Development for CMUT probes	34
3.1. Contributions on Hardware Development for CMUT probes	35
3.2. Introduction to CMUT probes	35
3.2.1. Ultrasonic transducers	35
3.2.2. Capacitive acoustic transducers	37
3.2.3. CMUT technology	40
3.3. Hardware development to interface ULA-OP 256 with CMUT probes	41
3.3.2. Electronic board development for 256 elements linear CMUT probe	43
3.3.3. Acquisitions with linear CMUT probe with 256 elements	43
3.4. Realization of electronic board for testing a new 9-level ST Microelectronics pulser	45
Chapter 4. 3-D Imaging with Diverging Waves	57
4.1. Contributions on 3-D Imaging with DW	58
4.2. Plane and Diverging wave theory	58

4.3.	<i>Sparse arrays usage motivations</i>	61
4.4.	<i>3-D Diverging Waves using 2-D sparse arrays feasibility</i>	61
4.4.1.	<i>Experimental setup</i>	62
4.4.2.	<i>Acquisition sequence and phantom evaluation criteria</i>	64
4.4.3.	<i>Results</i>	67
4.5.	<i>Optimal virtual source distribution in 3-D Diverging Waves imaging</i>	68
4.5.1.	<i>Array configuration and transmission strategy</i>	69
4.5.2.	<i>Results</i>	70
Chapter 5. Spectral Doppler with 2-D sparse arrays		74
5.1.	<i>Contributions on Spectral Doppler with sparse arrays</i>	75
5.2.	<i>Doppler Ultrasound principles</i>	75
5.2.1.	<i>Continuous Wave Doppler Systems</i>	76
5.2.2.	<i>Pulsed Wave Doppler Systems</i>	78
5.2.3.	<i>Single- and Multi-Gate PW Doppler</i>	80
5.3.	<i>Doppler spectrum width</i>	81
5.3.1.	<i>Velocity, transit time and geometrical spectral broadening</i>	81
5.4.	<i>Preliminary Spectral Doppler measurements with 2-D sparse arrays</i>	84
5.4.1.	<i>System and arrays used</i>	85
5.4.2.	<i>Results</i>	88
5.5.	<i>Spectral Doppler simulations and measurements with 2-D sparse arrays on a flow phantom</i>	90
5.5.1.	<i>2-D array probe, simulations, experiments setup and processing</i>	90
5.5.2.	<i>Results</i>	96
5.5.3.	<i>Discussion</i>	100
Chapter 6. Conclusions		107
6.1.	<i>Summary of Contributions</i>	108
6.2.	<i>Direction of Future Works</i>	108

Chapter 1. Introduction

1.1. Objective

Ultrasound (US) imaging is broadly used both in biomedical and industrial applications, given its non-invasive, non-destructive and non-ionizing features. In recent years, many studies on new probe materials and geometries have contributed to improve the performance of 1-D and 2-D arrays. For instance, the CMUT technology permits to exploit the modern electronic micromachined techniques to realize ultrasound transducers but requires additional electronics to be introduced in US scanners. In this regard, part of my PhD activity was dedicated to the development of the electronic circuits necessary to make such type of probes compatible with the open US scanner ULA-OP 256 recently realized by the University of Florence for research purposes. The imaging results obtained with a 256-element linear array probe confirm the excellent resolution and contrast-to-noise ratio achievable with CMUT technology. The new circuits will also soon permit the test of a novel 2-D CMUT probe recently developed in collaboration with the University of Roma Tre.

2-D array probes, which can make finally feasible three-dimensional (3-D) US investigation in real-time, have gained special attention by the ultrasound research community in the last few years. Such probes could, in principle, extend Doppler analysis, until now restricted to a planar region, to any desired point inside a volume. This would be particularly useful, e.g. in carotid artery investigation, to correctly reconstruct 3-D morphology of plaques that are not perfectly described by means of standard B-Mode (planar) imaging.

2-D array probes are typically formed by many elements (usually up to thousands) organized in regular grids. In high end US machines these probes are usually controlled by expensive specific integrated circuits (ASICs). Possible methods to reduce the number of elements to be simultaneously controlled in 2-D probes include row-column addressing and sparse array probes. The latter ones are particularly attractive in terms of costs and flexibility, because characterized by a limited number of elements that can be individually controlled by a scanner. Such elements are distributed on the probe surface following specific geometries designed to enhance the corresponding acoustic beam both in transmission (TX) and in reception (RX).

A consistent part of this PhD work was dedicated to the investigation of possible limitations in the use of sparse array probes for imaging and

Doppler purposes. In the former cases, a sparse probe was used to reconstruct 2-D images from a volumetric region when diverging waves were transmitted. Spectral Doppler analysis with 256-element sparse array probes was also, for the first time, experimentally tested and compared with the results provided by a full, 1024-element, 2-D array.

The manuscript is organized as follows:

- Chapter 2: The basic concepts of ultrasonic wave propagation, the characteristic parameters of propagation media and the effects they produce are concisely illustrated. Fundamentals on ultrasound scanners and signal elaboration are summed up.

- Chapter 3: A brief introduction on ultrasound (piezo and CMUT) probes principles is reported. The electronic hardware developed to connect the ultrasound ULA-OP 256 scanner to new CMUT probes is described and preliminary experimental results are presented.

- Chapter 4: A short description about high-frame rate imaging techniques (Plane Waves and Diverging Waves) is presented. The description of 3-D imaging acquisitions using Diverging Waves and the obtained results are detailed.

- Chapter 5: The Doppler principles in ultrasound imaging are introduced. The comparison between the spectral Doppler performance of full-gridded and sparse 2-D arrays is analyzed through extensive simulations and experiments.

- Chapter 6: Conclusions and future works.

1.2. Contributions

Conference Proceedings

- E. Roux, F. Varray, L. Petrusca, **P. Mattesini**, C. Cachard, P. Tortoli, H. Liebgott, “3D Diverging Waves With 2D Sparse Arrays: A Feasibility Study”. IEEE International Ultrasonics Symposium 2017, Washington D.C., USA.
- **P. Mattesini**, A. Ramalli, E. Roux, L. Petrusca, H. Liebgott, O. Basset, P. Tortoli, “Spectral Doppler Measurements with 2-D Sparse Arrays”. IEEE International Ultrasonics Symposium 2018, Kobe, Japan.
- **P. Mattesini**, E. Roux, E. Badescu, L. Petrusca, O. Basset, P. Tortoli, H. Liebgott, “Optimal virtual sources distribution in 3-D Diverging Wave Ultrasound Imaging: an experimental study”. IEEE International Ultrasonics Symposium 2018, Kobe, Japan.
- A.S. Savoia, B. Mauti, L. Fanni, G. Caliano, E. Boni, **P. Mattesini**, M. Scaringella, P. Tortoli, “A 120+ 120- Element Crisscross CMUT Probe's with Real-Time Switchable Electronic and Fresnel Focusing Capabilities”. IEEE International Ultrasonics Symposium 2018, Kobe, Japan.
- **P. Mattesini**, A. Ramalli, G. Goti, L. Petrusca, O. Basset, P. Tortoli, H. Liebgott, “Spectral Doppler analysis with sparse and full 2-D arrays”. IEEE International Ultrasonics Symposium 2019, Glasgow, United Kingdom.

Journal paper

- **P. Mattesini**, A. Ramalli, L. Petrusca, O. Basset, H. Liebgott, P. Tortoli, “Spectral Doppler Measurements with 2-D Sparse Arrays”. IEEE Transactions on Ultrasonics, Ferroelectrics, and Frequency Control, 2019.

Chapter 2. Ultrasound Basics

In this chapter are briefly described the main principles of the Ultrasound Waves and of the Ultrasound Systems. The first part of the chapter introduces the physics of the Ultrasound, the second part deals with the generic model of Ultrasound systems, the third part describes more in details the Ultrasound Systems used during my PhD work: ULA-OP 256 and Verasonics Vantage 256.

2.1. Ultrasound waves

The physical phenomenon of sound can be described as a pressure wave that, starting from a vibrating body (source), propagates in a medium disturbing the particles that compose it. Perturbation consists in the displacement of the particles from the equilibrium position in space, transmitting this displacement to the adjacent particles. The direction of displacement (compression and rarefaction of the particles) is parallel to the direction of propagation of the wave. Ultrasounds are characterized by sound waves with a frequency of oscillation higher than those audible by the human ear, generally referred to as ultrasound for frequencies higher than 20 kHz.

The nature of this phenomenon can be explained mathematically by the theory of waves. The analytical expression of the acoustic wave is a solution to the equation:

$$\frac{d^2T}{dz^2} = \frac{\rho}{\beta} * \frac{d^2T}{dt^2} \quad (2.1)$$

where T [N/m^2] represents stress, ρ [kg/m^3] is the density of the medium in which the waves propagate and β [$\text{kg} / (\text{m s}^2)$] is the elastic constant of the medium. The generic solution of the equation is:

$$T(z, t) = T_0 * e^{j(2\pi ft \pm kz)} \quad (2.2)$$

$$k = \frac{\omega}{c} \quad (2.3)$$

This equation represents a flat wave propagating in the z direction, where f [Hz] is the frequency of stress oscillation, k [$1/\text{m}$] is the mean modulus of elasticity of the medium and T_0 the maximum value of pressure (modulus). The ultrasonic wave is also characterized by a wavelength λ which represents the distance between two points of the wave with the same amplitude value:

$$\lambda = \frac{c}{f} \quad (2.4)$$

where c [m/s] represents the speed of propagation of the wave in the medium.

The speed at which ultrasound propagate is directly linked to the density of the material they pass through, to its chemical-physical nature (for example, its state of aggregation and the type of bond between the atoms that compose it).

The propagation of ultrasonic waves is based on the oscillation of the particles of the medium and the transmission of this mechanical energy to the adjacent ones. It is easy to understand that several particles more in contact allows a higher speed of transmission of the oscillation. Another important parameter for estimating the speed of the wave is the elastic constant of the medium that describes the inertia of the material, or the speed of response to sound stress by the particles of the medium. The speed is therefore:

$$c^2 = \frac{\beta}{\rho} \quad (2.5)$$

2.1.1. Ultrasound propagation

In general, there are four different ways of propagating ultrasonic waves in a medium: through longitudinal, shear, superficial and Lamb waves. Instead in fluids without a crystalline lattice, it occurs only

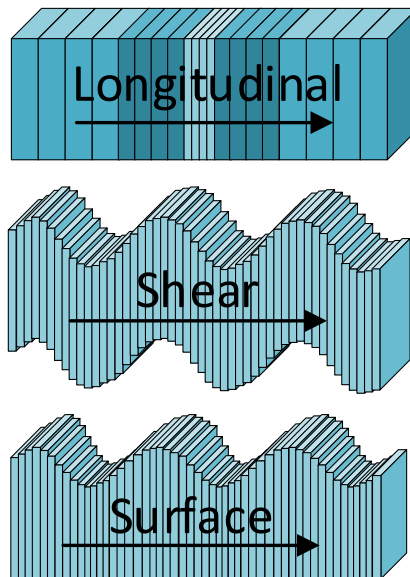


Fig. 2-1. Propagations modes of US waves.

through longitudinal waves: these are characterized of alternate phases of compression and expansion of the particles in the medium. The particles displacement occurs in the same direction as the propagation of the ultrasonic wave.

The shear waves are characterized by a displacement of the particles perpendicular to the direction of propagation of the ultrasonic beam, while the surface waves, have the characteristic of propagating in the surface layer of solids, following the profile of the medium, with a direction of vibration of the molecules perpendicular to the surface of the solid.

The three propagation modes are displayed in Fig. 2-1.

In thin materials, Lamb waves can be generated, which affect the entire cross-section of the solid and can vibrate symmetrically or asymmetrically.

An important parameter for understanding the propagation of sound waves is the acoustic impedance Z of the medium, which is defined as:

$$Z = \rho * c \quad (2.6)$$

The impedance Z [1 Rayl equals 1 kg / (m² s)] is a complex quantity that, in the case of plane waves or in the case of spherical propagation with a very distant source, assumes real values. The constant value of this quantity guarantees a constant velocity propagation in the medium and above all a continuous propagation in the same direction. When there are impedance discontinuities, special phenomena occur depending on the size of the discontinuity.

When the ultrasonic beam encounters a separation surface between two materials with different acoustic impedances, the phenomenon of reflection occurs: a part of the beam is transmitted from the first to the second medium, while a part is reflected at the interface. R is the coefficient of reflection given by the following relation:

$$R = \left(\frac{Z_2 - Z_1}{Z_1 + Z_2} \right)^2 \quad (2.7)$$

Where Z_1 and Z_2 are the acoustic impedances of medium 1 and 2 respectively.

T is the transmission coefficient given by the following formula:

$$T = \left(\frac{4 * Z_1 * Z_2}{(Z_1 + Z_2)^2} \right) \quad (2.8)$$

In the case where an ultrasonic beam affects a separation surface between two media at an angle other than zero, the beam penetrating into the second medium is partially refracted, as shown in Fig. 2-2.

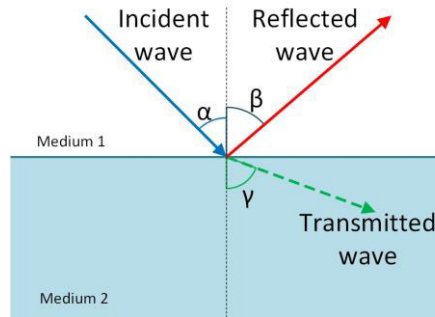


Fig. 2-2. US waves reflection and transmission scheme.

Snell's law, reported below, allows to determine the direction of the beam in the second medium.

$$\frac{\sin(\alpha)}{c_1} = \frac{\sin(\gamma)}{c_2} \quad (2.9)$$

Where α is the incidence angle, γ is the transmission angle, c_1 is the propagation speed of the wave in the medium 1 and c_2 is the propagation speed in the medium 2.

When an ultrasonic wave passes through a medium, it suffers an attenuation due to the heterogeneity of the material. This attenuation can be traced back to the phenomenon of absorption and diffusion. In general, absorption is due to the attenuation of the molecular movement and its subsequent transformation into heat. Diffusion is linked to the heterogeneity of the material and acts by dispersing the beam in several directions, generating an attenuation along the direction of propagation.

Attenuation A_{dB} is given by:

$$A_{dB} = 20 \log_{10} \left(\frac{I_1}{I_2} \right) \quad (2.10)$$

Where I_1 and I_2 are the beam intensities before and after being attenuated.

2.1.2. Pulsed Wave Systems

Pulsed wave (PW) sensors use a single transducer to transmit and receive the ultrasonic wave. It periodically sends short duration pulses with Pulse Repetition Frequency (PRF) called burst, each of which is composed of a fixed number of sinusoid cycles. In the interval between two consecutive bursts, the sensor listens to the echo. The signal reflected from a depth d reaches the receiver after an interval of time Δt from the transmission of the burst, this interval can be determined by the following relationship:

$$\Delta t = \frac{2d}{c} \quad (2.11)$$

Depending to the number of listening windows (gate) between two successive bursts, pulsed wave systems can differ in:

- *Single gate*: they can isolate the echo signal coming from only one depth.
- *Multi gate*: they allow signals from different depths to be discriminated against at the same time.

The range of depths that can be investigated by a PW system, depends on the duration D of the burst and its PRF. In fact, in order to avoid an overlap between the transmitted wave and the received one, it is necessary that the system, after the transmission, puts itself in listening mode. Therefore, echoes coming from distances less than d_{\min} cannot be acquired:

$$d_{\min} = c \cdot D \quad (2.12)$$

Similarly, it will not be possible to receive an echo that takes longer to return to the transducer than the one provided by the listening window between two consecutive bursts ($1 / PRF$) and therefore it will not be possible to investigate depths that are further than d_{max} from the transducer:

$$d_{max} = \frac{c}{2 \cdot PRF} \quad (2.13)$$

The single gate systems shown in the Fig. 2-3, can process the echo received from a single sample volume, placed at variable depths.

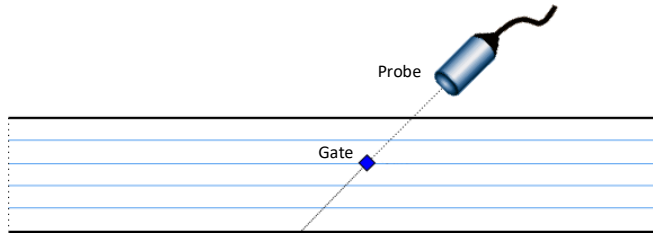


Fig. 2-3. Single gate US system.

During the listening window, the radio frequency signal that is received is not suitable for processing because it is very weak ($<10 \mu V$), so it is amplified by a low noise device.

It is then demodulated, extracting the component in phase and in quadrature, to distinguish the targets approaching and moving away. Then a low-pass filtering stage is used to eliminate high-frequency disturbances and finally a high-pass filtering stage to eliminate low-frequency contributions due to stationary or slowly fluctuating targets.

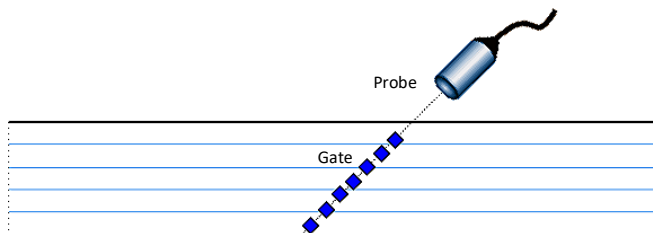


Fig. 2-4. Multi-gate US system.

Multi-gate systems, in Fig. 2-4, move the echo gating operation to the digital processing phase downstream of the Analog to Digital (A/D) converter (Fig. 2-5), whose sampling frequency will depend on the PRF, the number of gates and their size.

This allows to have information about targets at greater depths and thus reconstruct their motion in more detail than single gate systems.

In fact, by processing this data through an FFT (Fast-Fourier-Transform), it is possible to obtain spectral profiles that, suitably averaged, allow to trace a velocity profile of the fluid.

2.2. Ultrasound Imaging

The ultrasound imaging systems referred to in this thesis are biomedical systems (Fig. 2-6), i.e. they have the aim of studying the human body to detect and diagnose various pathologies. For example, ultrasound scanners that use ultrasound to observe entire organs or to perform targeted tests on sections of arteries or muscles.

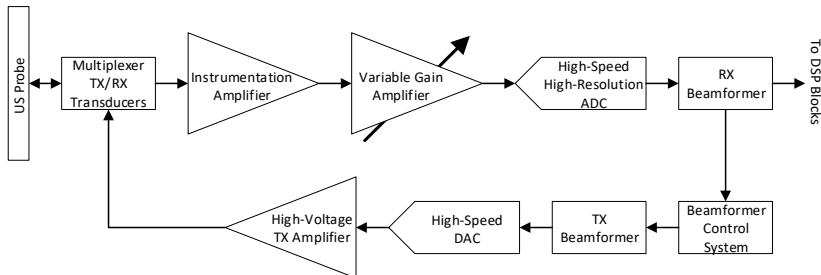


Fig. 2-5. US data elaboration chain.

In order to understand the applications of these systems, it is necessary to study their overall functioning, and which are the main blocks that make them up.

Regardless of the specific applications for which they are used, the type of signals generated or processed, the operation of these systems is quite general. Normally a programmable device such as FPGA (Field Programmable Gate Array) is responsible for the generation of electrical signals, which are then amplified and transmitted to the probe that transforms them into ultrasonic waves that will propagate in the medium to be investigated.



Fig. 2-6. MyLab™Six CrystaLine Esaote US system.

When these affect a target, i.e. a body with a different acoustic impedance, we observe the manifestation of ultrasonic reflection. The reflected wave, called echo, travels towards the probe that converts it into electrical signals that can be processed through DSP (Digital Signal Processor). Specifically, by observing the amplitude, frequency and delay between the echoes received and the signals transmitted, it is possible to obtain information on the position, movement and physical parameters (material, geometry, etc., ...) that characterize the target.

The information resulting from the analysis of multiple echoes and/or transmissions can therefore be used to investigate areas or volumes of interest and show the data on a display.

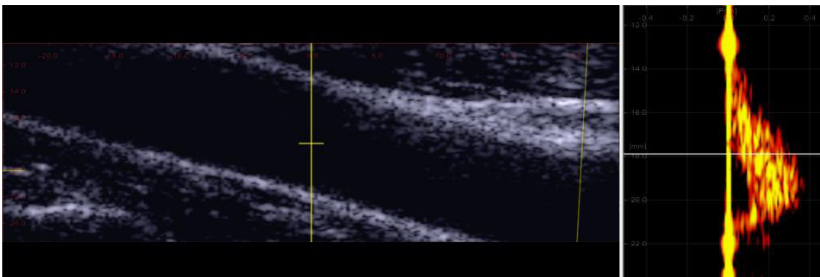


Fig. 2-7. B-mode image of a carotid artery (left) and the associate blood flow profile (right).

Fig. 2-7 shows an example image, obtained with an ultrasound system, of a B-mode image of the carotid artery (left) and the profile of the speed (right) of the blood flow in the same carotid artery, obtained through the phase shift between the impulse sent and the subsequent echoes received.

An ultrasound system is usually composed of the blocks shown in Fig. 2-8: the first element is the probe, which is connected by a set of cables to the electronic apparatus for transmission and reception.

The cable is a critical element because it is made up of several wires equal to the number of transducers present in the probe, inserted inside a plastic sheath that protects them from mechanical stress and, often, also covered by a metallic layer that prevents electromagnetic disturbances. If the number of elements is very high, the cable has a significant thickness that leads to a loss of flexibility and therefore greater difficulty in usage. This aspect limits the number of probe elements, however, by reducing the thickness of the individual wires connecting the transducers, linear probes with 192 elements or matrix probes with 256 elements are commonly used.

The interface between the transducers and the electronics is formed by a multiplexer that connects the transmission and reception channels to one or more elements of the probe. The reason for its presence is that the number of transducers is usually higher than the number of signal generation and processing channels and the choice of probe elements used determines the spatial characteristics of the beam focusing.

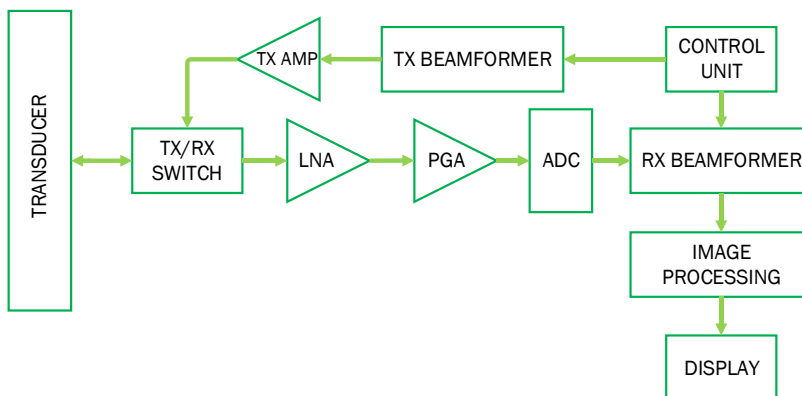


Fig. 2-8. General scheme of an US system.

The first device in the receiving chain is a switch that separates the transmission chain from the receiving chain. The ratio between the amplitude of the signals sent to the probe and those received can be up to 80 dB and the T/R switch therefore becomes fundamental to decouple them and avoid degrading the received signal. In many systems the switch and the multiplexer are replaced by a single device that integrates both functions, just to optimize performances.

The received signals are amplified by LNA (Low Noise Amplifiers), contained in the Analog Front-End, to obtain an electrical signal with the highest possible signal-to-noise ratio, which can then be processed in different ways depending on the chosen application. The processing of the pre-amplified signal is the responsibility of the dedicated programmable devices, i.e. DSP and FPGA (which are also used for signal generation). Their task is practically to apply numerical algorithms to the echoes received by the probes so that the information received is represented (usually using a PC) in a way that the user can understand.

The ultrasound signal can be represented in different ways. One is B-Mode, which consists of displaying in grayscale the information obtained by scanning a certain area. The speed and direction of blood flow can be represented by the Doppler Mode, which consists of the representation of the Doppler spectrum, and several variants of it. One of them is the Color Doppler Mode: a color scale is used to represent the direction of blood flow in a 2-D region. Another is the Color Flow Doppler Mode, where a two-dimensional region is superimposed on a B-Mode image, using a "multiple" encoding: for the blood direction different colors are used (red or blue), the brightness indicates the intensity (speed) and another color (green) represents any turbulent movements.

Another way of investigation that can be cited is the Harmonic Mode in which the properties of the medium under investigation are exploited: the non-linear characteristics of the target produce echoes with a different spectrum from that of the incident beam introducing, in addition to harmonic components at multiple frequencies, the so-called sub-harmonics, i.e. components with a frequency lower than the fundamental. With the received spectrum, knowing the transmitted one, it is possible to isolate the added components and characterize the medium through its non-linear characteristics.

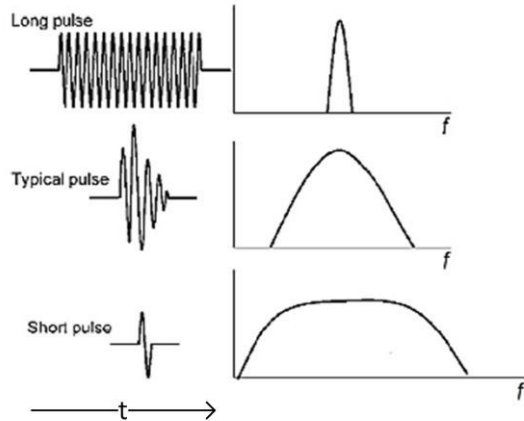


Fig. 2-9. Example of pulses in time and in frequency domain.

The different modes of representation of the ultrasound images are the basis for the choice of the type of signal to be used and, therefore, define the specific requirements for the devices in the chain of generation and transmission.

Given the dual function of transmitter and receiver of each element of the probe, the most commonly used signals are pulses or burst, or sinusoidal signals (or square wave) that last only a few periods of repetition. The duration of the burst is a very important parameter because it shows how long the transmission devices must remain active, determining their power consumption.

The length of the pulse (Fig. 2-9) determines other important factors. In fact, this aspect is closely linked, in addition to the band of the transmitted signal, to the energy radiated by the probe and therefore to the maximum depth of penetration. However, it should be noted that impulse compression techniques are often used to increase the energy and the signal-to-noise ratio.

The transmitted signal is generally a burst of a few cycles filtered to have a bell-shaped spectrum that helps devices downstream, in terms of Slew-Rate (SR), in the abrupt transition from zero signal to oscillating signal.

To carry out a two-dimensional scan, it is necessary to investigate the region along the main direction of the transmitted beam, i.e. deep in the middle, making a horizontal scan: this implies having to transmit the same burst several times, to receive all the echoes related to the targets

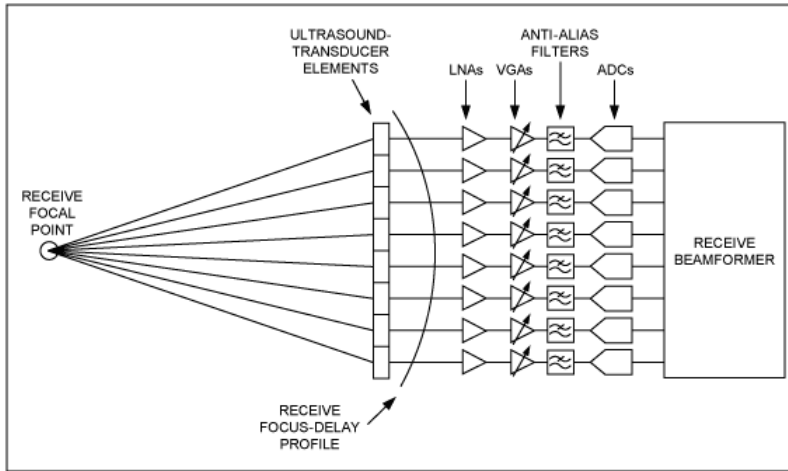


Fig. 2-10. US reception chain.

of the entire region of interest. The interval between two consecutive transmissions is called Pulse Repetition Interval (PRI). For power consumption it is necessary that the PRI is some orders of magnitude greater than the duration of the single burst, but this has the negative effect of increasing the total scanning time.

Although most of the signals used are time-finished signals, there are applications in which continuous signals are transmitted: this is the case of CWD (Continuous Wave Doppler) where a moving object is continuously targeted by a wave to receive the weak echo that is reflected and process it to extract the Doppler information.

In addition to the generation of signals, the programmable devices have the task of managing the electronic focusing of the beam. The beam of mechanical waves has a point of focus given by the composition of the individual waves and the intervention of the acoustic lens. Electronic focusing allows to modify the coordinates of this point in an almost arbitrary way, activating (or deactivating) specific transmitters and, above all, acting on the relative delays between the electronic signals transmitted to the various transducer elements.

During the reception phase (Fig. 2-10), the echoes received are processed through the operation of beamforming: the different length of the path that the waves must travel from the reflecting target to the individual elements of the probe, makes it necessary to apply time

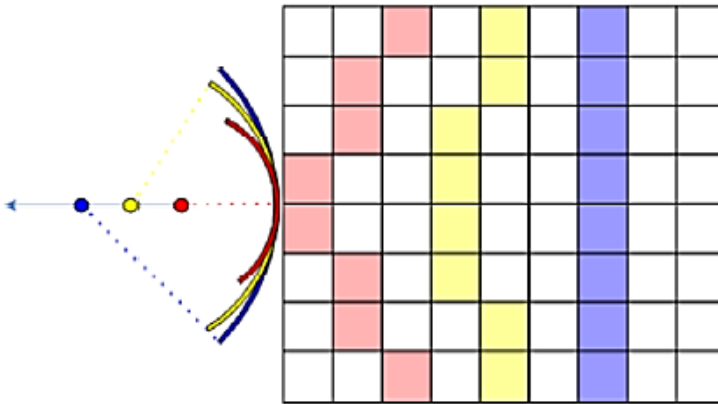


Fig. 2-11. Dynamic focusing scheme.

delays to the signals received. The delay to be applied varies depending on where the element is on the probe.

In fact, the delay applied to the signals received by the transducers closest to the target will be less than that of the receivers further away, so as to properly process the reflected echoes relating to the same transmission.

To scan a line, several transmissions are made by focusing on different points and a matrix of delays applied in transmission is then created for each individual element and for each point of focus. This matrix is applied by the digital devices that generate the signal and supervise the processing during reception. To reconstruct the total echo received, the delay matrix can be used, and the different signals can be added together in a coherent manner. The operation described is called dynamic focusing and an example is shown in Fig. 2-11.

The last block of the ultrasound system shown in Fig. 2-8 is the power amplifier (Tx Amp): the task of this stage is to amplify the low voltage signals coming from the FPGAs and bring them to values of tens of Volts suitable for the transmission of ultrasonic signals.



Fig. 2-12. ULtrasound Advanced Open Platform 256 (ULA-OP 256).

2.3. ULA-OP 256 system

One of the ultrasound imaging system used during this thesis work is the ULA-OP 256 (ULtrasound Advanced Open Platform).

ULA-OP (Fig. 2-12) is completely designed in the laboratory of Microelectronic Systems Design (MSDLab) of the University of Florence, but currently diffused in various research laboratories both in Italy and in the world (France, Great Britain, Sweden, Canada, Japan and China).

The great progress of modern electronics has made available devices such as FPGAs and DSPs with truly amazing features and computing powers at affordable costs.

This progress has contributed to the continuous evolution of specific frontends and computational systems in the field of ultrasound technology, i.e. to the dizzying growth of the potential of an imaging system in terms of increasing the fields of possible use and the quality of the results obtained.

ULA-OP belongs to this category of systems and is used in the field of scientific research for a variety of purposes ranging from the study of more efficient strategies for signal generation, to the development of more precise and faster investigation and processing techniques.

The key features that allow ULA-OP to be used in research to increase its performance are the accessibility of subsystems, re-programmability and modularity, or the ability to modify or expand the functionality of the system by simply replacing or adding appropriately designed electronic boards. These aspects make it reconfigurable for many applications simply through a partial reprogramming of digital devices and/or the replacement of one or more of its elements.

The ULA-OP 256 system [1] referred to specifically in this thesis is the result of continuous updates and optimizations made on the first ULA-OP 64 model, which will not be described in detail and for which please refer to [2].

TABLE I. ULA-OP 256 MAIN CHARACTERISTICS

General features	<ul style="list-style-type: none"> ▪ Open platform ▪ 32 to 256 independent TX/RX channels ▪ Size: 34 x 30 x 26 cm
Transmitters	<ul style="list-style-type: none"> ▪ 32 to 256 arbitrary waveform generators based on a 468 Mbit/s sigma-delta bitstream ▪ Max output voltages: 200 Vpp ▪ Frequency: 1 to 20 MHz
Receiver	<ul style="list-style-type: none"> ▪ Bandwidth: 1 to 30 MHz ▪ Analog gain: 2 – 54 dB with 0 to 40 dB programmable TGC ▪ 12-bit @ 78.125 MSPS ADCs
Beamformer	<ul style="list-style-type: none"> ▪ Programmable apodization and delays (dynamic focusing delay and sum beamformer, with resolution of 1/16 of the sampling period)
Processing modules	<ul style="list-style-type: none"> ▪ Coherent demodulation, band-pass filtering, downsampling, B-mode, multi-gate spectral Doppler, vector Doppler, etc (with the possibility to create new custom modules by the end user)
Storage capabilities	<ul style="list-style-type: none"> ▪ Up to 144 GB for RF (pre- or post-beamformed) and baseband data

ULA-OP 256 can manage individually and separately 256 channels of transmission and reception and therefore can be used with probes with a very high number of elements. This feature encourages to use matrix probes with which to perform three-dimensional scans faster and more effectively than linear probes, without having to move the probe mechanically.

Given the two-dimensional arrangement of the matrix probe elements, it is possible to use beamforming profiles that allow scanning both horizontally and vertically, as well as in depth.

The ULA-OP 256 system consists of a User Interface (UI) Board for interfacing with a PC and 8 Front-End (FE) Boards that handle all the operations for the management of 32 channels each.

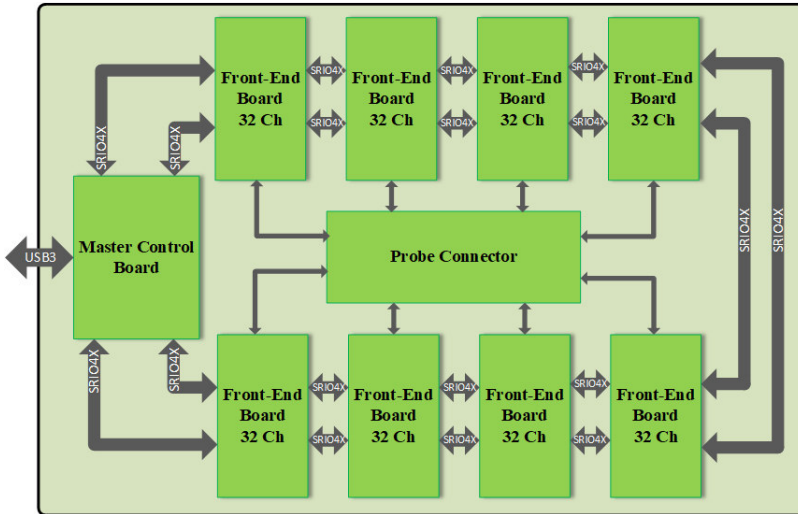


Fig. 2-13. General architecture of ULA-OP 256.

In the system there is another board that takes care of the power management. Starting from a 12 V power source, through DC/DCs controlled by a programmable controller, each card is supplied with the appropriate power supply for its operation.

The general architecture of ULA-OP 256 is shown in Fig. 2-13.

The Master Control (MC) Board is a board that manages the interface between the system and the PC for the transfer, via USB 3.0, and the display of data obtained from the processing of ultrasound signals received.

The MC card is also connected to the 8 FE modules in order to form a ring with bidirectional data flow as shown in Fig. 2-13. The communications are realized with Serial RapidIO (SRIO) architecture with 4 I/O lines. The capacity of the individual lines and the number of SRIO interfaces allow a total bandwidth of 80 Gbit/s full duplex for each module.

Each FE board is equipped with an FPGA of the ARRIA V GX family from Altera (Intel). Its main task is to generate 32 independent signals for each transducer during transmission and to focus the beam of the received signals.

The FPGA communicates, always through SRIO lines, with two DSPs (Texas Instruments TMS320C6678 devices) that receive data from the FPGA and deal with demodulating, filtering and applying all the numerical processing algorithms specific to the type of investigation carried out.

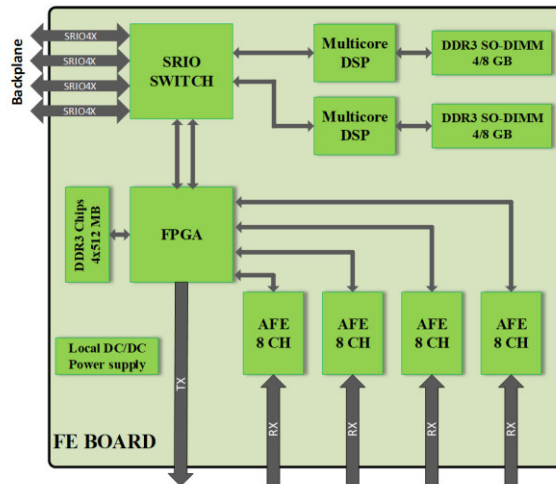


Fig. 2-14. FE board architecture.

All three programmable devices are equipped by DDR3 memories to allow the storage of the received signals and their subsequent reading by the user. The DSPs can use a memory of up to 8 GB each, while the FPGAs have at their disposal a bank of 4 memories of 512 MB.

The last blocks in the architecture of the 32-channel board, shown in Fig. 2-14, are the four AFE5807, devices for conditioning the received signals. They manage 8 channels each, in each chip are integrated 8



Fig. 2-15. FE board picture.

LNA (Low Noise Amplifier), 8 VGA (Variable Gain Amplifier) with variable gain in a range of 40 dB and 8 ADC (Analog to Digital Converter) that sample at 78.125 MSPS and quantize at 12 bits.

The physical realization of the board is shown in Fig. 2-15.

In addition to the DSPs and FPGAs already described, note the two 50x2 connectors, one on the right of the AFE chips and one on the left of the FPGA. These two connectors are intended for the connection of an additional board containing all the power electronics for the transmission and management of the T/R Switches.

The last module mentioned is the one that contains the external adapter for the various types of probe, fundamental given the nature of the ULA-OP research system: the ability to connect different types of probe, with different types of connectors, is a very important aspect. The solution adopted to solve this problem is the use of external adapters. This solution has the biggest flaw regarding the degradation of the signal-to-noise ratio, since the insertion of an additional external card can significantly increase the insertion of noise. For this reason, a completely shielded and replaceable probe adapter card has been developed inside the system. This board mainly contains the specific probe connector that relates to an array of shielded high-speed connectors, which fit into a corresponding array that is housed in the backplane board of the system. The adapter board can be replaced by simply detaching it from the backplane connector. This solution allows great flexibility in the choice of probes while maintaining an excellent signal-to-noise ratio.

2.4. Verasonics Vantage 256™

The other ultrasound system used during this work is the Verasonics (Kirkland, WA, USA) Vantage 256™ since it is used in many research laboratories like the Lyon one whereby my PhD in joint supervision has taken place.



Fig. 2-16. Verasonics Vantage 256™ system.

The Vantage 256™ (Fig. 2-16) is a research ultrasound scanner that uses proprietary hardware and software technology to give access to all the tools required in medical ultrasound research: access to raw ultrasound data and real-time imaging with custom software at clinical frame rates.

This is achieved through a software interface based on the MATLAB programming environment that can be used to integrate a custom transducer array, to incorporate a custom beamformer or to add user-defined image processing algorithms.

Furthermore, there is the possibility of connecting more system together to have the capability of directly control 2-D probes with more than 256 channels using a dedicated external synchronization trigger.

The main characteristics of the Vantage system are reported in Table II:

TABLE II. VANTAGE 256™ MAIN CHARACTERISTICS

General features	<ul style="list-style-type: none"> ▪ 256 independent TX/RX channels ▪ Size: L-49 x W-46 x H-48 cm ▪ Total weight: 35-44 kg
Transmitters	<ul style="list-style-type: none"> ▪ Arbitrary Waveform: Per-channel programming of tri-state transition timing on a 4 ns grid ▪ Programmable pulser voltage: 2 to 190 V_{pp} ▪ Frequency: 0.5 MHz to 20 MHz with standard configuration ▪ 2 to 42 MHz with High Frequency configuration ▪ 50 to 1500 kHz with Low Frequency configuration
Receiver	<ul style="list-style-type: none"> ▪ Frequency range: 0.5 MHz to 50 MHz with standard configuration ▪ 1 to 50 MHz with High Frequency configuration ▪ 50 to 1500 kHz with Low Frequency configuration ▪ 14-bit A/D converters with programmable sample rate up to 62.5 MHz
Beamformer	<ul style="list-style-type: none"> ▪ Patented algorithms to perform image reconstruction with highly optimized software
Processing modules	<ul style="list-style-type: none"> ▪ Conventional line mode ▪ Flash imaging (flat phase “plane-wave” imaging) ▪ Spatial compounding, frequency compounding ▪ High frame rate acquisition using unfocused transmission ▪ High frame rate “ultrafast” color Doppler ▪ Conventional color flow and power Doppler ▪ Plane wave color flow and power Doppler ▪ Conventional spectral Doppler ▪ Vector Doppler imaging capable ▪ Wide-area, multi-point spectral Doppler capable ▪ HIFU transmission with interleaved imaging ▪ Shear wave generation and visualization ▪ Real-time custom application processing on GPU ▪ 3-D volume imaging

Chapter 3. Hardware Development for CMUT probes

In this chapter are described my contributions to the design of the hardware required to perform 2-D and 3-D imaging with CMUT ultrasound probe. A brief introduction gives an access to the CMUT technology in the ultrasound field.

3.1. Contributions on Hardware Development for CMUT probes

Part of this chapter is based on the paper presented during an international conference:

- A.S. Savoia, B. Mauti, L. Fanni, G. Caliano, E. Boni, **P. Mattesini**, M. Scaringella, P. Tortoli, “A 120+ 120- Element Crisscross CMUT Probe's with Real-Time Switchable Electronic and Fresnel Focusing Capabilities”. IEEE International Ultrasonics Symposium 2018, Kobe, Japan.

All contributions are reported in Section 1.2.

3.2. Introduction to CMUT probes

Probes are a key element in an ultrasound system. As part of my research project, new types of probes will be used in addition to the standard piezoelectric ones. These new transducers are called Capacitive Micromachined Ultrasonic Transducer (CMUT). Their main advantages, compared to piezoelectric elements, are a much lower production cost and greater flexibility in making probes with arbitrary arrangement of the individual elements.

Obviously, however, being a relatively new technology has not yet reached the maturity and reliability typical of current piezoelectric probes. However, the potential advantages of CMUT technology justify the search for optimal solutions to make this type of transducer perform at its best.

3.2.1. Ultrasonic transducers

This section examines ultrasonic transducers, i.e. transducers capable of transforming electrical signals into mechanical oscillations and vice versa, and in particular piezoelectric transducers. Piezoelectric transducers have dominated the world of ultrasonic sensors since their invention until today. Thanks to the advent of micro-fabrication techniques, however, the possibility of creating electromechanical systems on a micrometric scale was born, giving rise to a new category of sensors: the Capacitive Micromachined Ultrasonic Transducer (CMUT) which are capacitive transducers micro-fabricated on silicon formed by arrays of electrostatic cells placed next to each other,

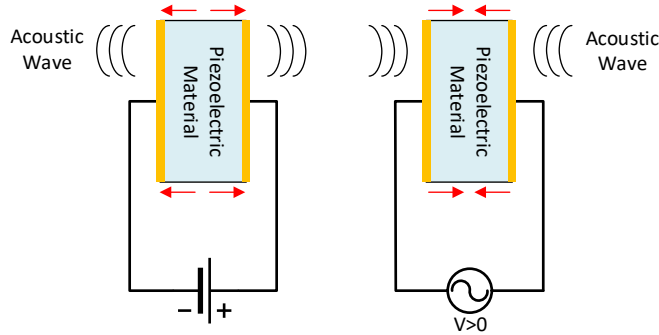


Fig. 3-1. Piezoelectric effect.

according to appropriate distributions. In the following paragraph the CMUT ultrasound transducers will be described more in details.

Piezoelectricity is a characteristic phenomenon of some types of crystals which, under tensile or compressive forces in a suitable direction, accumulate charges on their faces, as shown in the right part of Fig. 3-1.

This phenomenon is completely dual, since applying an electric voltage on the faces of the crystal, instead of a force, produces a deformation, giving rise to the reverse energy transformation. These materials are commonly used to generate and receive ultrasound waves.

The main characteristics of an ultrasound transducers are:

- *Bandwidth*: characterizes the transducer's flexibility in its ability to transmit and receive signals at specific frequencies. In particular, the percentage bandwidth is given by the following relationship:

$$\Delta B_{\%} = \frac{f_{max} - f_{min}}{f_0} \% \quad (3.1)$$

Where f_{max} and f_{min} are the frequencies for which the transducer amplitude response decreases by 3 dB with respect to the maximum value assumed at the center frequency (f_0).

- *Focal distance*: the focusing of the ultrasonic beam, generated by a transducer, is obtained with plastic lenses placed in front of it. The resulting beam shape is characterized by a proximal

zone, where the beam diameter is constant, and a distal zone, where the beam diverges. The focal distance is that which separates the transducer from the center of the proximal zone. For a circular probe of radius r , which operates at wavelength λ , focal length L , is given by the following formula:

$$L = \frac{r^2 f_0}{c} \quad (3.2)$$

- *Axial resolution*: is the minimum distance that must elapse between two targets lying in planes parallel to the direction of the US beam, in order to distinguish the contributions from each one. It is directly proportional to the transmission frequency and inversely to the duration of the transmitted wave packet.
- *Transversal resolution*: is the minimum distance that must elapse between two targets lying on planes perpendicular to the direction of the US beam in order to distinguish the contributions of each one.

3.2.2. Capacitive acoustic transducers

Transducers are appliances that convert physical quantities such as voltage and current onto strength and displacement. They can work in both directions transforming electrical quantities in mechanical one and conversely, but usually they are optimized to work in a preferred way. An interesting group of transducers are the capacitive acoustic ones: placing them in contact with a fluid generate propagation of elastic waves proportional connected to the voltage signals applied. Vice versa they can convert a mechanical displacement of the fluid in which an elastic wave is propagating into electrical signals.

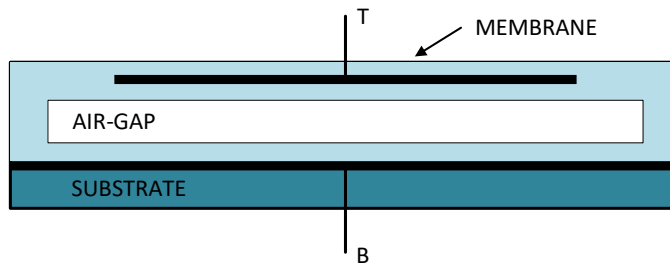


Fig. 3-2. Scheme of the section of an electrostatic cell.

The capacitive acoustic transducer is a capacitor with flat planes and parallel where the two facing themselves electrodes are separated from a void space. One of the electrodes is anchored to a rigid substrate instead the other one is partially anchored to the substrate and so it is partially free to move: Fig. 3-2 shows the scheme of a capacitive acoustic transducer. The two electrodes T (top) and B (bottom) are electrically separated: they are encapsulated in a dielectric material that constitutes the transducer structure. Changing the dielectric material properties is possible to change the dynamic mechanical properties of the mobile membrane that is the active acoustical part of the transducer. The dielectric material also has the function of avoiding short-circuit by accidental contact between the two electrodes.

Polarizing with a voltage difference the two electrodes T and B the two conductor parallel surfaces are charged. Since the charge accumulated in the two electrodes are equal but of opposite polarity an electric field appears in the separation zone of the electrodes (named air gap). As it is shown in Fig. 3-3 the electrostatic attractive force causes the deflection of the mobile membrane getting closer to the substrate. Such displacement is balanced from the elastic recall force generated from the membrane after the deflection. Increasing the voltage

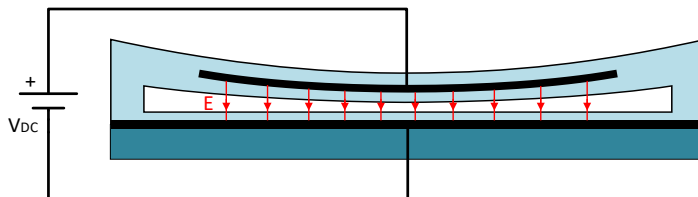


Fig. 3-3. Deflection of an electrostatic cell under a voltage polarization.

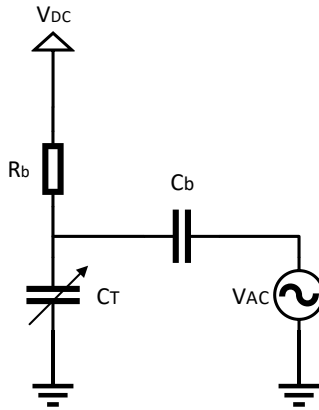


Fig. 3-4. Polarization circuit of an electrostatic cell.

difference between the two parallel conductors the electrostatic field increases accordingly up to a critical value (called collapse voltage) that causes the membrane to collapse on the substrate, touching it (when the elastic recall force is not strong enough to balance the electrostatic force). To let the membrane vibrate and generating acoustic waves is necessary to polarize it with a time varying electric voltage. Since the electrostatic force is always attractive is required to apply a continuous voltage and then add an alternate voltage. The continuous polarization voltage is also necessary to have an electric signal on the capacitor when the membrane is moved from the exterior. When an acoustic wave hits the elastic membrane, triggers the oscillation of the same, deforming the geometry of the electrostatic cell and, hence, varying its capacitance. In presence of accumulated charge on the two conductor layers, after a variation of the capacitance, it can be observed or a variation of the charge itself or a variation of the voltage difference between the electrodes. These variations can be revealed using appropriate electronic circuits connected to the capacitor.

The polarization circuit is shown in Fig. 3-4. The continuous polarization voltage is usually applied through a resistor with high impedance (R_b). To add also the alternate voltage a capacitor is used (C_b) which is also of high value. The capacitor C_b let the continuous voltage arrive only to the transducer and not to the alternate voltage generator.

3.2.3. CMUT technology

During 1996 Haller et. al. [3] presented an acoustic capacitive transducer working in air built using the micromachining construction procedure, the same one used from several decades for realizing micro electromechanical systems (MEMS). The goal was to use this technique in working the silicon to build a sufficiently small capacitive transducer, small enough to reach working frequency of the order of MHz with a good transducing efficiency. The transducer was micro-fabricated on silicon and formed by arrays of electrostatic cells placed next to each other, electrically connected in parallel, lateral dimensions of tens of μm and thickness of few μm . These dimensions bring to have very strong electric field in the air gap generating strong electrostatic force. The dimensions and the technical producing process gave the name to the transducer: CMUT (Capacitive Micromachined Ultrasound Transducer).

Later, Ladabaum et. al. [4], presented CMUT transducers working both in air and water showing the production technological process, the modelling and the experimental characterization. The results were very promising, and the flexibility offered by the planar technology of silicon suggested the possibility of realizing transducers for ultrasound applications.

In the years after many researchers have used then new CMUT technology in realizing ultrasound transducers: the results have been positive and comparable with the ones obtainable with the best

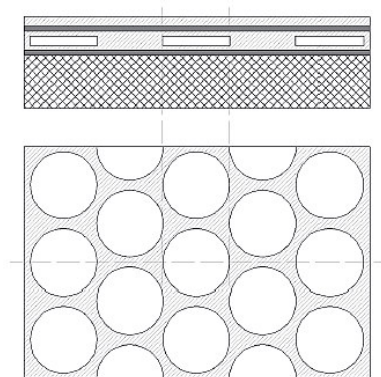


Fig. 3-5. Section view (top) and from above view (bottom) of CMUT cells distribution.

ultrasound probes currently on the market. The CMUT technology has shown its capability to be a credible alternative of the current piezoelectric material technology.

CMUT transducers are made of many active electrostatic cells of dimension in the order of μm . Usually the mechanical active part is made of a big number of membranes, of circular or hexagonal shape, working in parallel. The CMUT circular cells structure is shown in Fig. 3-5 (bottom): the cells centers are distributed so as creating 60° between them. The vertical structure of the CMUT is shown in Fig. 3-5 (top).

Exciting the circular membranes with an electric signal they are deformed depending from the excitation frequency.

3.3. Hardware development to interface ULA-OP 256 with CMUT probes

Initially the need was to make this new type of sensors usable within ULA-OP 256, an open ultrasound system for research purposes developed by the University of Florence.

To do this, it was necessary to expand the functionality of the ULA-OP 256 system to make it compatible with CMUT probes: this type of transducer to generate ultrasound, requires voltages of continuous polarization in the order of hundreds of volts that were not provided by ULA-OP. So, it was necessary to create a dedicated electronic to generate this supply voltages. This board also contains an FPGA and dedicated electronic components to configure the power supplies and to manage the control signals coming from the ultrasound system and directed to the probe.

3.3.1. Expansion electronic board for CMUT probes on ULA-OP 256.

A board intended to be connected to the ultrasound system that generates the high supply voltages (up to 250 V) has been designed using four switching power supplies configurable through an FPGA that has the function of driving and monitoring the operation of the designed board. Moreover, the FPGA allows to interpret the commands



Fig. 3-6. CMUT control and supply board picture: high voltage supplies circuits (red) and control circuits (light blue).

coming from ULA-OP and to forward them in an appropriate way to the electronics present on the probe body. The importance of the FPGA is also to have the possibility to connect different CMUT probes (in terms of geometry of the probe elements) that can be controlled realizing the appropriate FPGA firmware.

In Figure Fig. 3-6 is highlighted in red the zone that contains the circuits used to generate the 4 configurable high voltage supplies (up to ± 250 V, +200 V, -100 V). Instead in light blue is highlighted the FPGA MAX10 in the middle and the JTAG connector used to program the FPGA, on the right.

The top of the board was deliberately reserved for the FPGA so that it was far enough away from the high voltage lines and had enough space around it to route the many lines that need to be connected to it. In this regard it should be noted: the lines to the right are those that carry the control signals to the probe, the lines down carry the signals for driving and monitoring the high voltage supply circuits, those on the left instead receive commands for the probe elements from the ULA-OP system.

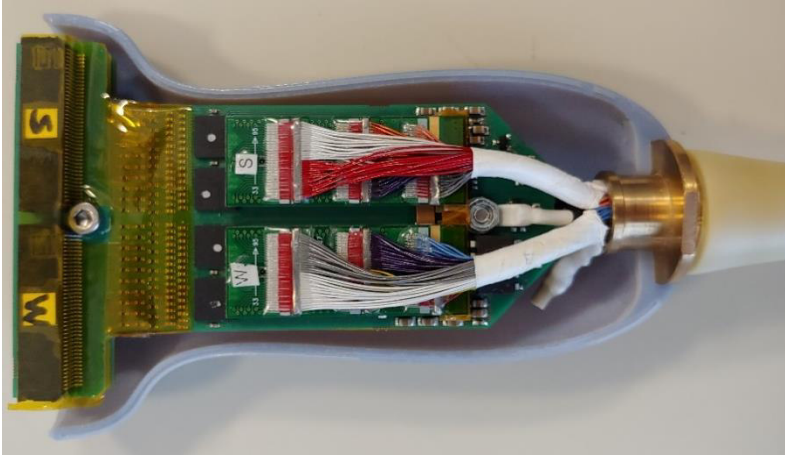


Fig. 3-7. LNA board (inserted in the probe handle) picture.

3.3.2. Electronic board development for 256 elements linear CMUT probe

In order to increase the quality of the images that can be acquired with the linear CMUT probe, it has been developed a board (Fig. 3-7), to be inserted in the probe body, that contains the Low Noise Amplifier MAXIM 14822, that provides a programmable gain from 0 to 9.5 dB. These amplifiers have been placed as close as possible to the probe elements. This allows to significantly increase the dynamics of the echoes received before they arrive on the cable to the ultrasound system. As it can be observed in Fig. 3-7 on the left there is the connector for the probe head (containing the CMUT elements, not present in the Figure), moving to the right there are the four LNA chips and in the right part of the image there is the probe cable.

The configuration of the LNAs is realized through a serial communication channel managed by the FPGA on the board described above, which also generates the high supply voltages required by the CMUT elements to properly work.

3.3.3. Acquisitions with linear CMUT probe with 256 elements

Once the hardware development was completed, then it was used to do ultrasound acquisitions with the linear CMUT probe to compare

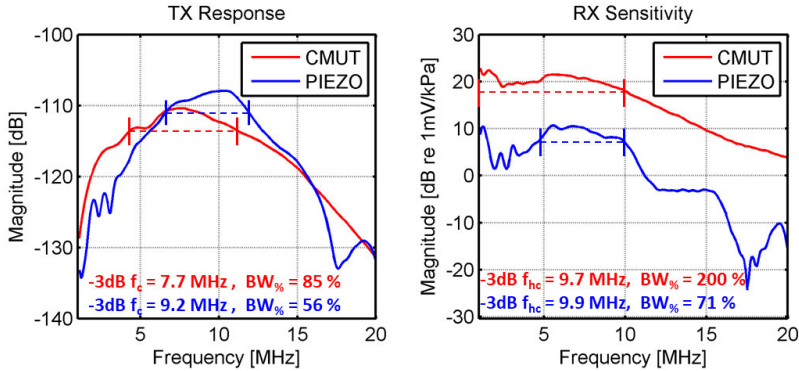


Fig. 3-8. CMUT peak sensitivity compared with commercial piezoelectric probe (ESAOTE LA523).

them with those done by a conventional piezoelectric probe (Humanscan 9LMQ linear 256 elements).

The probe used for the acquisitions has been entirely developed and realized by ACULab of Roma Tre University. This probe was used with ULA-OP 256 with an ad-hoc phantom for ultrasound studies.

The comparison in terms of transmission and reception performances of the CMUT probe and the Piezo one is shown in Fig. 3-8: as we can observe the CMUT probe permits to have a broader bandwidth in

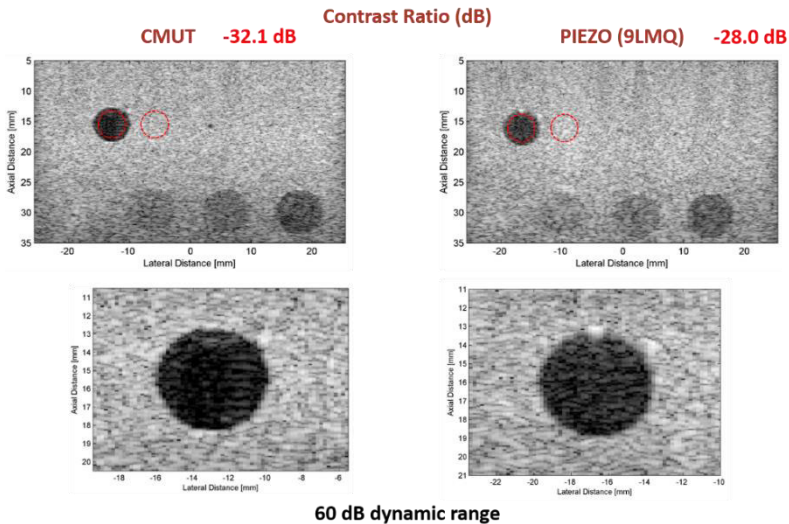


Fig. 3-9. Contrast comparison between CMUT (left) and piezo probe (right).

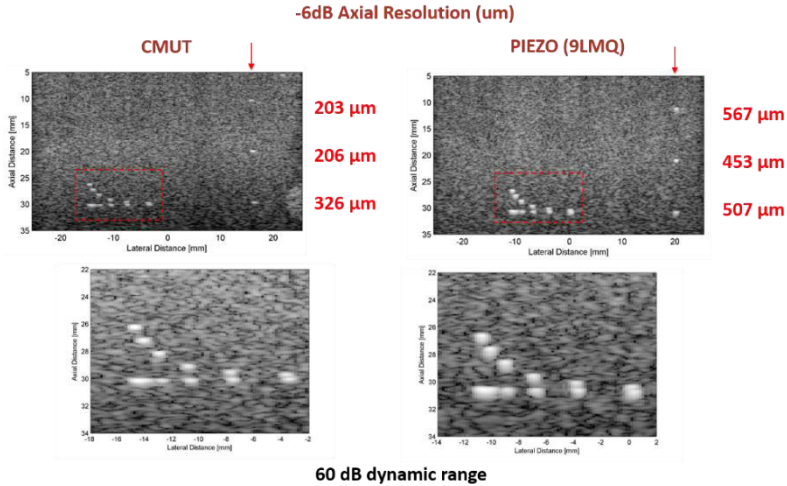


Fig. 3-10. Resolution comparison between CMUT (left) and piezo probe (right).

transmission and a better sensitivity in reception (of about 10 dB) and also wider frequency range, especially for low frequencies.

Then two different types of acquisitions have been made to evaluate the Contrast Ratio (CR) and -6dB Axial Resolution on a multi-purpose multi-tissue ultrasound phantom (CIRS 040GSE). The contrast results are shown in Fig. 3-9 and there is a clear improvement for the CMUT probe: the CR is 4.1 dB better comparing the anechoic cyst with the background tissue.

In terms of Resolution the results are shown in Fig. 3-10: also, in this case the advantages using the CMUT probe are clear, the resolution is better by about a factor of 2.

Anyhow, the hardware developed to drive CMUT probes with the ULA-OP system will be shortly employed in preliminary acquisitions with 2-D spiral CMUT arrays.

3.4. Realization of electronic board for testing a new 9-level ST Microelectronics pulser

This activity is part of a project in collaboration with ST Microelectronics for the development of new components for the transmission of ultrasound signals. These kind of pulser bring some advantages in terms of integrability and lower power consumption

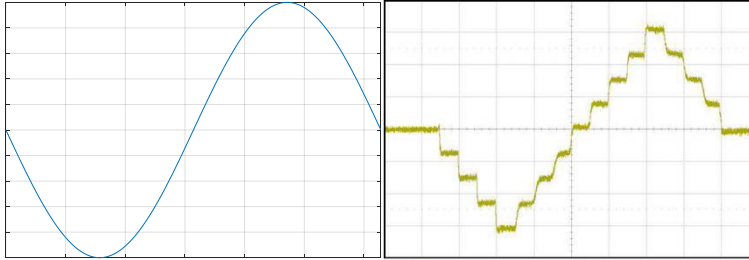


Fig. 3-11. Examples of transmission signals: linear (left) and discrete (right).

achieved using quantized transmission signals and not continuous as happens in linear transmitters. This also makes it possible to generate higher excitation voltages for the transducers while taking up less space. The negative side is that by sending quantized signals, unwanted harmonic components are also transmitted, in addition to the desired excitation, introducing disturbances on the signal. This type of transmitter is suitable for transducers with a limited band and therefore less sensitive to unwanted harmonics at frequencies higher than probe working frequency. In Fig. 3-11 is reported a comparison between a transmitted signal typically used for linear pulser and the shape of the ones send with the multi-level devices.

As part of this project I have designed a transmission board containing a transmitter that provides 9 different voltage levels (from -100 to +100 V using 25 V steps). Each component has four TX/RX channels managed by an FPGA that can be configured either through the ULA-OP system or in stand-alone mode using a PC.

The general architecture of the designed transmission board has been taken, for size reasons, from one of the boards already present in ULA-OP, the one containing the linear transmitters. This is because the available space where the transmission cards are inserted in the ULA-OP system is limited and therefore dimensional constraints exist. The transmission board was designed to be inserted in the Front-End card of ULA-OP system, as highlighted in the Fig. 3-12.

The main components allocated in the PCB are listed below:

- Multilevel pulser XMKD73A;
- Four MAX10 FPGAs with serial connection for the management of digital signals entering the chip;
- Connectors to the Front-End Board of ULA-OP 256;

- CDCVF855 clock distributor to provide the clock to all the main components;
- TPS51200 voltage regulator to generate 1.2 V necessary for FPGA cores;
- TPS7A8001 and TPS7A3301 voltage regulators to generate respectively +3.3 V and -3.3 V necessary for FPGAs and transmitter from +5.5 V and -5.5 V;
- Jtag pads needed to interface with FPGAs and program them via USB Blaster using Quartus™ software;
- N-channel Mosfets (ZXMN10A08E6) and P-channel Mosfets (ZXMP10A17E6) for the generation of the output voltages and the positive and negative references related to them;
- Gate Drivers UCC27525 (DGN) to drive the above mentioned Mosfets;
- SMLVT3V3 protection and stabilization diodes to generate the voltage references for the nine output voltages;
- Header for external power supply during stand-alone card debugging session.

Regarding the nine power supply levels to be provided to the device, it was decided to include a voltage divider in the project which, starting from +HV and -HV, the highest positive and the lowest negative voltage respectively, generates the remaining voltages in a passive way as to facilitate debugging and testing operations by significantly reducing the number of external power supplies. In addition, several

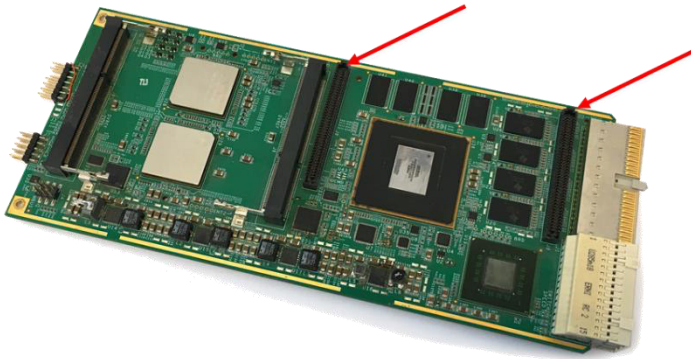


Fig. 3-12. Picture of FE board, red arrows indicate where the transmission board is inserted.

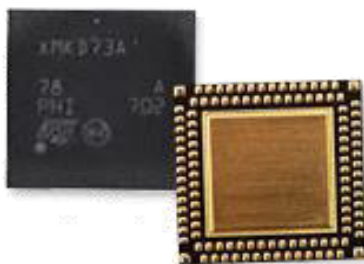


Fig. 3-13. 9-level transmitter chip.

high voltage capacitors have been inserted with the important function of supplying current and keeping the voltage stable during the transmission pulses.

The 9-level transmitter chip build by ST Microelectronics is shown in Fig. 3-13: its dimensions are $9 \times 10 \text{ mm}^2$ and the package is a Dual-Row QFN. The board designed to host the transmitter was realized using the software OrCAD Cadence (for the schematic design) and Cadence Allegro (for PCB design).

The circuit designed with OrCAD was imported on Allegro in order to place the components on the board, to which the relative footprints have been assigned, and proceed with the drawing of the tracks for the electrical connection.

Before proceeding with the routing, however, it is necessary to define the number of layers of the board and assign a specific function to each of them.

The stackup of an electronic board is important because it defines not only its performance in terms of electromagnetic compatibility with other ULA-OP elements, but also the integrity characteristics of the signals present on the PCB.

The treatment of problems related to EMC (ElectroMagnetic Compatibility) requires the use of Maxwell's equations and study of the type of connections (microstrips and/or striplines) as transmission lines. The signals that can be critical in terms of EMI (ElectroMagnetic Interference) are clocks and high frequency low voltage periodic signals. The solutions adopted for routing and stackup, such as keeping LVDS clock lines isolated, were considered enough to allow compatibility problems to be neglected.

The integrity of signals propagating on the lines, on both external and internal layers, is a subject that involves several aspects. In addition to the obvious thermal noise, the problems to be considered derive from phenomena such as crosstalk and switching noise. Crosstalk can be a problem in board areas where there is a higher density of connection tracks, and even more so if the lines are high voltage ones. To be considered is also the need to ensure adequate ground paths for RF signals: having to do with pulses with spectral content in the range of MHz, it is not possible to establish in advance what will be the paths of the signal to close to GND.

Finding solutions to all these problems at the same time is a difficult task, especially since it involves both technological and economic aspects. However, there are some general measures relating to one or more of the aspects described. One of them is to assign entire conductor planes to the various power supplies and ground and make sure that each routing plane is close to one of the GNDs. In this way, in addition to providing a ground closure to all lines, it is possible to shield more effectively the signals from electromagnetic interferences and decrease the crosstalk also acting on the thickness of the dielectric between the layers. A disadvantage in the use of these techniques is the difference in impedance (and therefore in propagation speed) between the lines on the external planes and the lines on the internal planes, which can cause



Fig. 3-14. UO256TX9L-1_0 board (top view).

problems when fast signals must pass from one plane to another. In order to avoid this phenomenon and to reduce EMIs, it is preferable to route the high-frequency signals exclusively, or almost, on the internal layers. Another technique used to minimize crosstalk and coupling problems is to route in such a way that the tracks on nearby planes are perpendicular to each other and the magnetic fluxes generated do not interlink.

Given the number of components to be connected, the number of power supplies and the type of signals that will be used, the solution adopted for the UO256TX9L-1_0 board was a twelve-layer stackup.

The realized board is shown in Fig. 3-14, Fig. 3-15 and it has these main characteristics:

- Dimensions: 139 x 82 mm²
- N. of layers: 12
 - 2 externals used for placing and routing
 - 4 internals for routing
 - 3 for ground
 - 3 for power supplies

Since that this card was a prototype there are some cables attached to test it in stand-alone mode without insert it inside the ULA-OP system.



Fig. 3-15. UO256TX9L-1_0 board (bottom view).

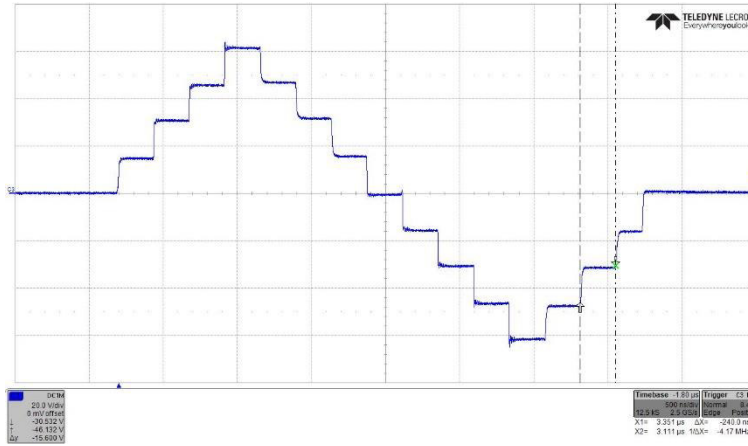


Fig. 3-16. Signal transmitted without resistive load.

The 9-level transmitter has been preliminary tested by Filippo Frosecchi (a former master student) during his thesis work in collaboration with ST Microelectronics. The board has been tested to verify both the electrical operation and the dynamic characteristics for use as a multi-channel transmission system capable of handling arbitrary signals with high amplitude.

The system clock was generated by a PXI of National Instruments at a frequency of 66.667 MHz (period of 15 ns) and amplitude 3.3 V for physical limits of the instrument.

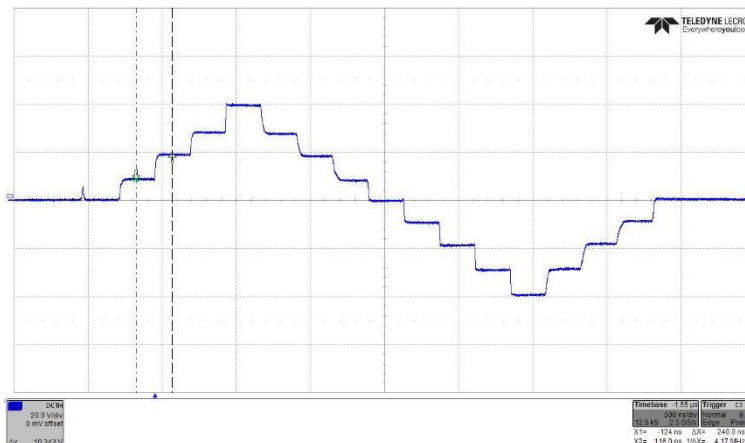


Fig. 3-17. Signal transmitted with resistive load.

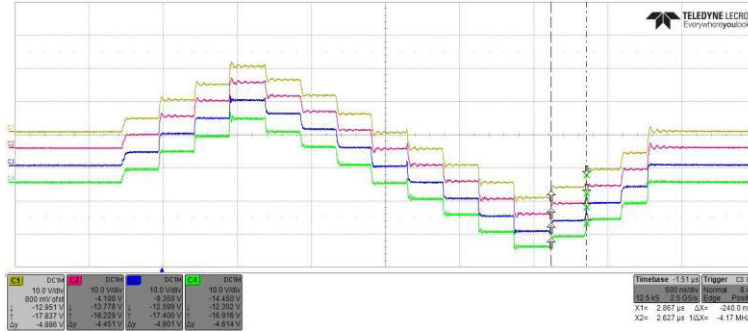


Fig. 3-18. Signal transmitted using 4 channels simultaneously.

In a first phase (without the presence of the 9-level transmitter) the power supplies provided and generated internally by the voltage divider were verified, using the dedicated headers to high voltages and the test points integrated on the board surface. After testing them using different values of +HV and -HV (± 20 V, ± 30 V, ± 40 V, ± 60 V, ± 80 V) the digital signals dedicated to the register related to the references were tested.

Once all references were tested, transmission evaluations could be carried out. For the initial phase it was decided to manage a single channel switching off the other three (testing the others one by one). Afterwards tests using all the channels together were performed obtaining good results in terms of obtaining the same behavior with all the channels. Examples of the tests performed are listed below, with

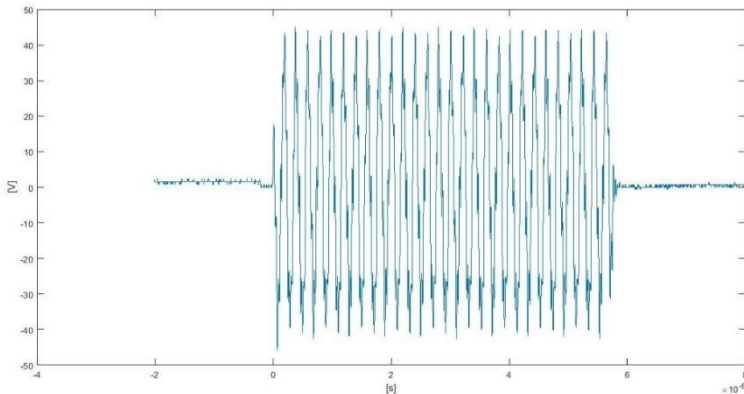


Fig. 3-19. 5 MHz sinusoid transmitted using an LA523 probe.

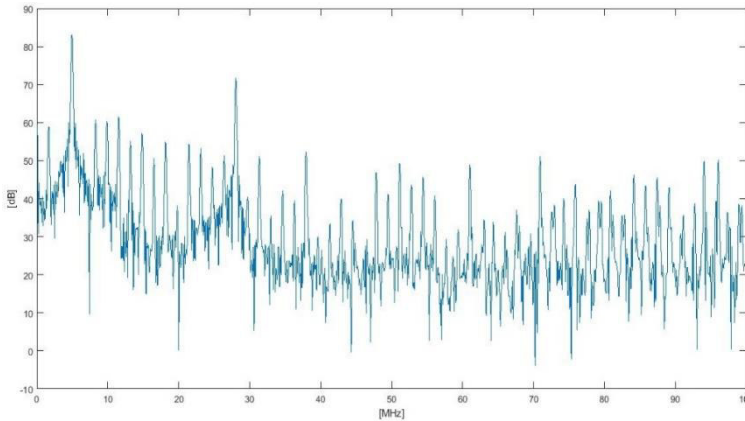


Fig. 3-20. FFT of 5 MHz sinusoid transmitted with LA523 probe.

power supply voltage +20 V, in floating mode without and with a resistive load:

- Construction of a complete sinusoid cycle using all 9 levels of available output voltage (without load Fig. 3-16 and with resistive load Fig. 3-17);
- Sinusoid cycle using all the four transmission channels together Fig. 3-18;

For the duration of the single states, in the first test phase we preferred to use a time of about 200 ns for each state in order to avoid excessive solicitations on the device with fast transitions between the different output voltage levels; not being sure of the complete stability of the device.

All the above tests were then repeated using a higher power supply voltage (+40 V) and investigating the behavior of the channels with a load of 300 Ω inserted on the board connecting to the output of the transmission chip using a jumper.

Additional tests were performed using the transmission board with a linear ultrasound probe LA523 produced by Esaote, with a working bandwidth from 4 to 13 MHz and a resonance frequency of about 7 MHz.

These tests have highlighted that the 9-level device has no difficulties in driving a reactive load as an ultrasound probe. Fig. 3-19 presents the acquisition, made using an oscilloscope, of a sinusoid at 5 MHz

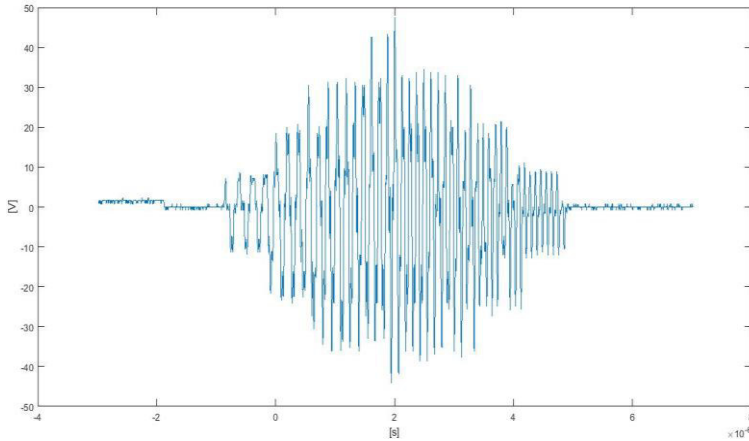


Fig. 3-21. Chirp with frequency sweeping from 3 to 10 MHz transmitted with LA523.

obtained measuring the signal present on an element of the ultrasound probe.

In Fig. 3-20 is displayed the FFT of the previous wave shape: the 2nd order harmonic distortion is about 22 dB.

The chirp signal transmitted in another test is shown in Fig. 3-21 and its relative FFT in Fig. 3-22. They present a good behavior also in presence of an ultrasound probe. The 2nd order harmonic distortion is about 30-35 dB that represents a positive result.

To conclude the tests, a comparison with an already tested solution on the ULA-OP 256 system was performed: some acquisitions were done

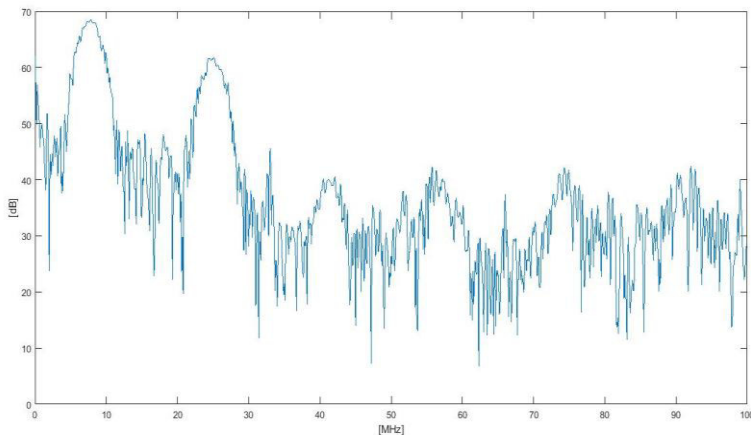


Fig. 3-22. FFT of the chirp with frequency sweeping from 3 to 10 MHz transmitted with LA523.

3 Hardware Development for CMUT probes

using the standard linear transmitters. Investigating a single channel connected to a single probe element and transmitting ten sinusoidal cycles at 5 MHz we obtained the results shown in Fig. 3-23 and the relative FFT in Fig. 3-24. The 2nd order harmonic distortion resulted of about 35-36 dB that is a coherent value with the one obtained with the 9-level discrete transmitter.

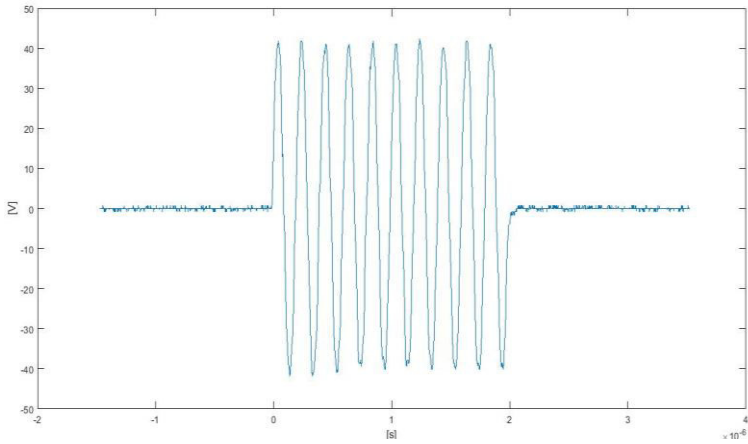


Fig. 3-23. Sinusoidal cycles at 5 MHz transmitted with the linear transmission board.

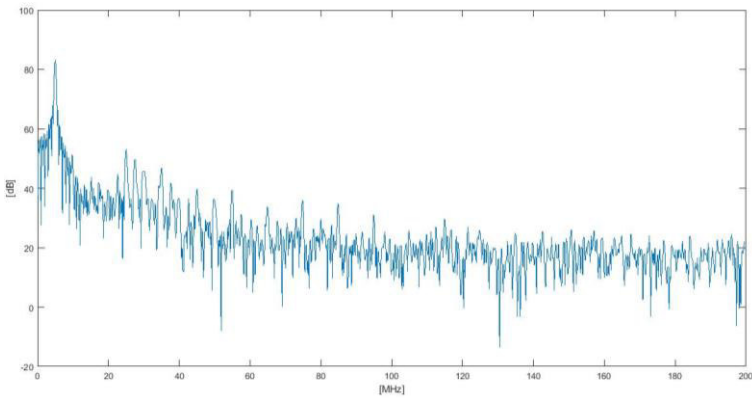


Fig. 3-24. FFT of sinusoidal cycles at 5 MHz transmitted with the linear transmission board.

Chapter 4. 3-D Imaging with Diverging Waves

In this chapter, 3-D acquisitions using a 1024-element array obtained by transmitting Diverging Waves are described. The used ultrasound scanner was formed by four 256-channel ultrasound systems that were synchronized together to drive the 1024-element probe. After a brief introduction on Plane and Diverging Wave transmitting methods, the influence of Virtual Source distribution on final image quality is discussed.

4.1. Contributions on 3-D Imaging with DW

Part of this chapter is based on the papers presented at two international conferences:

1. E. Roux, F. Varray, L. Petrusca, **P. Mattesini**, C. Cachard, P. Tortoli, H. Liebgott, “3D Diverging Waves With 2D Sparse Arrays: A Feasibility Study”. IEEE International Ultrasonics Symposium 2017, Washington D.C., USA.
2. **P. Mattesini**, E. Roux, E. Badescu, L. Petrusca, O. Basset, P. Tortoli, H. Liebgott, “Optimal virtual sources distribution in 3-D Diverging Wave Ultrasound Imaging: an experimental study”. IEEE International Ultrasonics Symposium 2018, Kobe, Japan.

All contributions are reported in Section 1.2.

4.2. Plane and Diverging wave theory

Ultrafast imaging represents one of the biggest improvements in medical ultrasound imaging in the last years. A lot of new applications for clinical (but not only) purposes are achievable thanks to the high frame rate obtainable both in 2-D and 3-D ultrasound imaging exploiting plane and diverging waves (PWs and DWs) transmission

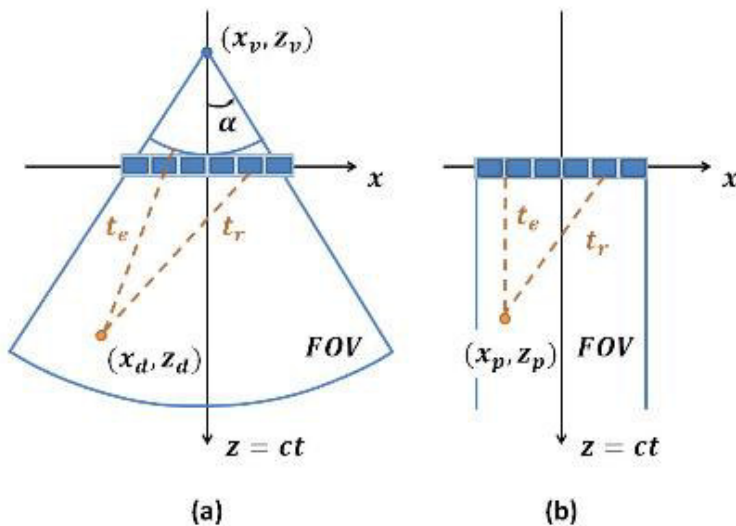


Fig. 4-1. Diverging Waves (a) and Plane Waves (b): scheme of the reconstruction of the TX/RX delays.

techniques. The trend for the ultrasound imaging in the next years will probably be to look at thousand images per seconds (or to several hundred using the compounding strategy to increase resolution and contrast in images got using PW or DW). A very important contribution to high frame rate imaging came from the development of GPU technologies that are required to process the amount of data produced by plane wave imaging.

Plane wave imaging represents a radical change in the medical US paradigm. These techniques aim at increasing the achievable frame rate (FR) by up to more than 100-times with respect to classic ultrasound imaging methods. Such high frame rates are suitable to observe very fast phenomena where the spatial resolution is less important than the temporal one. Some example applications are shear wave imaging, flow, contrast dynamics, and functional ultrasound imaging [5].

The idea is to reduce the number of transmission events required to construct an image to the bare minimum, to maximize the frame rate. The minimum reachable value is one transmission per image. In this extreme case the frame rate is limited only by the ultrasound wave speed in the imaging medium, influencing the required depth to be visualized, and by the computational time necessary to form the image. The basic concept is that the generation of a plane wave allows

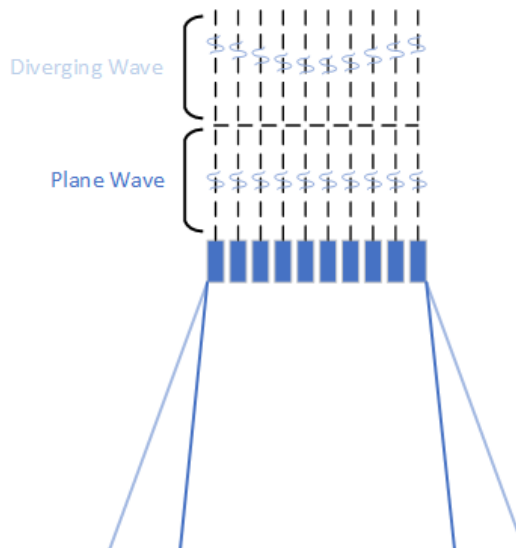


Fig. 4-2. Diverging Waves (top) and Plane Waves (bottom) transmission scheme.

achieving a wide and homogeneous ultrasound beam (as wide as the probe aperture). A simple way to send a plane wave is to excite all the transducer elements with the same signal in every transmission event. After a single transmission the echo signals permit to generate all the lines required to display an image. The echo-signals must be processed to align the phases associated to each receiving element and elaborated in parallel to generate multiple lines at the same time. The main drawbacks of this technique are the reduced pressure amplitudes compared to focused beams and the consequent reduced SNR and penetration depth. Furthermore, the plane wave imaging approach suffers from poor spatial resolution and contrast due to the maximization of the temporal resolution. The approach used to balance plane wave imaging performance is image “compounding” that mainly consists in averaging. A steering angle is used so that the wave is no longer moving only in front of the probe surface, it is also propagating following a given angle. Using different transmission angles in consecutive transmissions, and averaging the corresponding images, the compounded image is obtained. Through this approach the frame rate gain is reduced by a factor equal to number of used angles, but spatial resolution, SNR, contrast and penetration depth are increased. Nevertheless, to obtain the same quality of the standard beam forming methods the required compounding angles is quite high (in the order of 70 [6]) and the frame rate gain of the plane wave imaging technique risks to be lost. Anyway, the number of angles and the maximum steering angle are usually adjusted to adapt plane wave imaging to different applications.

Diverging wave imaging is essentially similar to the plane wave technique. The difference among the two methods is the defocused beam used in diverging wave transmission allowing a larger insonified zone. Also, in this case the image is formed by generating multiple lines in reception and by applying compounding algorithms. Most of the considerations made for plane wave imaging remain valid also for diverging wave. Considering the low-pressure generated by non-focused techniques in the transmission phase, they are not fitted for tissue harmonic imaging applications, where high-pressure acoustical waves are required to generate the harmonic components that are needed to construct the image.

4.3. Sparse arrays usage motivations

In both academic and industrial domain the interest on 3-D real-time ultrasound imaging by mean of 2-D arrays probe is currently under large investigation [7]–[9]. On the medical side this great interest on 3-D ultra-fast imaging is justified by the interest for cardiac applications [10]–[13] such as for heart strain assessment. Unfortunately achieving a sufficient volumetric data in a single heart beat to reach a satisfying temporal and spatial resolution it is not possible on current clinical US scanners [14], given the large amount of data provided by the high number of elements forming 2-D fully populated probes. Different techniques have been studied to reduce the number of probe elements to accordingly reduced the number of channels required in the US scanner to control 2-D arrays. An approach is to control a group of probe elements with a single channel, like happen in: micro-beamforming [15]–[23], row-column addressing [24]–[29] and channel multiplexing [30]. These techniques promise good results, but they also lead to a reduced control capability on the single element and less flexibility. Another approach is to reduce the element number on the probe head by mean of properly distribute them to optimize the acoustic beam: sparse array [31]–[36] can be designed to set the elements number to be controlled by an equal number of channels commonly available with up-to-date scanners. This solution can be used to have full access of the transmitted wave properties with the drawback of reduced Signal-to-Noise Ratio (SNR) and contrast losses due to the element reduction.

4.4. 3-D Diverging Waves using 2-D sparse arrays feasibility

The interest for high-frame-rate imaging has fostered the study of new strategies to design and to drive 2-D arrays for ultrafast 3-D imaging experiments. Driving each element of a 2-D array directly demands as many channels as the elements number (for instance: 1024 for a 32x32 array). This solution is feasible for only few research institutes (the Aixplorer systems at the Langevin Institute in Paris [37], the SARUS project at the Technical University of Denmark in Lyngby [38], the

parallelized Verasonics systems at the University of Lyon [39]) and is limited to 1024 elements/channels.

An alternative approach is based on 2-D sparse arrays that aim at obtaining good quality 3-D ultrasound images while reducing the number of channels to 128, 192 or 256 (the number of elements driven by standard ultrasound scanners), possibly without adding integrated circuits or multiplexing [40].

An experimental validation of this modality for 3-D ultrasound imaging was given using focused transmission modalities [41]. Three sparse array configurations with 128, 192 and 256 elements (called *opti128*, *opti192* and *opti256*, respectively) were extracted from a 32x32 full-gridded probe by using the simulated annealing approach [31], [40]. In this work, we investigated the feasibility of acquiring 3-D volumes at high frame rate by transmitting DWs while using the same *opti128*, *opti192* and *opti256* sparse arrays utilized for focused transmission.

It is worth noting that the paper by Flesch [24] claims that 2-D sparse arrays “geometry with large spacing between elements is not straightforward for the transmission of plane waves or diverging waves”. However, by leveraging the backward propagation principle [42] and using the time reversal principle, we may assume that if an array is optimized to produce focused beams, it may also produce well defined and artifact-less diverging waves starting from virtual sources.

To obtain all the images a standard delay-and-sum beamforming technique was used. Virtual source (VS) is a point source that produces the required diverging wave and was positioned following different schemes. From every VS an image was obtained. DWs propagate from the probe surface so its dimensions must be small enough to fit, for instance, the human intercostal aperture as requested for heart investigations.

4.4.1. Experimental setup

The array used in the experiments was a 32x32 elements probe with 3 MHz working frequency (72% bandwidth), having a square footmark with borders of about 10 mm. The single element size is 249 μm and the pitch is 300 μm in both x- and y-directions. The probe connection design was of the type one-element-to-one-channel: every element of

the 1024 was physically connected to a distinct channel in transmission and in reception.

To activate the desired sparse elements configurations, among the all 1024-element available on the 2-D array, we used a weighting map obtained by setting to one, the relative 2-D matrix positions, and, conversely, labelling with zeros the unwanted elements, aiming to have activated only the desired elements in both TX and RX phases when sparse distributions were used. No apodization was used.

Based on this binary weighting map, six array configurations (whose layouts are reported in [41]) were considered. Reference arrays were the full 32x32 matrix (ref1024) and the circular dense array (ref716) obtained removing the corner elements from ref1024. The optimized arrays, composed by 128, 192 and 256 elements, were obtained after 1280000 optimization cycles [40]. The 256-element random array (rand256) was obtained by selecting the best (in terms of the same energy function used for optimized configurations) among 1280000 random configurations. The role of rand256 is to compare it with opti256 and show the interest for the optimization routine when the same computational effort is used to obtain the two array configurations.

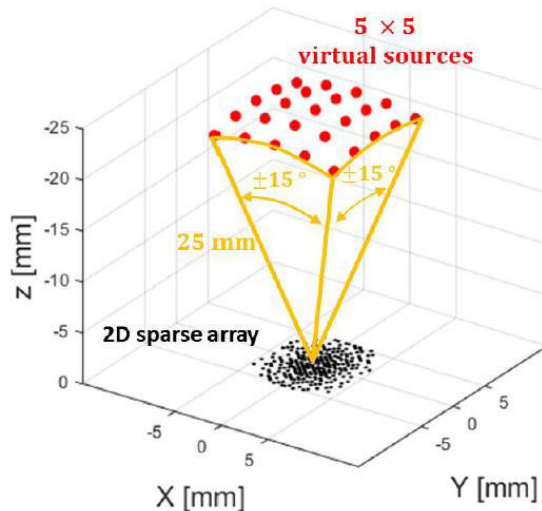


Fig. 4-3. Virtual Sources distribution behind the probe surface.

4.4.2. Acquisition sequence and phantom evaluation criteria

Four Verasonics Vantage 256 systems were connected to drive the 1024 elements of the array and to sample the echoes at 12 MHz. After defining the activation map (to activate the correct element distribution for each array) each array was excited with the same acquisition sequence. The sequence consisted on using set of 5x5 virtual sources positioned on a 25 mm radius sphere behind the array with span $\pm 15^\circ$ in both azimuth and elevation used to acquire compounded volumes (Fig. 4-3). Selecting the virtual sources distance from the array center at 25 mm is a compromise among different imaging objectives. Following the theory, they should be placed at 10 mm distance to obtain a theoretical field of view of about $\pm 30^\circ$ but the contrast would be considerably lower. Instead considering the sparse array optimization based on a TX focus at 40 mm, such depth may have been chosen, but in this case, the field of view would have been reduced by $\pm 7.6^\circ$, we have thus selected an intermediate focal point at 25 mm. Using the data

TABLE III. DW EXPERIMENTS PARAMETERS

Acquisitions parameters	
<i>Sampling frequency</i>	12 MHz
<i>Excitation signal</i>	3-cycle sine burst @3MHz without temporal weighting
<i>Virtual sources distance</i>	25 mm behind the array
<i>Virtual sources angle range</i>	$\pm 15^\circ$ in both elevation and azimuthal directions
<i>Compounding</i>	25 DWs/volume
<i>Reconstruction depth range</i>	15 mm to 70 mm
<i>Greyscale phantoms</i>	Gammex (Sono410 SCG), CIRS (054GS)
Transducer parameters	
<i>Central frequency</i>	3 MHz
<i>Bandwidth (-6dB)</i>	72 %
<i>Element size (squares)</i>	249 μm
<i>Pitch</i>	300 μm
<i>Elements apodization</i>	1 (activated) or 0 (deactivated)

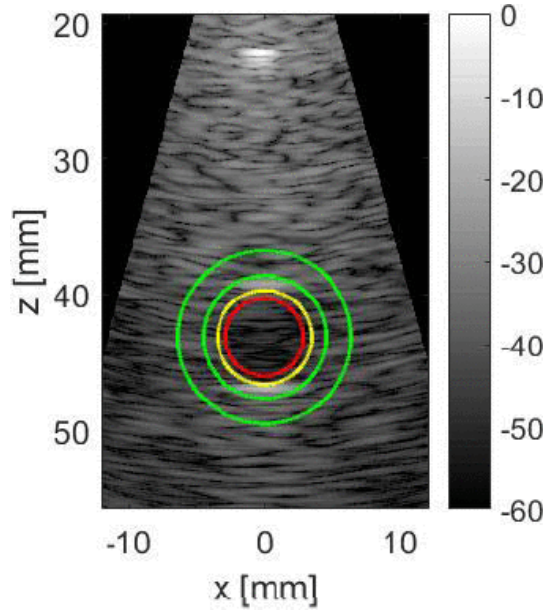


Fig. 4-4. Region of interest used to compute the CNR: the circular green crown highlights the background considered region and the red circle the cyst region.

acquired from different VSs and summing them coherently, an enhanced image could be obtained. This technique is called coherent compounding [10], [43] and takes benefit of constructive and destructive interferences (speckle) contained in ultrasound images to uniform the obtained image while maintaining the acoustic contrast. The transmitted signal was a 3-cycle 3 MHz sinusoidal burst for each used virtual source. The volumetric data extracted for each of the 25 virtual sources were averaged to obtain a 25-DW-compounded volume with improved resolution and contrast.

To achieve a 4 volumes per second rate, the maximum investigation depth was set at 120 mm and the PRF at 100 Hz. Each volume was reconstructed between 15 and 70-mm depth using a delay-and-sum beamforming method.

The parameters used for all the experiments are reported in Table III.

The adopted comparison parameters were the lateral resolution and the contrast to noise ratio (CNR), defined as follows:

$$CNR = 20 \log_{10} \left(\frac{|\mu_{bck} - \mu_{cyst}|}{\sqrt{\sigma_{bck}^2 + \sigma_{cyst}^2}} \right) \quad (4.1)$$

in which μ_{area} and σ_{area} are the mean and standard deviation, respectively, of the beamformed signal envelope (before the logarithmic compression) evaluated on the background (*bck*) and inside the cyst (*cyst*).

The comparison parameters have been obtained considering the XZ plane images acquired from a Gammex (Sono410 SCG) and a CIRS (054GS) phantom. To preserve the integrity of the images and to avoid

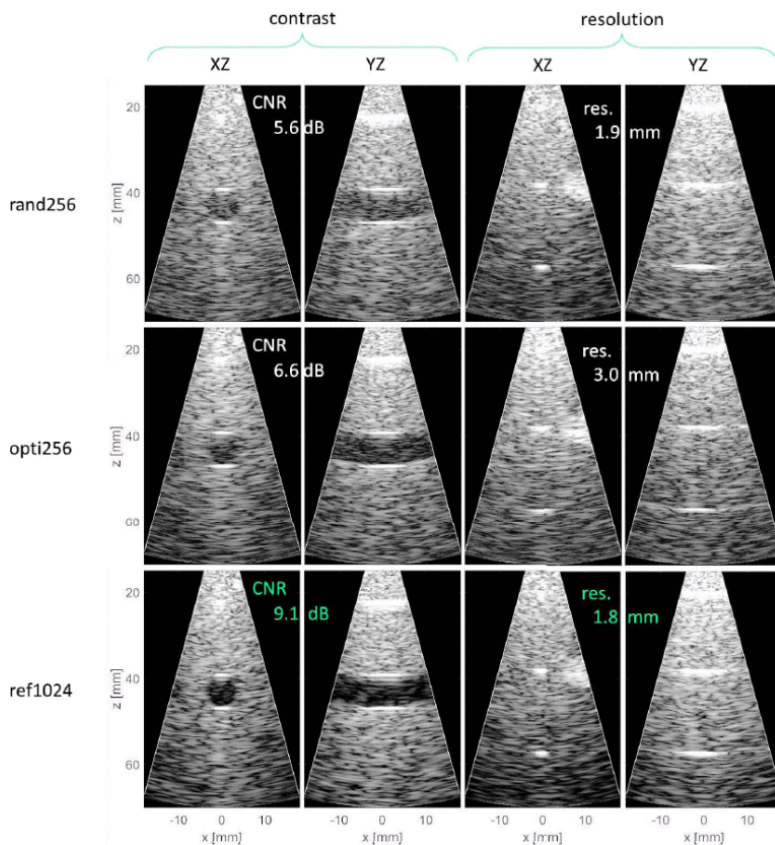


Fig. 4-5. 3-D images slices on XZ plane (first and third column) and on YZ plane (second and fourth column) acquired with rand256 (first row), opti256 (second row) and ref1024 (third row).

TABLE IV. CNR AND RESOLUTION RESULTS

	opti128	opti192	opti256	rand256	ref716	ref1024
<i>CNR (dB)</i>	2.8	1.4	6.6	5.6	9.8	10.7
<i>FWHM (mm)</i>	2.8	2.8	3.0	1.9	2.1	1.8

probe displacements between different acquisitions, the same position of the probe was maintained for all the array configurations in each sequence tested on the same phantom. The image quality was assessed through the full width at half maximum (FWHM) considering three scatterers positioned at 20-, 40- and 60-mm depth. In Table IV the average of the three values obtained from each tested array is reported. Concerning the contrast evaluation, the cyst region was confined by a circle of radius 2.9 mm. The outside region of the cyst was demarcated by an inner circle of radius 4.5 mm and an outer circle of radius 6.5 mm as shown in Fig. 4-4. Furthermore, the images were interpolated on 1000 (depth) \times 700 (lateral direction) pixels and visualized with a 60-dB dynamic range prior the evaluation.

4.4.3. Results

A qualitative assessment of the contrast is provided by the XZ and YZ 3-D image slices obtained in the contrast phantom reported in the first two column of Fig. 4-5. Both opti256 and rand256 perform good contrast imaging capability since the anechoic cyst at 40 mm depth is clearly distinguishable as for the image of ref1024 but by using only 25% of the probe elements. However, the noise inside the cyst is more evident for rand256 compared to opti256, especially on the YZ plane where the edges are clearer with opti256. The first row of Table IV reports the quantitative results highlighting that the best results in terms of contrast are given by ref1024 array (CNR of 10.7 dB). The CNR of opti256 is lower than the ref1024 one (by 4.1 dB) but results higher than rand256 one (by 1 dB) and also higher than opti128 one (by 3.8 dB). Unexpectedly opti192 array gave a CNR 1.4 dB lower than the one of opti128. The ref716 resulted very competitive with ref1024 showing a

CNR below ref1024 by only 0.9 dB but having at same time a very similar resolution performance.

A qualitative analysis of the resolution performance is given by the XZ and YZ 3-D image slices acquired on the resolution phantom shown in Fig. 4-5 (third and fourth column) for rand256, opti256 and ref1024. The opti256 provides a coarser resolution compared to ref1024 and rand256 since the three point spread functions are much broader. On the other hand, the resolution performance offered by rand256 is very similar to that of ref1024 since the scatterers look very similar. The quantitative results shown on the second row of Table IV, indicate that the best resolution is given by ref1024 (1.8 mm resolution on average over the three scatterers). The rand256 gives resolution performance coarser than ref1024 by only 0.1 mm. The optimized arrays (opti128, opti192 and opti256) present worst resolution than ref1024: +1.0 mm, +1.0 mm and 1.2 mm coarser respectively.

These experimental results have shown that 3-D DW imaging can be realized while reducing the number of channels by using DW through 2-D sparse arrays. Nevertheless, qualitative and quantitative comparison of six sparse arrays (optimized and random) did not fully validate that a sparse array optimized for focused imaging is still optimal in DW transmission. Actually, the rand256 demonstrated a good compromise between contrast and resolution by using only the 25% of the elements of ref1024; instead the optimized arrays (opti128, opti192 and opti256) presented resolution performance coarser than 50% of the ref1024 that are not balanced by the 1 dB CNR improvement (considering the best case of opti256) with respect to rand256. These results indicate that the optimization of 2-D sparse array configurations need to be further studied for 3-D DWs transmission.

4.5. Optimal virtual source distribution in 3-D Diverging Waves imaging

As highlighted from the previous activity the optimization strategy to properly distribute the array elements to achieve good performance in DW transmission need to be further investigate.

Former studies [40], [44] has experimentally demonstrated that sparse 2-D arrays are able to perform fast volumetric US imaging by

transmitting Diverging Waves (DWs). Since the ideal distribution of virtual sources (VSs) for DWs is still unclear with any kind of 2-D arrays, the goal of this work is to experimentally analyze to what extent the VSs distribution affects images acquired with a full-gridded 2-D array, a 256 random elements sparse arrays and a 256 elements sparse array optimized for focused mode transmission [31], [40].

4.5.1. Array configuration and transmission strategy

The same experimental setup, already described in 4.4.1 and 4.4.2, was used. The probe elements configurations selected to be deployed in the experiments are shown in Fig. 4-6.

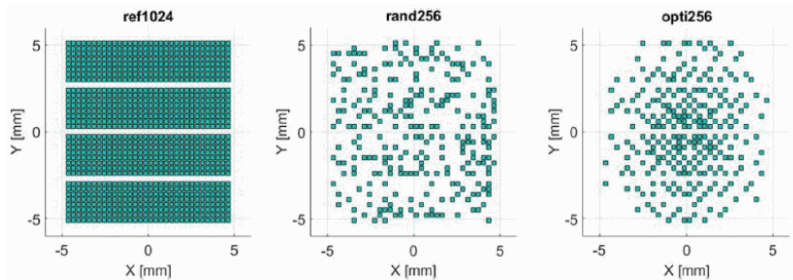


Fig. 4-6. Probe element distributions used: 1024-element full-gridded (*ref1024*), 256-element random (*rand256*) and 256-element optimized (*opti256*).

Each set of VSs may be considered as a virtual array. Two different VSs positioning strategies have been studied (Fig. 4-7): a regular structure on a grid and a sparse structure on a spiral grid, aiming to increase the SNR and to reduce grating lobes of the virtual probe. In the two instances the VSs were positioned at $d = 25$ mm and $d = 40$ mm behind the center of the probe surface varying the aperture angle from 60° to 120° . The acquisitions were made on a GammexTM (Sono410SCG) and a CIRSTTM (054GS) phantom. The images evaluation metrics were the lateral and the axial Full Width at Half Maximum (FWHM, the Contrast to Noise Ratio (CNR) and the Contrast Ratio (CR), defined as follows:

$$CR = 20 \log_{10} \left(\frac{|\mu_{bck} - \mu_{cyst}|}{\sqrt{\mu_{bck}^2 + \mu_{cyst}^2}} \right) \quad (4.2)$$

in which μ_{area} and σ_{area} are the mean and standard deviation, respectively, of the beamformed signal envelope (before the logarithmic compression) evaluated on the background (*bck*) and inside the cyst (*cyst*).

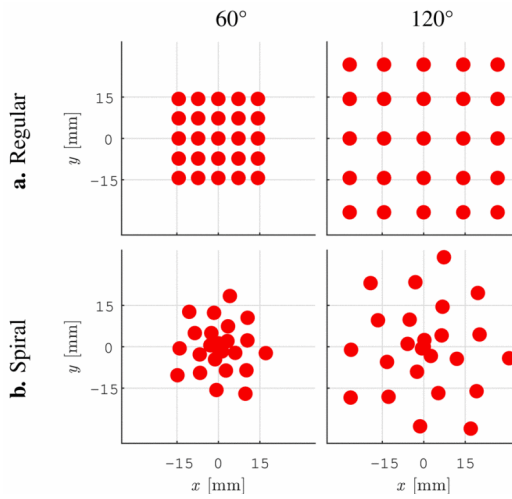


Fig. 4-7. Virtual source positioning strategies: regular (a) and spiral (b).

4.5.2. Results

The images obtained by scanning the XZ plane are reported in Fig. 4-8 for the $d = 40$ mm case. The contrast and resolution measurements results are presented in Table V.

In ref1024 a general enhancement of CR and CNR were achieved by using the spiral VSs positioning strategy instead of the regular one. For the axial resolution, approximately same results were obtained with all the tested VSs arrangements while the lateral resolution is resulted up to 0.4 mm coarser in spiral VSs distributions. Concerning opti256 the behavior is similar: better CR and CNR performance was obtained using the spiral VSs distribution. Poorer resolution performance was

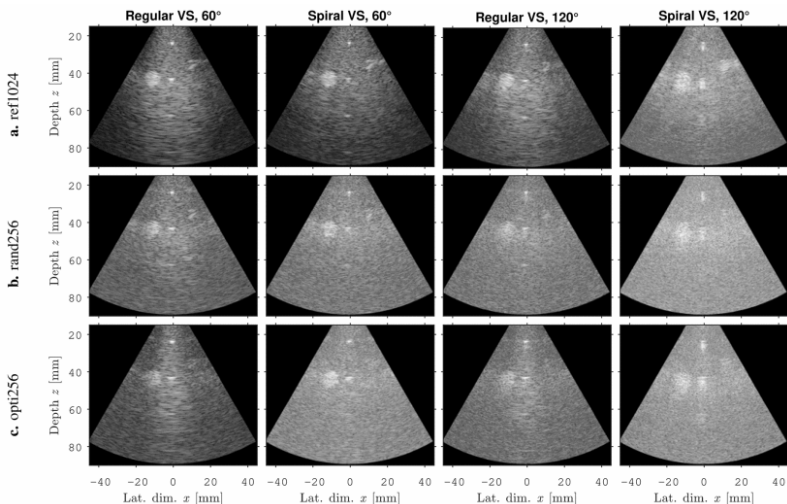


Fig. 4-8. Compounded images obtained from experimental data acquired with 25 VSs at 40 mm behind the probe surface (Dynamic = 60 dB).

observed: up to 0.3 mm coarser for the lateral and up to 0.1 mm in the axial case. The rand256 provided results close to the opti256 ones: spiral VS arrangements lead to better CR and CNR but decreased resolution, up to 0.4 and 0.2 mm coarser respectively for the lateral and the axial resolution.

In Table V a general comparison between all the three tested array configurations is shown. The contrast was generally enhanced by using a spiral VSs arrangement rather than a gridded one, but this was associated with both lateral and axial resolution degradation.

A fair assumption is that the contrast increasing is related to the reduction of the grating lobes when a spiral VSs distribution was used and the worsening of the resolution was due to the reduced VSs density at the borders of the virtual array.

For future studies it will be crucial to determine the optimal VSs number that will probably be a trade-off between contrast, resolution and the desired frame rate depending on the specific application. Determining an optimal VSs position through an optimization procedure may be done aiming to further examine the results in a deterministic way (like for regular and spiral distributions).

TABLE V. VSS DISTRIBUTIONS RESULTS

Ref1024 VSs d. 40mm				
	Mean Lat. Reso. [mm]	Mean Ax. Reso. [mm]	CR [dB]	CNR [dB]
Grid 60°	1,98	0,47	-8,8	-10,2
Grid 120°	2,13	0,44	-2,3	-15,4
Spiral 60°	2,39	0,47	-11,5	-8,8
Spiral 120°	2,29	0,45	-6,4	-11,0
Rand256 VSs d. 40mm				
	Mean Lat. Reso. [mm]	Mean Ax. Reso. [mm]	CR [dB]	CNR [dB]
Grid 60°	2,06	0,45	-3,0	-16,2
Grid 120°	2,06	0,58	0,4	-31,0
Spiral 60°	2,46	0,67	-5,5	-12,7
Spiral 120°	2,49	0,75	-1,1	-24,7
Opti256 VSs d. 40mm				
	Mean Lat. Reso. [mm]	Mean Ax. Reso. [mm]	CR [dB]	CNR [dB]
Grid 60°	3,11	0,44	-2,5	-17,5
Grid 120°	2,78	0,49	0,6	-27,9
Spiral 60°	3,35	0,55	-4,6	-16,6
Spiral 120°	3,14	0,47	-2,2	-19,6

Best (green) and worst (red) performances for each column are highlighted

Chapter 5. Spectral Doppler with 2-D sparse arrays

In this chapter a detailed comparison between 2-D full-gridded and sparse arrays in Spectral Doppler analysis is presented through both simulations and experiments.

5.1. Contributions on Spectral Doppler with sparse arrays

Part of this chapter is based on the papers presented at two international conferences and a journal paper:

1. **P. Mattesini**, A. Ramalli, E. Roux, L. Petrusca, H. Liebgott, O. Basset, P. Tortoli, “Spectral Doppler Measurements with 2-D Sparse Arrays”. IEEE International Ultrasonics Symposium 2018, Kobe, Japan.
2. **P. Mattesini**, A. Ramalli, G. Goti, L. Petrusca, O. Basset, P. Tortoli, H. Liebgott, “Spectral Doppler analysis with sparse and full 2-D arrays”. IEEE International Ultrasonics Symposium 2019, Glasgow, United Kingdom.
3. **P. Mattesini**, A. Ramalli, L. Petrusca, O. Basset, H. Liebgott, P. Tortoli, “Spectral Doppler Measurements with 2-D Sparse Arrays”. IEEE Transactions on Ultrasonics, Ferroelectrics, and Frequency Control, 2019.

All contributions are reported in Section 1.2.

5.2. Doppler Ultrasound principles

In ultrasonic flow investigations a key role is represented by the “Doppler effect”. When there are a transmitter and a receiver in relative movement, the “Doppler effect” is in the alteration of the frequency of the received wave compared to the transmitted one due to such movement. This phenomenon was described by the physicist Christian Johann Doppler in 1842 in an article named “On the colored light of double stars and other stars of the firmament”. The use of Doppler technique in the ultrasound field, aims at gathering information about the speed and the type of blood flow inside the vessels. An ultrasound probe is placed on the skin surface in proximity of the interested vessel. The ultrasonic waves are backscattered by the red blood cells that are in motion with respect to the probe and behave as isotropic scatterers for the acoustic waves. The region including the scatterers that contribute to the detected Doppler signal is defined “sample volume”. The echo signals produced by red blood cells within the sample volume are collected by the probe and processed by the ultrasound system.

The two most diffused systems in blood velocimetry are: continuous wave (CW) and pulsed wave (PW) systems. They differ in how the signal is transmitted and the echo-data are consequently elaborated.

CW systems use two transducers (one for transmission (TX) and one for reception (RX)). In this case, the sample volume is the area of intersection between the TX and the RX beam. There is no alternation between transmission and reception phases: ultrasound waves are continuously sent to the target and the echoes are continuously received. The CW technique cannot discriminate signals generated from different depths. The only information obtainable is about the global trend of velocity in the entire sample volume.

PW systems usually employ a single transducer that alternately act as transmitter and receiver. In TX, the transducer is excited by short pulses (burst pulses) generally made of few sinusoidal cycles. The transmission is repeated with a period of PRI seconds. Between two consecutive transmissions the transducer collects the echoes backscattered from different depths. Here, the sample volume is delimited by the region instantaneously occupied by the wave packet sent by the transducer. In the reception phase the sample volume is enlarged in the US propagation direction by the finite bandwidth of the probe and of the reception chain. The sample volume width is instead defined by the transverse dimension of the ultrasonic beam. By knowing the ultrasound speed in tissue, c , and the time interval Δt between the emission of the signal and the reception of an echo, the depth at which the echo was generated corresponds to:

$$d = \frac{c * \Delta t}{2} \quad (5.1)$$

5.2.1. Continuous Wave Doppler Systems

When a moving source transmits a continuous wave on a static receiver, if the movement is towards the receiver, the received frequency will be higher than the transmitted one, because of the higher number of the cycles hitting the receiver in the time unit. If the

movement is going away from the receiver the resulting effect will be the opposite: the received frequency will be lower than the transmitted one.

Considering the source moving at a speed v toward the receiver and defining with θ the angle between the velocity vector and the line that connects transmitter and receiver (θ is commonly defined as ‘‘Doppler angle’’) the relation between the transmitted frequency, f_t , and the received one, f_r , can be written as follows:

$$f_r = \frac{c}{c - v * \cos\theta} * f_t \quad (5.2)$$

If the receiver is moving and the source is still, the previous relation can be rewritten as:

$$f_r = \frac{c + v * \cos\theta}{c} * f_t \quad (5.3)$$

Considering the medical applications of ultrasound, the signal is transmitted from a still source (the probe) and is then backscattered by the red blood cells moving in the vessel. Red blood cells, in practice, first act as receivers and then as transmitters.

The frequency received by the probe is given by the combination of the two cases described above, conforming to the formula:

$$f_r = \frac{c + v * \cos\theta}{c - v * \cos\theta} * f_t \quad (5.4)$$

The Doppler shift is defined as the difference between the received and the transmitted frequency:

$$f_d = f_r - f_t = \frac{2v * \cos\theta}{c - v * \cos\theta} * f_t \quad (5.5)$$

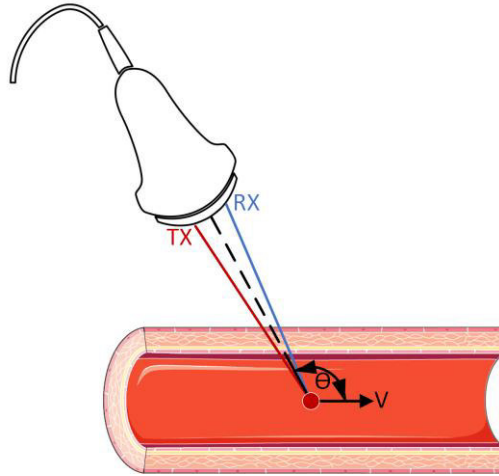


Fig. 5-1. Continuous Wave transmission scheme.

In blood, the maximum velocity is in the order of 2-3 m/s while the ultrasound speed in soft tissues reaches much higher values, typically about 1540 m/s. Being commonly $c \gg v$, it is possible to simplify the previous equation as follows:

$$f_d \approx \frac{2v * \cos\theta}{c} * f_t \quad (5.6)$$

5.2.2. Pulsed Wave Doppler Systems

PW systems emit one packet of ultrasonic energy for each Pulse Repetition Interval (PRI), i.e. with Pulse Repetition Frequency $PRF=1/PRI$.

Commonly, the PRI is longer than the length of transmitted pulses and the downtime between two consecutive transmissions is used to receive the pulse-echo signals. With reference to Fig. 5-2, the echoes backscattered from blood are received with delays proportional to the distance between the probe and the blood vessel, and inversely proportional to the ultrasound speed. If we sample the received signal, each sample is characterized by a specific delay from the end of transmission and corresponds to one investigation depth. The PW modality permits “gating” the echo-signal, so that it is possible to

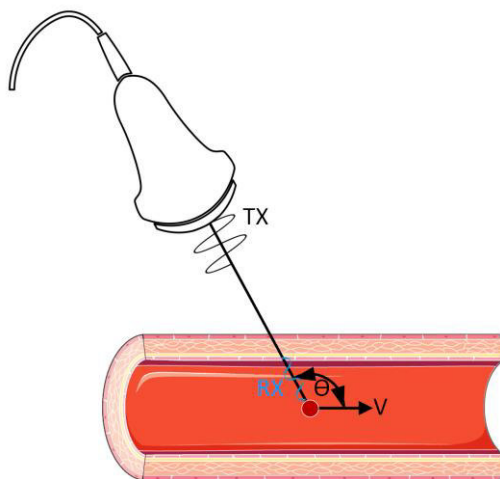


Fig. 5-2. Pulsed Wave transmission scheme.

distinguish the contributions from different depths. The samples obtained (after quadrature demodulation) from each depth in different transmission events are usually processed using an FFT (Fast-Fourier-Transform) to get information about the scatterers speed.

An accurate study of the two different approaches highlights that while in the CW case the velocity of the scatterers is related to a variation of the received frequency (compared to the transmitted one) namely that is a real Doppler effect, while in PW case the information about the scatterers velocity is contained in the variation of the phase of the pulse-echo signal between consecutive transmission events. Even though the relation between the target velocity and the Doppler shift is the same as in CW, and is still regulated by eq. (5.6), there are some important differences among the two methods that cannot be underestimated [45]. In PW Doppler, whichever is the investigated depth, the echo-signals are inherently sampled at PRF rate. According to Shannon's theorem, to avoid aliasing effects, it is possible to recover the correct velocity of the scatterers if they produce Doppler shifts lower than $PRF/2$. Furthermore, some effects concerning US propagation (like frequency-dependent attenuation) can affect the shift Doppler in CW case much more than PW case.

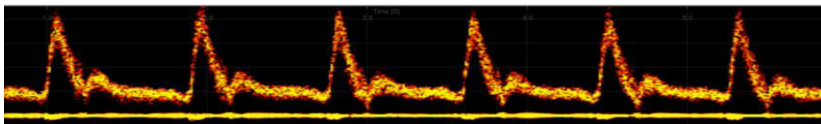


Fig. 5-3. Spectrogram example relative to the center of the Common Carotid Artery.

5.2.3. Single- and Multi-Gate PW Doppler

Most commercial ultrasound systems can work in PW Doppler mode. Almost all of them carry out the Doppler PW information from one single depth at a time. This approach allows to display the temporal variation of the Doppler spectrum associated to the desired depth. The resulting figure is shown in Fig. 5-3 and it is commonly called Spectrogram (or Sonogram). This representation gives immediate information about the time behavior of the blood velocity but does not show any detail about the velocity profile on the vessel section under analysis.

Another possibility offered by the PW approach is the Multi-gate analysis [46] that simultaneously evaluate the flow speed at multiple depths. The Multi-gate modality first collects the samples of the demodulated echo signals in a time domain matrix. The term “Fast Time” is usually associated to the samples collected from different depths within the same PRI (e.g., the samples in a matrix column), and “Slow Time” is usually associated to the samples collected from the same depth at different PRIs (e.g., the samples in a matrix row). The FFT algorithm is applied to NFFT points accumulated along each Slow Time direction. When all the spectra, sorted by depth, are reported in a color scale we get the spectral profiles. The scheme reported in Fig. 5-4 describes the required steps to obtain the spectral profiles.

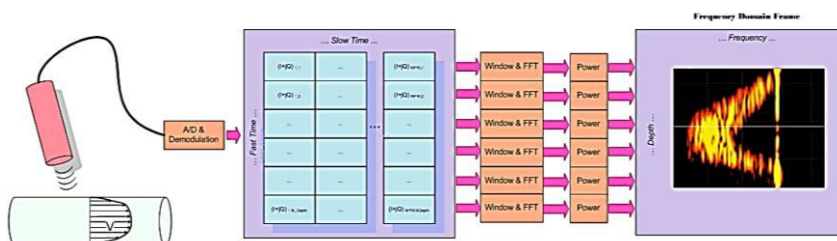


Fig. 5-4. Multi-gate Doppler technique scheme.

5.3. Doppler spectrum width

Based on the Doppler equation, from a theoretical point of view we may think that the spectrum associated to a single moving scatterer is made by only one frequency component, leading to a Doppler spectrum formed by a single line. The observation of real Doppler spectra suggests a different conclusion: they have a finite bandwidth, and this involves a certain ambiguity in flow velocity estimation using ultrasonic Doppler.

Many studies have been carried out since 1970 to determine the causes of this phenomenon and they have highlighted that the causes are multiple and presenting different consequences on Doppler spectrum.

5.3.1. Velocity, transit time and geometrical spectral broadening

Velocity broadening is the first aspect that impacts on the broadening of the Doppler spectra. This is a phenomenon related to the size of the sample volume. The flow inside a vessel is typically characterized by the presence of red blood cells moving with different velocities depending on their position. Almost unavoidably, targets with multiple velocities are intercepted within the sample volume. Thereby, the resulting received signal is an integration of several velocity contributions. This leads to different frequency components in the Doppler signal, depending on the velocity gradient within the sample volume.

Another element that contributes to velocity broadening is the non-stationary movement of scatterers whose speed change during the observation time (which corresponds to the number of PRIs over which the FFT is evaluated) further enlarging the spectrum. This aspect is more present during the systolic acceleration of blood flow.

Another phenomenon that contributes to broadening of the Doppler spectrum is the Transit Time, which was first studied by Vermon L. Newhouse [47], and considers the duration of the path of a scatterer while crossing the sample volume.

The transit time, t , i.e. the time needed by a scatterer to cross the sample volume, is coincident with the duration of the echo-signal associated to such scatterer, in the slow-time domain. The relative

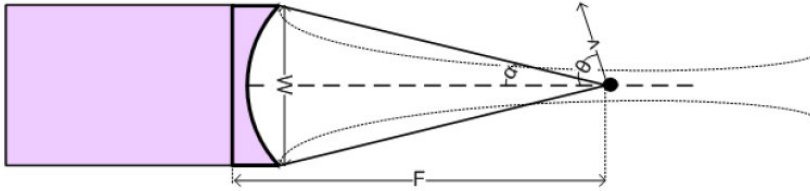


Fig. 5-5. Geometrical broadening in the transducer focus.

Doppler bandwidth is approximately equal to $1/t$. Newhouse observed that the non-uniform field typically associated to focused beams provides an amplitude modulation to the echo signals, further enlarging the Doppler bandwidth. The bandwidth increase associated with the Transit Time is hence determined by the path covered and by the non-uniformity of the acoustic field in the sample volume. The Doppler angle, in particular, influences the transit time.

The widening of the Doppler spectrum can also be interpreted in terms of “Geometrical broadening”, which has been studied still by Newhouse. To see the nature of this contribution, refer to Fig. 5-5. In focused beams, the Doppler angle among the direction of the target and the ultrasound one, does not have an unambiguous value. According to the so-called ray approximation, each focused beam can be seen as given by the contributions of multiple rays, each propagating with a different direction, i.e., with a different Doppler angle. Each of these rays give a different Doppler shift, thus enlarging the final bandwidth.

The equivalence of the Geometrical Broadening and the Transit Time was firstly demonstrated by Edwards in laser Doppler systems [48].

Afterwards Newhouse proved that this equivalency was valid also in ultrasonic Doppler flow-metering showing that these two aspects were in reality two different interpretations of the same phenomenon and that is only required to consider one of the two in theoretical estimation of the Doppler bandwidth [49]. Especially, the equivalence was demonstrated valid in the focal region of a transducer and for Doppler angles close to 90° .

Generally speaking, we refer to Intrinsic Spectral Broadening (ISB) to indicate either the transit time and the geometrical effects that contribute to the enlargement of the Doppler bandwidth. All the aspects related to ISB and how they impact on the Doppler spectrum, have been

studied as possible artifacts causes in velocity measurements, as well as possible source of additional information [50].

We describe here the theoretical estimation of the Doppler bandwidth due to the ISB related to focal depth when a focused wave is transmitted [51]. Let us consider the geometric approach and the configuration in Fig. 5-5. The Spectral broadening is here associated to the ambiguity of the Doppler angles, that assume several values sweeping from a minimum to a maximum value:

$$\theta_{min} = \theta - \alpha; \theta_{max} = \theta + \alpha \quad (5.7)$$

It can be geometrically demonstrated that the Doppler bandwidth will be equal to:

$$B_D = \frac{2 * f_t * v}{c} * 2 * \sin\alpha * \sin\theta \quad (5.8)$$

That is, for $F \gg W$:

$$B_D \simeq \frac{2 * f_t * v}{c} * \frac{W}{F} * \sin\theta \quad (5.9)$$

The above-mentioned relation is very important in Doppler spectra bandwidth measurements and permits to make some interesting general considerations regarding the Doppler bandwidth, like:

- The bandwidth is directly proportional to the W/F ratio, to the scatterers velocity and to the transmission frequency;
- For given flow and transducer parameters, the maximum bandwidth is achieved when the flow direction is perpendicular to the ultrasonic beam;
- It is possible to estimate the maximum frequency of the Doppler spectrum due to the ISB, as follows:

$$f_{max} = f_D + \frac{B_D}{2} \quad (5.10)$$

where f_D represents the Doppler shift frequency.

It is important to consider what has reported in literature [52], i.e. that the maximum Doppler spectrum frequency does not depend on the

velocity range contained in the sample volume, but only on the maximum value of that range.

5.4. Preliminary Spectral Doppler measurements with 2-D sparse arrays

Spectral Doppler analysis [53] still acts as the reference ultrasound technique for quantitative blood velocity estimation [54]. It is commonly used in cardiovascular imaging [55], e.g. for the evaluation of artery stenosis or regurgitation of the mitral valve and obstetrics [56].

Current progress in 3-D ultrasound imaging lead, potentially, to extend Doppler analysis, previously limited only on a planar zone, towards any point belonging to a volume. This aspect would be valuable in many applications, like in carotid artery investigations, to achieve the correct reconstruction of 3-D morphology of the plaques that are not adequately described through standard B-Mode imaging [57]–[59].

In recent years, many efforts were put in the development of innovative 3-D vector flow imaging methods [60]–[63], but their experimental applications are restricted yet.

3-D real-time ultrasound imaging requires 2-D array probes that typically have a huge number of elements that imply the occurrence of several problems like connectivity ones, cable size, power consumption, cost and computational load for the ultrasound scanner. Furthermore, 2-D probes are commonly organized in regular grids. Such elements are usually controlled by applying a specific integrated electronics (ASICs) in sophisticated ultrasound scanners [21], [64] or by employing row-column addressed arrays [27], [65] resulting to be quite expensive solutions.

As discussed in Section 4.3, a promising addressing to these issues is to utilize 2-D sparse arrays [32], [35], [36], [66]: a reduced number of elements is spread on the probe surface following specific geometries to optimize the acoustic beam transmission/reception properties. The appropriate arrangement of the elements can be obtained using optimization algorithms such as simulated annealing [31], or utilize the geometrical properties of Fermat’s spiral [67]. These non-regular probe elements distributions are appealing in terms of costs (not needing expensive ASICs, neither involving connection problems), and in

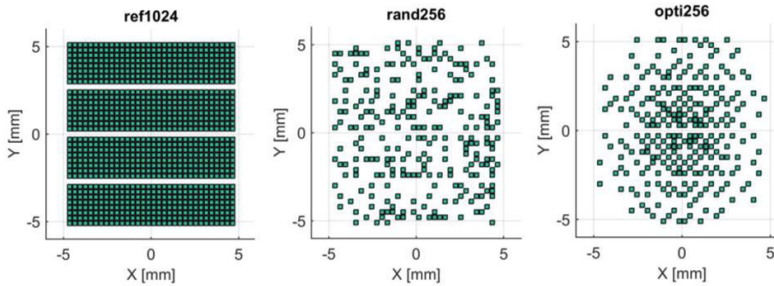


Fig. 5-6. Probe elements distributions used: 1024-element full-gridded (ref1024), 256-element random (rand256) and 256-element optimized (opti256).

flexibility terms (having the possibility to independently control all probe elements through the associated scanner).

Sparse arrays have been already used in some imaging tests [44], [68] but their capability to be used in Doppler investigations is not broadly stated in literature. Spreading the probe elements may distort the acoustic field adding radiation lobes in unwanted directions. This may affect the signal to noise ratio, the average Doppler frequency and the bandwidth of the Doppler spectra. The purpose of this study was to experimentally evaluate to what extent using sparse arrays instead of the full gridded ones influences the spectral Doppler assessments.

5.4.1. System and arrays used

Four Vantage 256 systems (Verasonics, Kirkland, USA) were synchronized and utilized together to get a 1024-element system [39]. The scanner channels have been individually linked to each of the 1024 elements of a 2-D probe operating at 3 MHz (Vermon, Tours, France). The system channels were independently connected to the elements of the full-gridded array through 8 connectors. The ultrasound system was set up to be able to configure and utilize three specific sets of probe elements arrangements (shown in Fig. 5-6):

- 1) the whole 1024-element array (named ref1024);
- 2) a sub-group of 256 elements randomly chosen (rand256);
- 3) a different sub-group formed by 256 elements selected through an optimization procedure (opti256).

All the details about the optimization of the elements positions are reported in [40], but, briefly, the opti256 structure has been selected

according to the simulated annealing algorithm to generate a proper acoustic field at 4 cm depth. Concerning rand256, its elements selection is the best random distribution reached using the same number of iterations used to choose opti256 but excluding any intelligent decision on the element selecting process between consecutive iterations. Hence, ref1024 serve as the reference full gridded array, meanwhile the other two represent the sparse arrays case, designed following two different methods.

The used phantom was a tissue mimicking rotating disc (shown inside the experimental setup in Fig. 5-7) having a 10 cm diameter and connected to a step motor that set the rotating speed. The disk was connected to a plastic shaft anchored to the step motor and set parallel to the ground. To avoid reflections from the wall of the water tank, a layer of US absorber was placed behind the disc. The tank was then filled with water to cover the probe and the disk providing a good acoustic coupling. The mixture forming the rotating phantom was made of agar (4%), silica (1%) and water.

The transmitted signals were 3, 5 and 7 cycles square waves at 3 MHz with a 2250 Hz PRF, focused at 40 mm depth inside the disc-shaped

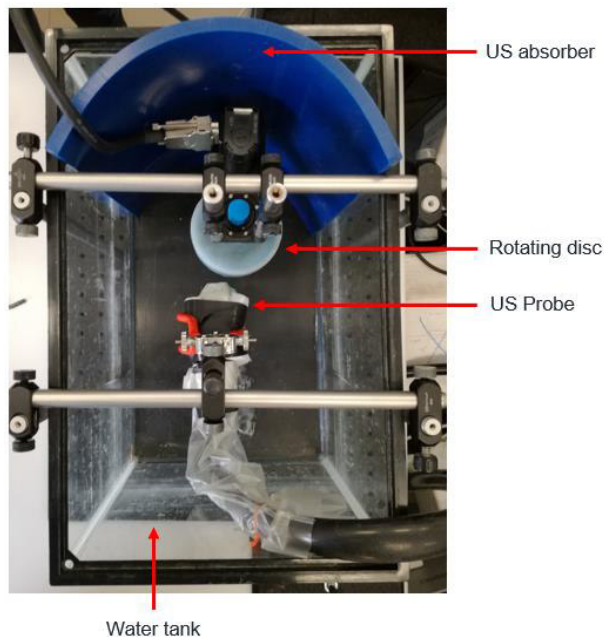


Fig. 5-7. Rotating disk measurements experimental setup (top view).

uniform agar phantom pushed to rotate at two different speeds ($\omega = 100$ or 200 °/s). The probe was regulated to let its axis intercept one disc chord. In each experimental test two different steering angles, $\theta=0^\circ$ and $\theta=12^\circ$, were used. A further test condition was used with the 1024-element arrangement: an excitation voltage equal to one-quarter of the one used on the 256-element configurations. This analysis was done to investigate the feasibility of ensuring the same transmitted signal power when using either the full or the sparse array configurations.

For every acquisition, the raw radiofrequency echo-data received from 640 transmission events (a tolerable number to avoid overloading the US scanner memory) was collected. These data were then beamformed off-line, quadrature demodulated to baseband and filtered using a low-pass filter to remove high frequency contributions. The I-Q slow-time samples received from each depth (from now on called Doppler signals) were weighted with a Blackman-Harris window prior to being converted to the frequency domain through a 128-point FFT [53], [69], [70]. After that the spectra at a chosen depth were averaged; the same operation was repeated for all depths within the disk. In particular, observing that all axial velocity components intercepted by the ultrasound beam are nearly the same, we averaged all spectra to finally produce one Doppler spectrum from each experiment.

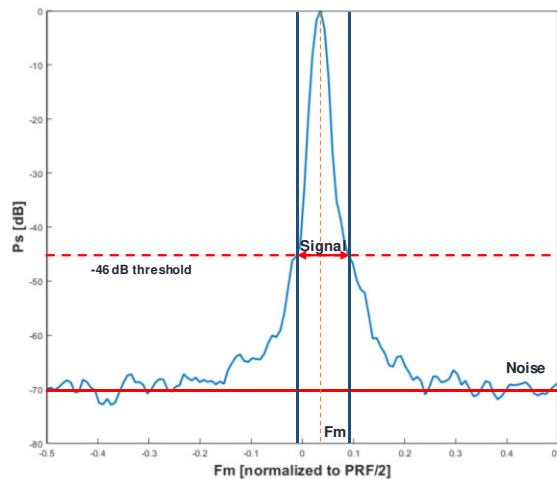


Fig. 5-8. Example of spectrum used to evaluate the Doppler spectra parameters.

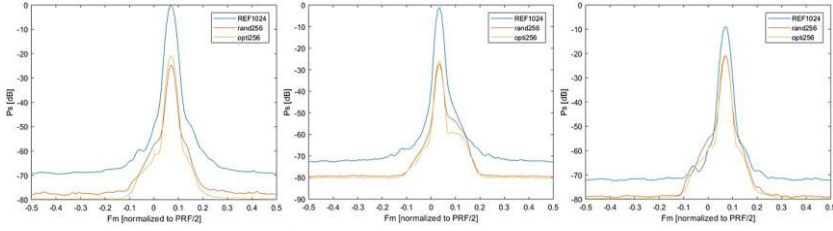


Fig. 5-9. Examples of Doppler spectra obtained with the three probe configurations by using the same TX signal amplitudes and 0° steering (left) or 12° steering (center) and when a higher voltage was applied to sparse configurations (right).

In the final Doppler spectrum, parameters (Fig. 5-8) like the mean Doppler frequency (Fm) were evaluated. Additionally, the signal power (Ps) and the signal-to-noise-ratio (SNR) were assessed. For Ps evaluation we considered the integral of the power densities on the main spectral lobe, described as the spectrum values above a heuristic threshold set at -46 -dB. The noise power was considered as the mean spectral power in the zone where it is almost flat, assuming that it keeps stable all over the bandwidth.

5.4.2. Results

Fig. 5-9 reports the Doppler spectra acquired in different experiments. All spectra were normalized respect to the maximum value related to ref1024 spectrum. A quantitative measure of the spectral parameters is reported in Table VI.

Fig. 5-9 shows that the peak intensity in ref1024 spectrum is much higher than the ones obtained with rand256 and opti26. Furthermore, it can be noted that the bandwidths and the peak positions are very close for all the three spectra. Additionally, the performances of the sparse arrays are almost the same referring the peak intensity and the noise level acquired.

The quantitative results are reported in Table VI. Here the same transmission voltage and disk rotating speed ($\omega = 100$ °/s - comparable results were obtained for $\omega = 200$ °/s) were used in all cases. Two steering angles were evaluated: 0° and 12° .

The Fm assessment for $\theta=0^\circ$ was not affected by probe elements sparsification as confirmed by the small differences observed on the acquired values, while it was slightly modified for $\theta=12^\circ$ (the mean

TABLE VI. PARAMETERS FOR 3 TX CYCLES, SPEED=100 °/s, SAME VOLTAGES APPLIED

	0° steering			12° steering		
	Fm^a	$SNR [dB]$	$Ps [dB]$	Fm^a	$SNR [dB]$	$Ps [dB]$
REF 1024	0.066	57.3	0.0	0.032	54.7	-2.5
Rand 256	0.065	38.6	-25.1	0.036	36.2	-28.3
Opti 256	0.066	43.6	-21.1	0.033	38.2	-27.1
Higher voltage for sparse probes						
REF 1024	0.066	48.4	-9.2	0.032	45.6	-11.5
Rand 256	0.065	42.6	-21.7	0.037	38.8	-25.6
Opti 256	0.065	43.6	-20.9	0.034	40.3	-24.8

a. Normalized to PRF/2

difference, among all the examined cases, resulted only in 1.3% of the Nyquist velocity).

The principal variations in the results obtained by using 256 or 1024 elements were associated with the SNR. Regarding the signal power, by applying the same TX voltages, we expect a difference of 24 dB passing from ref1024 to opti256 since we lose 12 dB in TX and 12 dB in RX. Nonetheless the channels contributing to the received noise are 4-times more numerous for ref1024. This leads to expect a quantity of noise, at the beamformer output, 6 dB higher compared to the 256-element solution. Overall when the probe elements used number pass from 1024 to 256, we await about $24-6 = 18$ SNR deterioration.

The results evaluation showed that the average SNR degradation was 17 dB for rand256 and 14.5 dB for opti256 configuration compared to ref1024; signal power outcomes highlighted 24 dB of difference among ref1024 and rand256 and 21.6 dB in comparison with opti256.

By applying an excitation voltage 4-times greater to the sparse arrays (40 V versus 10 V - results are shown in the bottom part of Table VI) we obtained an average SNR loss of 6 dB with rand256 and of 4.5 dB with opti256; the signal power lost 13 dB using rand256 and 11.5 dB using opti256 instead of ref1024. These results are close to the theoretical ones, but the SNR is also affected by the steering angle reducing it by roughly 3-4 dB in all tested configurations.

In conclusion, this preliminary study has experimentally appraised to what extent using a sparse array, rather than a full gridded one, affects spectral Doppler analysis. The results feature that spectrum shape along with its average Doppler frequency do not considerably vary. As awaited, the SNR suffers a forceful reduction, but it is possible to recover, up to 12 dB, by mean of exciting the sparse array elements using higher TX voltages, aiming to reach the same focal pressure generated by the complete 2-D array. This SNR recovery may be crucial for critical SNR conditions applications.

5.5. Spectral Doppler simulations and measurements with 2-D sparse arrays on a flow phantom

Based on the promising results of the preliminary work presented in Section 5.4, we decided to investigate the same topic in a more realistic scenario.

The outcomes of the former study, obtained with a rotating disk containing silicon particles mixed with agar gel, represented a nearly ideal situation: all scatterers intercepted by the scan line produce the alike Doppler spectrum, no clutter is involved, and attenuation is imperceptible. During the present activity, Field II simulations [71], [72] are introduced, where a parabolic fluid was investigated by a 1024 elements full gridded array and by the optimized sparse array (opti256) already used in the previous experiments. Moreover, extensive experimental tests are introduced, by using a more realistic phantom, in which a blood mimicking fluid flows in a tube drown in a tissue-mimicking material.

5.5.1. 2-D array probe, simulations, experiments setup and processing

Both simulations and acquisitions were based on the same 2-D array already used in the activities described in Section 4.4.1.

The two array layouts used in this activity are shown in Fig. 5-10: the whole 1024 elements of the reference array are reported and in blue the

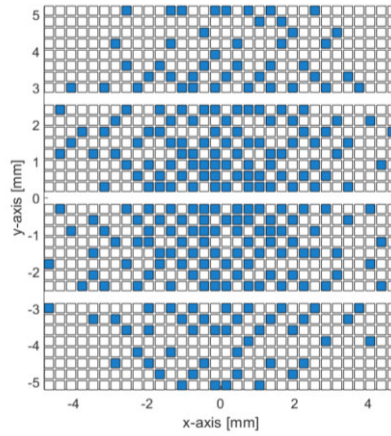


Fig. 5-10. Active elements distributions used in simulations and experiments. The elements of opti256 (blue) were selected from those available on the ref1024 array (both blue and white elements).

elements activated for opti256 are highlighted. Three empty lines along y-direction, due to manufacture constraints, can be observed.

The simulations structure was kept as similar as possible to the experiment structure detailed in the next paragraph.

A parabolic flow with steady velocity was simulated in a wall-less cylindrical vessel having a diameter (\emptyset) of 5 mm and a length of 24 mm. Adequately developed speckle was achieved by defining the density of the point scatterers to 8 scatterers/mm³, resulting in 12 scatterers per resolution cell, at least. In this work the minimal resolution cell was estimated to be 1.5 mm³ for ref1024. The scatterers were moved according to a parabolic profile in steady laminar flow, with peak

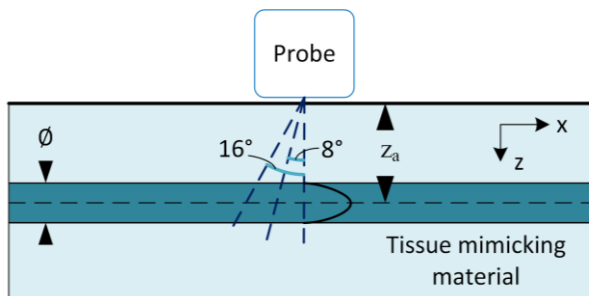


Fig. 5-11. Schematic of the experimental and simulations Spectral Doppler setup.

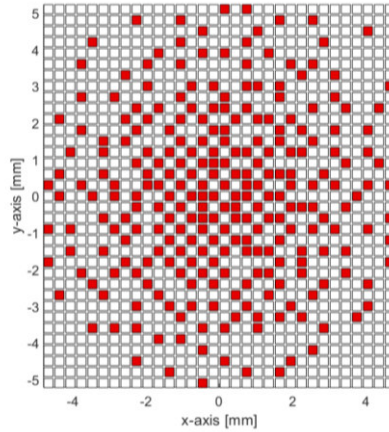


Fig. 5-12. Active elements distributions used in simulations only.
The elements of opti256 v2 (red) were selected from those available on the ref1120 array (both red and white elements).

velocity $V_p = 40$ cm/s. As reported in the scheme contained in Fig. 5-11, the vessel axis was imposed parallel to the probe x-axis, at a depth $z_a = 22.5$ mm. The flux was evaluated for a time interval $\Delta T = 1.82$ s with a pulse repetition frequency, PRF = 2250 Hz.

The ultrasound beams related to the 2-D probe used to realize the ref1024 and opti256 were simulated through Field II. The transmission beam was focused inside the vessel by using a 5-cycle sinusoidal burst at 3 MHz. In the reception phase, dynamic delay-and-sum beamforming algorithm was used without apodization. Three steering conditions were compared: 0° , 8° and 16° in each of the two orthogonal planes to the probe surface (XZ and YZ). When steering was performed on the YZ plane, the probe was rotated by 90° to set the vessel axis cohesive with the probe y axis.

Additionally, two further probe elements arrangements were simulated (ref1120 and opti256 v2, shown in Fig. 5-12) to assess the effects of the three missing lines in the Vermon probe, on the final Doppler spectra. This aspect will be considered in detail in Section 5.5.3.

For the experimental part, the ultrasound scanner was set in the same configuration described in Section 5.4.1).

The transmitted signals were 5-cycle square wave burst at 3 MHz frequency and 30 V of maximum amplitude, unless otherwise specified.

The ultrasound beam was focused on the center of the inspected vessel. In reception, dynamic focusing without dynamic apodization was executed. In every TX event, raw-echo data were acquired for a time interval $\Delta T = 0.89$ s with PRF = 2250 Hz, which corresponds to maximizing the occupation of the available memory onboard the ultrasound scanners.

The acquisitions were performed on the Doppler 403 Flow Phantom manufactured by Gammex (Middleton, WI, USA): it is a self-contained flow phantom comprising a 5-mm diameter (\emptyset) vessel, enclosed in a tissue mimicking material (attenuation: 0.5 dB/cm/MHz), where a blood mimicking liquid (Gammex patented Multi-Frequency HE [High Equivalency] GelTM) was pushed to flow at 4 ml/s constant rate or in pulsatile conditions. The probe was situated over the phantom surface, in parallel position respect to the vessel, whose axis sited at $z_a = 22.5$ mm, as in the simulation's activity. The tested steering angles were: $\theta = 0^\circ, 8^\circ, 16^\circ$ performed either in XZ and YZ plane (Fig. 5-11). To perform the same tests done in simulations, when the acoustic beam

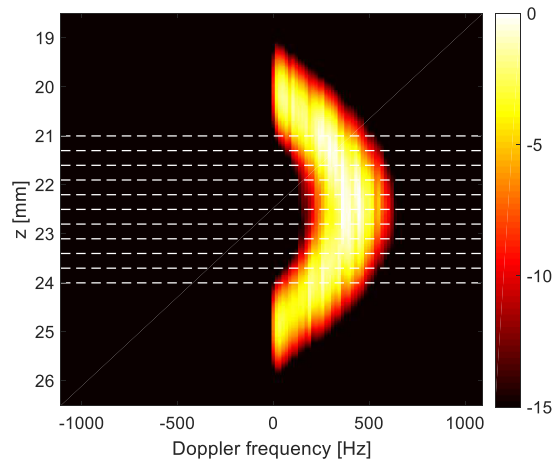


Fig. 5-13. Example of multi-gate spectral profile obtained in simulation with ref1024 producing a beam steered by 16° on the XZ plane. For each depth, the spectral amplitudes are coded according to the color bar on the right. Dotted lines indicate the depths considered in the estimate of spectral parameters.

was steered on the YZ plane, the probe was accordingly rotated by 90° to continue to intercept the vessel axis.

In every experimental acquisition, attentions were put to preserve the same setup conditions for successive measurements with ref1024 and opti256 arrangements. Considering that the aim of the experiments was comparing the spectra acquired with the two array layouts, potential minor misalignments among the probe symmetry axis and the vessel axis were neglected.

Simulated and experimental RF echo data collected from both the 2 D array configurations were off-line beamformed, demodulated and filtered low pass stage using MATLAB. The I-Q “slow-time” complex samples gathered from all the depths inspected (i.e., so-called Doppler signals), were gated with overlapping 128-point blocks, each one weighted using a Blackman-Harris window, and subsequently converted to the frequency domain with a 128-point FFT (as already done for the rotating disk experiments). Finally, all the spectra obtained from each depth were averaged in the “slow-time” direction, excepting the acquisitions in pulsatile flow conditions.

Fig. 5-13 reports an example of averaged multi-gate spectral Doppler profile [46], [73] obtained in simulations with a beam generated by ref1024 was steered of 16° on the XZ plane. In this profile, the power spectral Doppler densities detected at 19 to 26 mm depth were coded according to the color bar shown on the right [73]. The dotted lines specify the 11 particular depths (set apart by ≈ 0.3 mm) which were considered to evaluate the performance parameters of the related averaged spectra, as described in the next paragraph. These depths have been selected in the central region of the vessel where stream speeds are visibly different from zero.

In each Doppler spectrum coming from simulations and experiments the considered performance parameters have been:

- 1) the mean Doppler frequency (F_m),
- 2) the -6-dB bandwidth (BW),
- 3) the signal power (P_s),

as shown in Fig. 5-14. The signal-to-noise-ratio (SNR) was evaluated only for experimental data.

P_s was assessed as the integral of the power spectral densities above an empirical threshold (set here at -15 dB) higher than the detected

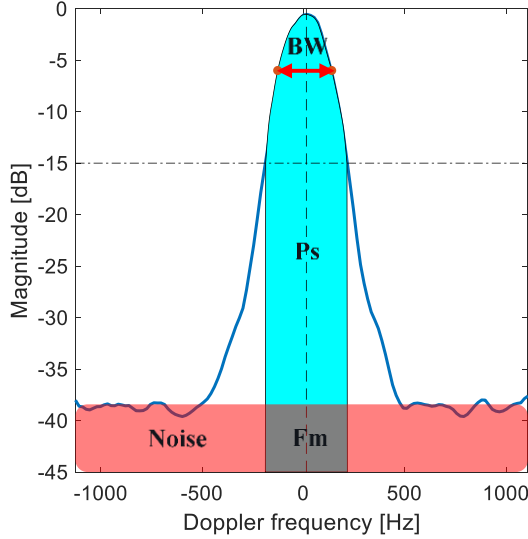


Fig. 5-14. Sample experimental Doppler spectrum obtained when all 1024 elements were used to transmit an unsteered beam. The figure shows how the spectral parameters (F_m , BW , P_s and noise) were evaluated.

system noise. Based on the experimental results we could assume the noise as white; then, its power spectral density could be approximated over the frequency range $[-PRF/2 - PRF/4]$ that, for all experiments, has not demonstrated to contain considerable signal contributions.

The relative differences between the parameters obtained with the two array configurations, have been evaluated for each steering angle, as follows:

$$\Delta F_m = \frac{F_{m_{opti256}} - F_{m_{ref1024}}}{F_{m_{ref1024}}} \quad (5.11)$$

$$\Delta BW = \frac{BW_{opti256} - BW_{ref1024}}{BW_{ref1024}} \quad (5.12)$$

$$\Delta P_s = \frac{P_{s_{opti256}}}{P_{s_{ref1024}}} \quad (5.13)$$

$$\Delta SNR = \frac{SNR_{opti256}}{SNR_{ref1024}} \quad (5.14)$$

For all the simulations/experiments performed, the above parameters were expressed by the average and the standard deviation (SD) of the

spectral values calculated at 11 distinct depths, as previously detailed (see Fig. 5-13).

5.5.2. Results

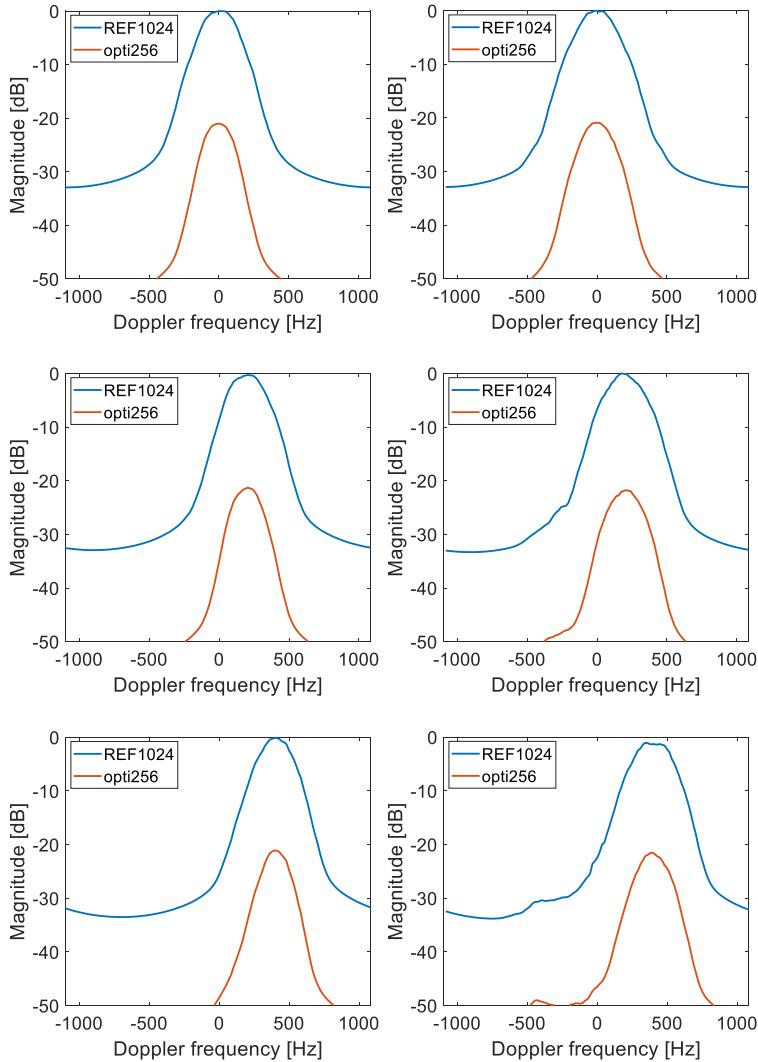


Fig. 5-15. Examples of simulated Doppler spectra obtained for the two probe configurations at 0° (top row), 8° (center row) and 16° (bottom row) steering in the XZ plane (left column) and in YZ plane (right column).

TABLE VII. SIMULATION PERFORMANCE METRICS

Steering [°]		opti256 vs ref1024		
XZ	YZ	$\Delta F_m \pm SD$ [%]	$\Delta BW \pm SD$ [%]	$\Delta P_s \pm SD$ [dB]
0	0	- ^a	-23.5±6.3	-22±0.08
8	0	-0.8±1.7	-19.5±5.4	-22±0.11
16	0	-0.7±1.2	-16±7.9	-21.9±0.04
0	0	- ^a	-15.2±6.5	-22.2±0.48
0	8	1.8±1.9	-15.2±3.1	-22±0.25
0	16	1.5±1.8	-13.5±5.2	-21.9±0.23
TOT:		0.5±1.6	-17.2±5.7	-22±0.20

a. F_m not evaluated because the nominal Doppler shift value is here zero

Fig. 5-15 reports six examples of spectra acquired in simulations while using different steering angles. All these spectra are associated to the sample volume placed into the vessel center. Especially, the two right bottom panels highlight that when the beam was steered on the YZ plane, sidelobes lower than 25 dB (not present with steering on the XZ plane) emerged for both array configurations.

The figure emphasize that the peak position is practically consistent with both layouts and that the spectra of ref1024 feature broader

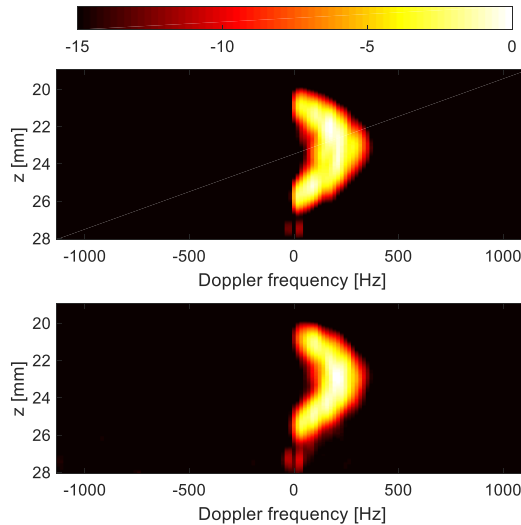


Fig. 5-16. Examples of multi-gate spectral Doppler obtained with ref1024 (top) and opti256 (bottom) with 16° of steering on XZ plane on the flow phantom. Each profile is normalized to the respective peak spectral density.

bandwidths. These assessments are consistent with the simulations results stated in Table VII. The average outcomes values highlight that:

- Fm difference between ref1024 and opti256 was 0.5%,
- BW was decreased by 17.2% and
- Ps was reduced by 22 dB using opti256 instead of ref1024.

Fig. 5-16 illustrates two examples of multi-gate spectral Doppler profiles got in the flow phantom experiments by using ref1024 and

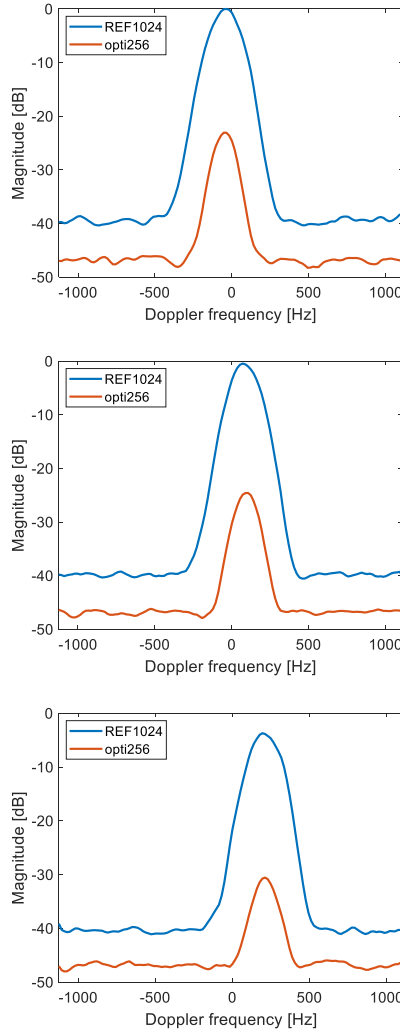


Fig. 5-17. Examples of experimental Doppler spectra obtained for the two probe configurations when the flow phantom was intercepted by US beams produced with 0° (top), 8° (center) and 16° (bottom) steering angles in the XZ plane.

TABLE VIII. EXPERIMENTS PERFORMANCE METRICS

Steering [°]		opti256 vs ref1024			
XZ	YZ	$\Delta F_m \pm SD$ [%]	$\Delta BW \pm SD$ [%]	$\Delta P_s \pm SD$ [dB]	$\Delta SNR \pm SD$ [dB]
0	0	- ^b	-30.9±6.1	-24.8±0.5	-17.6±0.6
8	0	5.5±7.2	-20.6±5.8	-24.9±0.2	-17.8±0.3
16	0	-1.4±6.2	-8.2±12.5	-27.6±0.6	-20.9±0.6
0	0	- ^b	-20.7±4.8	-25.3±0.2	-17.8±0.4
0	8	2.4±7.1	-19.3±9.8	-21.3±0.5	-14.3±0.5
0	16	2.1±11.5	-9.9±8.6	-19.8±0.2	-12.5±0.4
TOT:		2.2±8	-18.3±7.9	-24±0.4	-16.8±0.5

b. F_m not evaluated because the nominal Doppler shift value is here zero

opti256 probe configurations, respectively. For both profiles, parabolic flow is clearly observable over nearly the same ranges of Doppler shift.

In Fig. 5-17 shows three experimental spectra corresponding to the sample volume that intercepts the highest flow velocity, when the stream was investigated by the ultrasound beam at 3 different angles (0° , 8° , 16°). It can be observed that the spectral shape and the frequency of

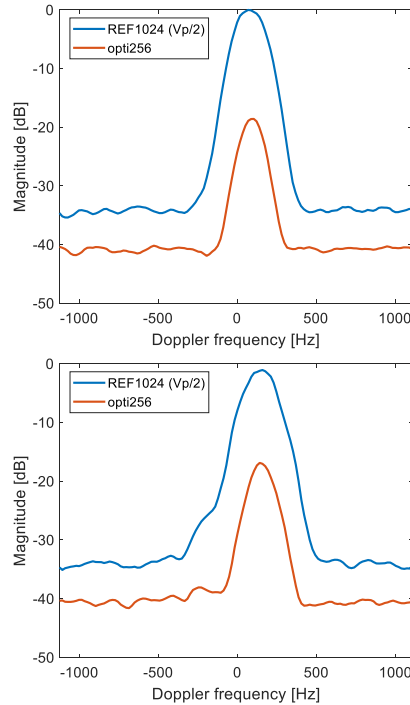


Fig. 5-18. Examples of Doppler spectra obtained on the horizontal vessel with 8° steering on XZ plane (top) and on YZ plane (bottom). The spectra of ref1024 are acquired using a -6 dB lower excitation voltage.

maximum amplitude (roughly equivalent to the mean frequency) remain similar for both probe patterns, while the signal and noise levels are significantly different. The noise spectral density resulted about 6 dB higher for ref1024, consistent with the 4-fold larger elements/channels number that contribute to increase the receiver noise. Conversely, the signal power is significantly lower for opti256 (between -20 to -28 dB), because of the 4-fold reduced transmitted pressure and number of receiving channels.

This behaviour is corroborated by the experimental measurements summarized in Table VIII: an average difference of 24 dB between ref1024 and opti256 signal powers recorded across the different steering conditions, with a notable deterioration at the highest steering angles. The associate SNR discrepancy between ref1024 and opti256 resulted 16.8 dB, on average.

The Fig. 5-18 shows the spectra obtained when the TX beam was steered by 8° on XZ (top panel) and by 8° on YZ planes (bottom panel). In these cases, opti256 was excited with a double TX amplitude (30V) compared to the one used for ref1024 (15V). The spectral noise densities difference is the same as in Fig. 5-17 (roughly 6 dB), since that does not depend on the TX amplitude. On the other hand, the signal power difference is reduced (18 dB) leading to a SNR discrepancy of only 11.8 dB when opti256 is used in place of ref1024.

5.5.3. Discussion

The principal aim of this work was defining to what extent sparse arrays, optimized to transmit ultrasound focused beams, may impact on the results of spectral Doppler investigations.

In both simulations and acquisitions, we decided to use opti256 arrangement as descriptive example of a sparse array. This configuration has demonstrated to be able to offer images of good quality [44], also in comparison with the images produced by a “completely random” sparse array probe, rand256 (i.e., a distribution reached by using the same iterations number employed to obtain opti256 and selecting the best random elements arrangements).

The rand256 has been excluded from this study because the preliminary experiments performed on a rotating disk [74], have shown

that its spectral Doppler outcomes are comparable to the opti256 ones, even though slightly worse.

It is clearly highlighted, from the simulations results, that for all the examined steering conditions, the Doppler spectrum shape and their relative mean frequency, F_m , are basically unchanged by using a sparse, rather than a fully populated, array is utilized. In terms of F_m , the mean difference was only 0.5%.

On the other hand, observing Fig. 5-15 and Table VII, the Doppler bandwidths observed on the sparse arrays are considerably narrower. This result appears consistent with the different equivalent apertures of the two considered arrays. Actually, as reported in literature [53], [49], [70], [50], [75], due to the transit-time broadening, the resulting BW depends on the equivalent aperture, A , of the array. Approximating A as two times the average distance between the element positions from the center of the probe, A resulted 6 mm for opti256 and 7.8 mm for ref1024. The proportion of the two apertures is then 77%. Considering, in particular, the measurements made at 0° beam-to-flow-angle, where the bandwidth is proportional to the aperture and to the largest intercepted velocity (but is not influenced by the potential presence of lower velocities inside the considered sample volume) the average bandwidth reduction for opti256 is 17.2%, in reasonable agreement with 77% ratio between the two equivalent array apertures. Nonetheless, given the velocity estimation from the spectral mean frequency, this reduction in the bandwidth does not interfere with the velocity estimation, but should be taken under consideration in velocity assessments based on spectral peak frequency [76].

Given the asymmetrical layout of the used probe (three lines of elements are missing on the y-direction) the ultrasound beams resulted not symmetrical respect the probe axis: simulations highlighted that for opti256, the -6dB beamwidths lengthways the x- and y-axis were 1.75 mm and 1.47 mm; instead in ref1024 case they resulted in 1.31 mm and 1.20 mm. For instance, these different beamwidths led to the different ΔBW s in the two 0° - 0° cases stated in Table VII and in Table VIII.

Simulations also evidenced the appearance of low-level spectral sidelobes when the US beam was tilted within the YZ plane (Fig. 5-15). Also, in Fig. 5-18, a small sidelobe (<-20 dB) is visible for ref1024 but not in opti256 spectrum, possibly because it is covered by noise. A

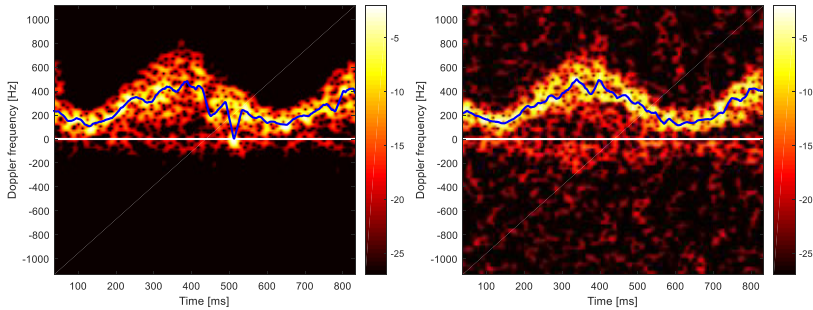


Fig. 5-19. Examples of spectrograms obtained with *ref1024* (left) and *opti256* (right) with 16° of steering on YZ plane on the flow phantom (the dynamic range was 25dB in both panels while the gain was adjusted to highlight the different SNRs).

possible explanation of this behavior will be given in the end of this Section.

Experimental outcomes have validated the invariance of spectrum shape and mean frequency by using the two different probe element arrangements (Table VIII and Fig. 5-16, 5-17, 5-18). Furthermore, spectrograms like those shown in Fig. 5-19 display that the Doppler spectra continue to be qualitatively comparable also in pulsatile flow conditions. The time behavior of the average Doppler frequency (the blue solid lines) were assessed for both array designs and compared by performing the Pearson product-moment correlation coefficient. This resulted $r = 0.856$, that represents a good statistical correlation, in particular if we consider the noise level on the spectrograms and the reduced signal power reached with *opti256*.

Unfortunately, the experimental setup was not always able to ensure an accurate positioning of the probe axis respect to the vessel. For example, the small negative Doppler shift in the first panel of Fig. 5-17 (in the case without steering) was due to a Doppler angle not exactly at 90° as required. Anyhow, the main goal was to compare the spectra obtained using either *ref1024* or *opti256*, so we paid particularly attention to maintain the setup conditions stable for consecutive measurements based on the two array patterns.

The flexibility limitations of the experimental setup have not permitted to accurately testing situations where the vessel axis was at

different depths or intercepted by beams steered on directions not coincident with XZ and YZ planes. However, the multi-gate spectral Doppler method permits to have Doppler spectra at several depths. Even though these spectra are not reported here, the outcomes in Table VII and Table VIII, showing the average and the standard deviation of the values obtained at various depth, confirm the principal conclusions of this work. Additionally, other steering conditions have been simulated, and the associated Doppler spectra resulted very similar to the ones shown in Fig. 5-15. Moreover, further simulations were done with another sparse array made by 128 elements (opti128: refer to [40]) and they confirmed the invariance of Fm and the BW reduction due to a smaller equivalent aperture of array. Clearly, also the Ps was decreased given the halved of the elements number.

The most important differences among the experimental results gathered using 256 or 1024 elements are associated to the signal and the noise power. For what concern the signal power, transmitting the same excitation amplitudes, 24 dB of difference between ref1024 and opti256 are estimated. Actually, the 4-fold smaller number of TX-RX elements involves an average acoustic pressure loss of 12 dB and, taking into account full coherence among all RX channel signals, an additional reduction of 12 dB in the receiver. On the other hand, the channels that participate to the received noise is 4-times larger for ref1024. This leads the total noise at the beamformer output to be 6 dB higher than in the 256-element situation. In aggregate, using 256 elements instead of the 1024 available in the full array, we assume to have, on average, about $24-6=18$ dB of SNR loss. The experiments results are coherent with this forecast, having obtained an average SNR improvement of 16.8 dB (standard deviation = 0.5) by means of using ref1024.

The SNR degradation may impact negatively in vivo acquisitions by limiting the maximum penetration depth, preventing, for instance, the Doppler investigation of deep vessels. This drawback could be partly surmounted by using higher TX voltages for sparse arrays, to try to achieve the same focal pressure (i.e., same Mechanical Index) of the full-gridded array, on the face of an accurate valuation of the possible consequences on the Thermal Index.

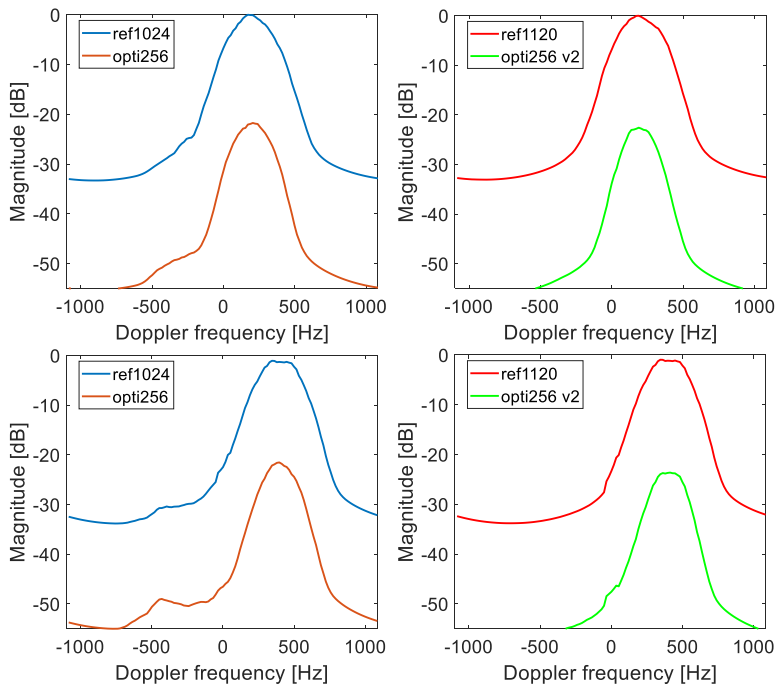


Fig. 5-20. Doppler spectra comparison between probe configurations with (Fig. 5-10) and without (Fig. 5-12) empty lines: obtained at 8° (the two at the top) and 16° (the two at the bottom) steering angles in YZ plane.

Another possible solution is to try to exploit coded imaging techniques, that have already shown their capability of increasing the SNR in Doppler analysis [77] by up to 12 dB.

Lastly, when the beam was tilted within the YZ plane, low sidelobes (< -25 dB) appeared for ref1024 and opti256 (Fig. 5-20, left column). The simulations performed with ref1120 and opti256 v2 (Fig. 5-12) proved that these sidelobes are caused by the three missing elements lines on y-direction (Fig. 5-20, right column).

It is important to mention that the comparison between different arrays was performed without employing any apodization neither in transmission and neither in reception to maximize the sensitivity and the SNR. In a real situation, apodization would have been applied to ref1024 to decrease the sidelobes, hence restricting the actual aperture and also reducing the Doppler bandwidth. On the other side, the active elements density on opti256 increases towards the center, i.e. a kind of density tapering came from the optimization constraints imposed on the

5 **Spectral Doppler with 2-D sparse arrays**

acoustic beam pattern. Consequently, the beam shape was already optimized and any additional apodization would have only further limit its sensitivity and deteriorate its performance.

Chapter 6. Conclusions

This chapter summarizes the contribution of the thesis and discusses possible directions for future research.

6.1. Summary of Contributions

This PhD project has provided contributions in terms of hardware (i.e. circuit developments) as well as in terms of methods (i.e. new methods development) concerning the use of innovative ultrasound probes.

Electronic boards were developed to make the open US scanner ULA-OP 256 compatible with new linear (1-D) and matrix (2-D) CMUT probes so as to expand the system potentiality toward new research activities that may take benefit of the use of such probes.

Novel 2-D probe element configurations (sparse arrays) for high-frame rate and Doppler applications have been investigated.

The imaging performance of sparse arrays when transmitting Diverging Waves was experimentally tested and the influence of different virtual sources distributions was evaluated. The results of this preliminary work confirm that virtual source distribution plays a primary role, and it will be important to determine the optimal distribution for each application.

First in vitro (flow phantom) results of spectral Doppler analysis obtained with a 256-element sparse array were compared with the results produced by a full-gridded 1024-element array. This work has determined the performance of sparse arrays in spectral Doppler acquisitions. In general, the characteristics of obtained Doppler spectra resulted consistent with the predictions of theory. However, the reduced number of used elements must be compensated with appropriate TX/RX techniques to recover the signal power loss.

6.2. Direction of Future Works

This thesis work has fostered different research activities. The possibility of using 1-D and 2-D CMUT arrays with the ULA-OP 256 system, has favored the collaboration of the University of Florence with the University of Roma Tre and the University of Waterloo (Canada) on the development of novel approaches for 3D imaging (with the former one for the realization of new CMUT transducers and testing of 2D sparse array probes with the latter). The problem of optimizing the virtual sources position when Diverging Waves are transmitted from 2-D probes is currently investigated at the University of Lyon. Finally, the positive results of spectral Doppler analysis based on sparse array

probes have encouraged the start of the development of a novel real-time 3D spectral Doppler system by the University of Florence.

Future work will be focused along three main directions:

- Regarding the Spectral Doppler with sparse arrays activity some aspects remain to be addressed. Techniques to recover the SNR loss due to the element number reduction in sparse arrays needs to be investigated (increasing the transmitting Voltage and/or using coded imaging techniques);
- The current limitations of the experimental setup may be addressed to permit the investigation of additional steering angles and focal depths and, especially, a necessary real-time visualization, which will be essential for preliminary in-vivo tests.
- Exploring new possible sparse arrays configurations to define layout and material characteristics optimized to adapt such arrays to different applications.

Bibliography

- [1] E. Boni *et al.*, “ULA-OP 256: A 256-Channel Open Scanner for Development and Real-Time Implementation of New Ultrasound Methods,” *IEEE Trans. Ultrason. Ferroelectr. Freq. Control*, vol. 63, no. 10, pp. 1488–1495, Oct. 2016.
- [2] P. Tortoli, L. Bassi, E. Boni, A. Dallai, F. Guidi, and S. Ricci, “ULA-OP: an advanced open platform for ultrasound research,” *IEEE Trans. Ultrason. Ferroelectr. Freq. Control*, vol. 56, no. 10, pp. 2207–2216, Oct. 2009.
- [3] M. I. Haller and B. T. Khuri-Yakub, “A surface micromachined electrostatic ultrasonic air transducer,” *IEEE Trans. Ultrason. Ferroelectr. Freq. Control*, vol. 43, no. 1, pp. 1–6, Jan. 1996.
- [4] I. Ladabaum, Xuecheng Jin, H. T. Soh, A. Atalar, and B. t. Khuri-Yakub, “Surface micromachined capacitive ultrasonic transducers,” *IEEE Trans. Ultrason. Ferroelectr. Freq. Control*, vol. 45, no. 3, pp. 678–690, May 1998.
- [5] M. Tanter and M. Fink, “Ultrafast imaging in biomedical ultrasound,” *IEEE Trans. Ultrason. Ferroelectr. Freq. Control*, vol. 61, no. 1, pp. 102–119, Jan. 2014.
- [6] L. Demi, “Practical Guide to Ultrasound Beam Forming: Beam Pattern and Image Reconstruction Analysis,” *Appl. Sci.*, vol. 8, no. 9, p. 1544, Sep. 2018.
- [7] R. W. Prager, U. Z. Ijaz, A. H. Gee, and G. M. Treece, “Three-dimensional ultrasound imaging,” *Proc. Inst. Mech. Eng. [H]*, vol. 224, no. 2, pp. 193–223, 2010.

Bibliography

- [8] A. Fenster, D. B. Downey, and H. N. Cardinal, “Three-dimensional ultrasound imaging,” *Phys. Med. Biol.*, vol. 46, no. 5, pp. R67–R99, Apr. 2001.
- [9] T. R. Nelson and D. H. Pretorius, “Three-dimensional ultrasound imaging,” *Ultrasound Med. Biol.*, vol. 24, no. 9, pp. 1243–1270, Nov. 1998.
- [10] J. Provost *et al.*, “3D ultrafast ultrasound imaging in vivo,” *Phys. Med. Biol.*, vol. 59, no. 19, pp. L1–L13, Oct. 2014.
- [11] L. Sugeng *et al.*, “Quantitative assessment of left ventricular size and function: side-by-side comparison of real-time three-dimensional echocardiography and computed tomography with magnetic resonance reference,” *Circulation*, vol. 114, no. 7, pp. 654–661, Aug. 2006.
- [12] E. D. Light, S. F. Idriss, P. D. Wolf, and S. W. Smith, “Real-time three-dimensional intracardiac echocardiography,” *Ultrasound Med. Biol.*, vol. 27, no. 9, pp. 1177–1183, Sep. 2001.
- [13] G. Stetten *et al.*, “Real-time 3D ultrasound: A new look at the heart,” vol. 15, Jan. 1998.
- [14] D. Garcia, P. Lantelme, and E. Saloux, “Introduction to speckle tracking in cardiac ultrasound imaging,” 2018.
- [15] D. Wildes *et al.*, “4-D ICE: A 2-D Array Transducer With Integrated ASIC in a 10-Fr Catheter for Real-Time 3-D Intracardiac Echocardiography,” *IEEE Trans. Ultrason. Ferroelectr. Freq. Control*, vol. 63, no. 12, pp. 2159–2173, 2016.
- [16] P. Santos, G. U. Haugen, L. Lovstakken, E. Samset, and J. D’hooge, “Diverging Wave Volumetric Imaging Using Subaperture Beamforming,” *IEEE Trans. Ultrason. Ferroelectr. Freq. Control*, vol. 63, no. 12, pp. 2114–2124, 2016.
- [17] G. Matrone, A. S. Savoia, M. Terenzi, G. Caliano, F. Quaglia, and G. Magenes, “A volumetric CMUT-based ultrasound imaging system simulator with integrated reception and μ -beamforming electronics models,” *IEEE Trans. Ultrason. Ferroelectr. Freq. Control*, vol. 61, no. 5, pp. 792–804, May 2014.
- [18] A. Bhuyan *et al.*, “Integrated Circuits for Volumetric Ultrasound Imaging With 2-D CMUT Arrays,” *IEEE Trans. Biomed. Circuits Syst.*, vol. 7, no. 6, pp. 796–804, Dec. 2013.
- [19] J. Kortbek, J. A. Jensen, and K. L. Gammelmark, “Sequential beamforming for synthetic aperture imaging,” *Ultrasonics*, vol. 53, no. 1, pp. 1–16, Jan. 2013.

- [20] R. Fisher *et al.*, “Reconfigurable arrays for portable ultrasound,” in *IEEE Ultrasonics Symposium, 2005.*, 2005, vol. 1, pp. 495–499.
- [21] I. O. Wygant *et al.*, “An integrated circuit with transmit beamforming flip-chip bonded to a 2-D CMUT array for 3-D ultrasound imaging,” *IEEE Trans. Ultrason. Ferroelectr. Freq. Control*, vol. 56, no. 10, pp. 2145–2156, Oct. 2009.
- [22] S. W. Smith, H. G. Pavy, and O. T. von Ramm, “High-speed ultrasound volumetric imaging system. I. Transducer design and beam steering,” *IEEE Trans. Ultrason. Ferroelectr. Freq. Control*, vol. 38, no. 2, pp. 100–108, Mar. 1991.
- [23] O. T. von Ramm, S. W. Smith, and H. G. Pavy, “High-speed ultrasound volumetric imaging system. II. Parallel processing and image display,” *IEEE Trans. Ultrason. Ferroelectr. Freq. Control*, vol. 38, no. 2, pp. 109–115, Mar. 1991.
- [24] M. Flesch *et al.*, “4D in vivo ultrafast ultrasound imaging using a row-column addressed matrix and coherently-compounded orthogonal plane waves,” *Phys. Med. Biol.*, vol. 62, no. 11, pp. 4571–4588, 07 2017.
- [25] I. B. Daya, A. I. H. Chen, M. J. Shafiee, A. Wong, and J. T. W. Yeow, “Compensated Row-Column Ultrasound Imaging System Using Multilayered Edge Guided Stochastically Fully Connected Random Fields,” *Sci. Rep.*, vol. 7, no. 1, pp. 1–18, Sep. 2017.
- [26] H. Bouzari *et al.*, “Curvilinear 3-D Imaging Using Row-Column-Addressed 2-D Arrays With a Diverging Lens: Feasibility Study,” *IEEE Trans. Ultrason. Ferroelectr. Freq. Control*, vol. 64, no. 6, pp. 978–988, Jun. 2017.
- [27] T. L. Christiansen, M. F. Rasmussen, J. P. Bagge, L. N. Moesner, J. A. Jensen, and E. V. Thomsen, “3-D imaging using row-column-addressed arrays with integrated apodization— part ii: transducer fabrication and experimental results,” *IEEE Trans. Ultrason. Ferroelectr. Freq. Control*, vol. 62, no. 5, pp. 959–971, May 2015.
- [28] A. S. Logan, L. L. P. Wong, A. I. H. Chen, and J. T. W. Yeow, “A 32 x 32 element row-column addressed capacitive micromachined ultrasonic transducer,” *IEEE Trans. Ultrason. Ferroelectr. Freq. Control*, vol. 58, no. 6, pp. 1266–1271, Jun. 2011.
- [29] A. Savoia *et al.*, “P2B-4 Crisscross 2D cMUT Array: Beamforming Strategy and Synthetic 3D Imaging Results,” in *2007 IEEE Ultrasonics Symposium Proceedings, 2007*, pp. 1514–1517.

Bibliography

- [30] B. Savord and R. Solomon, "Fully sampled matrix transducer for real time 3D ultrasonic imaging," in *IEEE Symposium on Ultrasonics*, 2003, 2003, vol. 1, pp. 945-953 Vol.1.
- [31] E. Roux, A. Ramalli, P. Tortoli, C. Cachard, M. Robini, and H. Liebgott, "2-D Ultrasound Sparse Arrays Multidepth Radiation Optimization Using Simulated Annealing and Spiral-Array Inspired Energy Functions," *IEEE Trans. Ultrason. Ferroelectr. Freq. Control*, vol. 63, no. 12, pp. 2138–2149, Dec. 2016.
- [32] B. Diarra, M. Robini, P. Tortoli, C. Cachard, and H. Liebgott, "Design of Optimal 2-D Nongrid Sparse Arrays for Medical Ultrasound," *IEEE Trans. Biomed. Eng.*, vol. 60, no. 11, pp. 3093–3102, Nov. 2013.
- [33] C. Tekes, M. Karaman, and F. L. Degertekin, "Optimizing circular ring arrays for forward- looking IVUS imaging," *IEEE Trans. Ultrason. Ferroelectr. Freq. Control*, vol. 58, no. 12, pp. 2596–2607, Dec. 2011.
- [34] M. Karaman, I. O. Wygant, Ö. Oralkan, and B. T. Khuri-Yakub, "Minimally Redundant 2-D Array Designs for 3-D Medical Ultrasound Imaging," *IEEE Trans. Med. Imaging*, vol. 28, no. 7, pp. 1051–1061, Jul. 2009.
- [35] A. Austeng and S. Holm, "Sparse 2-D arrays for 3-D phased array imaging - design methods," *IEEE Trans. Ultrason. Ferroelectr. Freq. Control*, vol. 49, no. 8, pp. 1073–1086, Aug. 2002.
- [36] A. Trucco, "Thinning and weighting of large planar arrays by simulated annealing," *IEEE Trans. Ultrason. Ferroelectr. Freq. Control*, vol. 46, no. 2, pp. 347–355, Mar. 1999.
- [37] J. Provost, C. Papadacci, C. Demene, J. Gennisson, M. Tanter, and M. Pernot, "3-D ultrafast doppler imaging applied to the noninvasive mapping of blood vessels in Vivo," *IEEE Trans. Ultrason. Ferroelectr. Freq. Control*, vol. 62, no. 8, pp. 1467–1472, Aug. 2015.
- [38] J. A. Jensen *et al.*, "SARUS: A synthetic aperture real-time ultrasound system," *IEEE Trans. Ultrason. Ferroelectr. Freq. Control*, vol. 60, no. 9, pp. 1838–1852, Sep. 2013.
- [39] L. Petrusca *et al.*, "Fast Volumetric Ultrasound B-Mode and Doppler Imaging with a New High-Channels Density Platform for Advanced 4D Cardiac Imaging/Therapy," *Appl. Sci.*, vol. 8, no. 2, Feb. 2018.
- [40] E. Roux, A. Ramalli, H. Liebgott, C. Cachard, M. C. Robini, and P. Tortoli, "Wideband 2-D Array Design Optimization With Fabrication Constraints for 3-D US Imaging," *IEEE Trans. Ultrason. Ferroelectr. Freq. Control*, vol. 64, no. 1, pp. 108–125, Jan. 2017.

Bibliography

- [41] E. Roux *et al.*, “Validation of optimal 2D sparse arrays in focused mode: Phantom experiments,” in *2017 IEEE International Ultrasonics Symposium (IUS)*, 2017, pp. 1–4.
- [42] M. Fink, “Time reversal of ultrasonic fields. I. Basic principles,” *IEEE Trans. Ultrason. Ferroelectr. Freq. Control*, vol. 39, no. 5, pp. 555–566, Sep. 1992.
- [43] G. Montaldo, M. Tanter, J. Bercoff, N. Benech, and M. Fink, “Coherent plane-wave compounding for very high frame rate ultrasonography and transient elastography,” *IEEE Trans. Ultrason. Ferroelectr. Freq. Control*, vol. 56, no. 3, pp. 489–506, Mar. 2009.
- [44] E. Roux, F. Varray, L. Petrusca, C. Cachard, P. Tortoli, and H. Liebgott, “Experimental 3-D Ultrasound Imaging with 2-D Sparse Arrays using Focused and Diverging Waves,” *Sci. Rep.*, vol. 8, no. 1, pp. 1–12, Jun. 2018.
- [45] N. Thomas and S. Leeman, “The double Doppler effect,” in *International Conference on Acoustic Sensing and Imaging, 1993.*, 1993, pp. 164–168.
- [46] P. Tortoli, F. Guidi, G. Guidi, and C. Atzeni, “Spectral velocity profiles for detailed ultrasound flow analysis,” *IEEE Trans. Ultrason. Ferroelectr. Freq. Control*, vol. 43, no. 4, pp. 654–659, Jul. 1996.
- [47] V. L. Newhouse, P. J. Bendick, and W. Varner, “Analysis of Transit Time Effects on Doppler Flow Measurement,” *IEEE Trans. Biomed. Eng.*, vol. BME-23, no. 5, pp. 381–387, Sep. 1976.
- [48] R. V. Edwards, J. C. Angus, M. J. French, and J. W. Dunning, “Spectral Analysis of the Signal from the Laser Doppler Flowmeter: Time-Independent Systems,” *J. Appl. Phys.*, vol. 42, no. 2, pp. 837–850, Feb. 1971.
- [49] V. L. Newhouse, E. S. Furgason, G. F. Johnson, and D. A. Wolf, “The Dependence of Ultrasound Doppler Bandwidth on Beam Geometry,” *IEEE Trans. Sonics Ultrason.*, vol. 27, no. 2, pp. 50–59, Mar. 1980.
- [50] G. Guidi, C. Licciardello, and S. Falteri, “Intrinsic spectral broadening (ISB) in ultrasound Doppler as a combination of transit time and local geometrical broadening,” *Ultrasound Med. Biol.*, vol. 26, no. 5, pp. 853–862, Jun. 2000.
- [51] D. Censor, V. L. Newhouse, T. Vontz, and H. V. Ortega, “Theory of ultrasound Doppler-spectra velocimetry for arbitrary beam and flow configurations,” *IEEE Trans. Biomed. Eng.*, vol. 35, no. 9, pp. 740–751, Sep. 1988.

Bibliography

- [52] P. Tortoli, G. Guidi, and V. L. Newhouse, “Improved blood velocity estimation using the maximum Doppler frequency,” *Ultrasound Med. Biol.*, vol. 21, no. 4, pp. 527–532, 1995.
- [53] Ph. D. Evans D. H. and W. N. McDicken, *Doppler ultrasound: physics, instrumentation, and signal processing*, 2nd ed. Chichester ; New York : J. Wiley, 2000.
- [54] Y. Karabiyik, I. K. Ekroll, S. H. Eik-Nes, and L. Lovstakken, “Quantitative Doppler Analysis Using Conventional Color Flow Imaging Acquisitions,” *IEEE Trans. Ultrason. Ferroelectr. Freq. Control*, vol. 65, no. 5, pp. 697–708, May 2018.
- [55] I. K. Ekroll, T. Dahl, H. Torp, and L. Løvstakken, “Combined vector velocity and spectral Doppler imaging for improved imaging of complex blood flow in the carotid arteries,” *Ultrasound Med. Biol.*, vol. 40, no. 7, pp. 1629–1640, Jul. 2014.
- [56] G. Urban *et al.*, “State of the Art: Non-Invasive Ultrasound Assessment of the Uteroplacental Circulation,” *Semin. Perinatol.*, vol. 31, no. 4, pp. 232–239, Aug. 2007.
- [57] G. A. Roth *et al.*, “Global, Regional, and National Burden of Cardiovascular Diseases for 10 Causes, 1990 to 2015,” *J. Am. Coll. Cardiol.*, vol. 70, no. 1, pp. 1–25, Jul. 2017.
- [58] M. Kozàková, C. Morizzo, F. Andreucetti, P. Palchetti, G. Parenti, and C. Palombo, “Quantification of extracranial carotid artery stenosis by ultrafast three-dimensional ultrasound,” *J. Am. Soc. Echocardiogr.*, vol. 14, no. 12, pp. 1203–1211, Dec. 2001.
- [59] B. López-Melgar *et al.*, “Accurate quantification of atherosclerotic plaque volume by 3D vascular ultrasound using the volumetric linear array method,” *Atherosclerosis*, vol. 248, pp. 230–237, May 2016.
- [60] J. Avdal, L. Løvstakken, H. Torp, and I. K. Ekroll, “Combined 2-D Vector Velocity Imaging and Tracking Doppler for Improved Vascular Blood Velocity Quantification,” *IEEE Trans. Ultrason. Ferroelectr. Freq. Control*, vol. 64, no. 12, pp. 1795–1804, Dec. 2017.
- [61] S. Holbek *et al.*, “Ultrasonic 3-D Vector Flow Method for Quantitative In Vivo Peak Velocity and Flow Rate Estimation,” *IEEE Trans. Ultrason. Ferroelectr. Freq. Control*, vol. 64, no. 3, pp. 544–554, Mar. 2017.
- [62] M. S. Wigen *et al.*, “4-D Intracardiac Ultrasound Vector Flow Imaging—Feasibility and Comparison to Phase-Contrast MRI,” *IEEE Trans. Med. Imaging*, vol. 37, no. 12, pp. 2619–2629, Dec. 2018.

Bibliography

- [63] S. Fiorentini, L. M. Saxhaug, T. G. Bjåstad, E. Holte, H. Torp, and J. Avdal, "Maximum Velocity Estimation in Coronary Arteries Using 3-D Tracking Doppler," *IEEE Trans. Ultrason. Ferroelectr. Freq. Control*, vol. 65, no. 7, pp. 1102–1110, Jul. 2018.
- [64] E. Kang *et al.*, "A Reconfigurable Ultrasound Transceiver ASIC with 24x40 Elements for 3-D Carotid Artery Imaging," *IEEE J. Solid-State Circuits*, vol. 53, no. 7, pp. 2065–2075, Jul. 2018.
- [65] S. Holbek, T. L. Christiansen, M. B. Stuart, C. Beers, E. V. Thomsen, and J. A. Jensen, "3-D Vector Flow Estimation With Row–Column-Addressed Arrays," *IEEE Trans. Ultrason. Ferroelectr. Freq. Control*, vol. 63, no. 11, pp. 1799–1814, Nov. 2016.
- [66] O. Martínez-Graullera, C. J. Martín, G. Godoy, and L. G. Ullate, "2D array design based on Fermat spiral for ultrasound imaging," *Ultrasonics*, vol. 50, no. 2, pp. 280–289, Feb. 2010.
- [67] A. Ramalli, E. Boni, A. S. Savoia, and P. Tortoli, "Density-tapered spiral arrays for ultrasound 3-D imaging," *IEEE Trans. Ultrason. Ferroelectr. Freq. Control*, vol. 62, no. 8, pp. 1580–1588, Aug. 2015.
- [68] A. Austeng and S. Holm, "Sparse 2-D arrays for 3-D phased array imaging - experimental validation," *IEEE Trans. Ultrason. Ferroelectr. Freq. Control*, vol. 49, no. 8, pp. 1087–1093, Aug. 2002.
- [69] P. Tortoli, G. Guidi, P. Berti, F. Guidi, and D. Righi, "An FFT-based flow profiler for high-resolution in vivo investigations," *Ultrasound Med. Biol.*, vol. 23, no. 6, pp. 899–910, Jan. 1997.
- [70] P. Tortoli, G. Guidi, and P. Pignoli, "Transverse Doppler spectral analysis for a correct interpretation of flow sonograms," *Ultrasound Med. Biol.*, vol. 19, no. 2, pp. 115–121, Jan. 1993.
- [71] J. A. Jensen, "FIELD: A Program for Simulating Ultrasound Systems," in *10th Nordicbaltic Conference on Biomedical Imaging, Vol. 4, Supplement 1, Part 1:351–353*, 1996, pp. 351–353.
- [72] J. A. Jensen and N. B. Svendsen, "Calculation of pressure fields from arbitrarily shaped, apodized, and excited ultrasound transducers," *IEEE Trans. Ultrason. Ferroelectr. Freq. Control*, vol. 39, no. 2, pp. 262–267, Mar. 1992.
- [73] P. Tortoli, G. Bambi, F. Guidi, and R. Muchada, "Toward a better quantitative measurement of aortic flow," *Ultrasound Med. Biol.*, vol. 28, no. 2, pp. 249–257, Feb. 2002.
- [74] P. Mattesini *et al.*, "Spectral Doppler Measurements with 2-D Sparse Arrays," in *2018 IEEE International Ultrasonics Symposium (IUS)*, 2018, pp. 1–4.

Bibliography

- [75] A. C. H. Yu, A. H. Steinman, and R. S. C. Cobbold, "Transit-time broadening in pulsed Doppler ultrasound: a generalized amplitude modulation model," *IEEE Trans. Ultrason. Ferroelectr. Freq. Control*, vol. 53, no. 3, pp. 530–541, Mar. 2006.
- [76] P. Tortoli, G. Guidi, and V. L. Newhouse, "Improved blood velocity estimation using the maximum Doppler frequency," *Ultrasound Med. Biol.*, vol. 21, no. 4, pp. 527–532, 1995.
- [77] A. Ramalli, E. Boni, A. Dallai, F. Guidi, S. Ricci, and P. Tortoli, "Coded Spectral Doppler Imaging: From Simulation to Real-Time Processing," *IEEE Trans. Ultrason. Ferroelectr. Freq. Control*, vol. 63, no. 11, pp. 1815–1824, Nov. 2016.